University of Sussex

Very Strong and Supercool Electroweak Phase Transitions

Christopher Peter Dereck Harman

Submitted for the degree of Doctor of Philosophy

University of Sussex

December 2016

Declaration

The content of Chapter 2 is based on work that resulted in the publication of ref. [1]. The content of Chapter 4 is based on work that is in preparation for publication.

I hereby declare that this thesis has not been and will not be submitted in whole or in part to another University for the award of any other degree.

Signature:

Christopher Peter Dereck Harman

UNIVERSITY OF SUSSEX

Christopher P. D. Harman, Doctor of Philosophy

Very Strong and Supercool Electroweak Phase Transitions

Summary

The aim of this work is to determine whether any zero temperature features of the scalar potential strongly influence the finite temperature properties of the electroweak phase transition. In particular, we address whether one can get an arbitrarily strong phase transition from zero temperature effects.

We investigate a variety of models of varying complexity. For the models we look into, we successfully determine that the vacuum energy difference at zero temperature has a direct influence on the critical temperature. This leads to arbitrarily strong phase transitions, subject to the caveat that sliding behaviour does not occur. What we call sliding behaviour is the scenario in which the broken vacuum destabilises under thermal corrections before reaching the critical temperature. The parameter subspace in which sliding behaviour *does* occur often leads to significantly weakened phase transitions.

For a more detailed investigation of the phase transition one must look at the thermal decay of the false vacuum. Choosing a non-supersymmetric real singlet extension to the Standard Model, called the xSM, we detail by example how one can systematically investigate some non-trivial phase transition properties. The specific model we adopt is the $\mathbb{Z}_2$xSM which has a $\mathbb{Z}_2$ discrete symmetry imposed on the singlet as well as the Higgs field. We focus on the non-sliding parameter subspace, which has a minimal zero temperature parameter space of only three free parameters. For this setup, the depth of the potential at zero temperature has a one-to-one mapping with the strength of the phase transition at critical temperature so we can trivially choose the strength. This allows for a systematic approach to investigating very strong phase transitions and their connection to the amount of supercooling, latent heat, bubble nucleation rate, and a hydrodynamical friction parameter. We also trace out the parameter region in which runaway bubbles are expected and discuss the implications for gravitational wave production.

Acknowledgements

I would like to thank all past, present, and future members of the Theoretical Particle Physics group at the University of Sussex for their support throughout my doctoral journey. I have thoroughly enjoyed every stimulating conversation and warm ale, as well as every stimulating ale and warm conversation, with Luke Arpino, Andrew Bond, Djuna Croon, Raul Cuesta, Daniel Cutting, Barry Dillon, Glauber Dorsch, Basem El-Menoufi, Filipe Ferriera de Freitas, Andy Granger, Nicola Hopkins, Ibere Kuntz, Sandra Kvedaraitė, Kirsty Leslie, Alba Leticia Carrillo, Jonathan Manuel, Edouard Marchais, Heather McAslan, Gustavo Medina, Ken Mimasu, Sonali Mohapatra, Jose Miguel No, Jan Schroeder, Jack Setford, Agamemnon Sfondilis, and Tom Steudtner.

Further, I would also like to thank all of the faculty and guests for sharing their knowledge and enthusiasm: Mudhahir Al Ajmi, David Bailin, Andrea Banfi, Xavier Calmet, Sebastian Jaeger, Daniel Litim, and Veronica Sanz. A special thank you to my internal and external examiners, Mark Hindmarsh and Thomas Konstandin. Finally, a very special thank you (with a cherry on top) to my PhD supervisor, Stephan Huber, whom supported me through and endured my many tantrums with Wolfram Mathematica.

Thank you to Melissa Baker, Engy Ghozlan, and Mohammad Sholkalmy for the emotional support and great first year as I attempted to understand supersymmetry. Christopher Fritz who has been a great friend and like a brother throughout my studies.

To my immediate family: dad, mum, brother, and sister. Thank you for the lifetime of, and continuing, support. I will try my best to translate this thesis to each of you someday; best set aside a few days.

And finally to Tugba Buyukbese whom our relationship strongly transitioned throughout my PhD. From a great friend and office mate to my now lifelong partner.

Contents

List of Tables

List of Figures

Chapter 1

Introduction

1.1 What's hot and what's not?

The fundamental physics community is in the midst of an exciting and distressing time. Throughout my last few years as an active researcher within a crossover region between particle theory and cosmology, there have been two landmark discoveries and a few disappointing results. Both landmark discoveries confirm theoretical predictions in the modern picture of both particle physics and cosmology.

The first landmark discovery was, of course, the detection of a CP-even Higgs boson at the Large Hadron Collider (LHC) in CERN [3, 4]. The Higgs is the final SM particle to be discovered and the first observed fundamental scalar in the history of science. The second landmark discovery was the observation of gravitational waves at LIGO [5]. What makes the discovery more exciting is that, from our current understanding, the observed signal can only be sourced by a binary black hole merger. Both discoveries almost complete the most popular theories in modern theoretical physics: the Standard Model of particle physics (SM) and the general theory of relativity. It is also fascinating that these ingredients were hypothesised in works conducted over 50 years [6–8] and 100 years ago [9, 10], respectively.

On the more disappointing side lies the realm of Beyond the Standard Model (BSM) physics. The end of Run 2 of the LHC has been disappointing for searches for supersymmetric extensions of the SM, raising the difficulty in finding an answer to the hierarchy problem. With nothing but the SM the theory/phenomenology community was rather deprived of direction, until December 2015. Suddenly, there was a shimmer of light for the particle physics community. A diphoton excess signal was reported by the ATLAS and CMS collaborations at the LHC with a greater than 3σ global significance (5σ local

significance) [11, 12]. A smoking gun was fired, but not with a recognisable signature. Nonetheless, a cascade of theorists and phenomenologists jumped on the opportunity - against the advice of experimental particle physicists - swamping the publishing world with the words *750 GeV diphoton excess*. Unfortunately, the signal disappeared as quickly as it came [13, 14], consistent with the cautionary tales of experimental particle physicists. The small flash of light was a glitch in the matrix. Without the diphoton signal, the theory community's direction was pulled back into the dark.

As far as matters in the dark go, even the world of dark matter is in an uncomfortable corner. Searches for particle candidates of dark matter are not optimistic. Nought but null results are reported and soon the parameter space for WIMP dark matter by direct detection will be exhausted [15]. This is a result of the neutrino background dominating in the lower cross sections of parameter space [16].

So has the fundamental physics community squandered its fortunes? Could there be no other physics beyond the SM? The first question may be answered by the predictions of astrology - in which I am void of expertise - so I can not comment. However, the answer to the second question - in which I do have expertise - is no.

Although the Higgs boson has been discovered, the SM is far from complete. A desirable "theory of everything" should not only be confined to microscopic (quantum) or macroscopic (classical) physics, but should also transcend scales. For example, in field theory language, the scalar potential describes the scalar particle content and interactions in the universe. An approach to transcend between the quantum and classical scales in field theory is called thermal field theory. This approach cranks up the heat in quantum field theory, equipping each coupling in the scalar potential with a temperature-dependence. It is (literally) the hot topic in particle physics.

Since the discovery of gravitational waves, an important question has been raised. Namely, what implications does the scalar potential have on the production of gravitational waves produced during cosmological phase transitions? This question can be broken down via an intermediate step. Existing literature has reviewed in great detail the connection between gravitational waves and the properties of a first order phase transition [17–19]. The other question is: what implications does the scalar potential have on the phase transition properties? Such a question is the subject area of this thesis and acts as a guiding light for the scientific community where purely microscopic/macroscopic questions have failed.

1.2 Thesis goal(s)

This thesis relates the subject of BSM theories to an important era in our cosmological history called the Electroweak Phase Transition (EWPT). The discovery of the Higgs boson is essential to the EWPT properties. In this regard, I consider myself incredibly lucky to have studied in the post-Higgs discovery era. This discovery set me up as a researcher with fresh eyes and one less phenomenological parameter to worry about: the Higgs mass. In fixing the Higgs mass, implications of BSM physics on the EWPT can be investigated with all SM content inherently included, i.e. anything new must be sourced from the BSM sector or is a remnant of the theoretical framework.

The aim of the following work is to determine a one-size-fits-all criteria as to how to obtain a strong electroweak phase transition from zero temperature effects. We attempt to establish a connection between the properties of the electroweak phase transition (thermal field theory quantities) and collider phenomenology (zero temperature, quantum field theory quantities). But why should we care about the strength of the phase transition? In the mechanism of electroweak baryogenesis, there is a need for what is called a strong electroweak phase transition [20, 21]. The "strength of the phase transition" may be naively measured through the value of $\xi_c \equiv \sqrt{2}\, v_c/T_c$, where v_c is the Higgs vacuum expectation value at critical temperature T_c. A strong first order phase transition is necessary to suppress the sphaleron transition rate from the broken vacuum to symmetric vacuum during the EWPT [21, 22]. Without a sufficient suppression rate any generated net baryon number may be washed out, inconsistent with our observed universe. Furthermore, very strong phase transitions may produce gravitational waves during the phase transition whose signals may be observed by future gravitational wave detectors [23–29].

We find such a connection between the critical temperature T_c and a zero temperature quantity called the vacuum energy difference $\Delta V(0)$. This quantity is defined as the difference in potential energy between the broken vacuum and symmetric extremum of the zero temperature effective scalar potential. A reader familiar with the literature will recognise this quantity as the free energy density difference evaluated at zero temperature. This work provides a clear insight of the underlying mechanism that provides arbitrarily strong phase transitions from zero temperature effects, e.g. tree level barriers, cubic terms, high number of singlet degrees of freedom.

1.3 Layout of the thesis

In Chapter 2 we investigate six BSM extensions, one of which is a supersymmetric extension. All non-supersymmetric scalar effective potentials are renormalised up to one loop, including the top quark and electroweak gauge bosons only. The supersymmetric extension we consider, called the Generalised Next-to-Minimal Supersymmetric extension of the Standard Model (GNMSSM), additionally includes one loop contributions for the stops (supersymmetric partners of the top quark). For all but the GNMSSM, we derive analytic expressions for the one loop vacuum energy difference at zero temperature in Section 2.2. For each model we consider a subspace of our free parameters that is assumed to capture all physics below the TeV scale. By means of a numerical scan, in Section 2.3 we draw correlations between $\Delta V(0)$, the critical temperature T_c, and the strength of the phase transition, ξ_c. Throughout this chapter we drop the subscript notation, referring to the strength as simply ξ.

Parameter points that exhibit sliding behaviour have a reduced strength. There does, however, exist a well-defined lower branch to the strength of the phase transition. This encourages an investigation into aspects of the Minimal SM with the Higgs mass as a free parameter, see Section 2.4. For this simple model, we briefly consider the impact of the treatment of the effective potential on our numerical results, e.g. zero temperature radiative effects, inclusion of Higgs into the loop, resummation effects.

As an intermediary, in Chapter 3, we briefly review the formalism behind calculating less trivial properties of the EWPT. This involves reviewing Coleman's paper on the decay of the false vacuum [30]. We discuss the concept of the bounce solution, surface tension, critical energy of the bubble, and false vacuum decay rate. The following chapter relies on numerical computation of thermal phase transition quantities discussed in this section.

Our intention in Chapter 4 is to investigate more technical EWPT properties, and determine whether the hypothesis in Chapter 2 holds for *alternative definitions* of the strength of the phase transition used in modern literature. We focus on the non-sliding parameter region of the $\mathbb{Z}_2$xSM model. This region is the parameter subspace discovered in Chapter 2 that has a one-to-one mapping between the strength of the phase transition measured at critical temperature $\xi_c = \sqrt{2}\, v_c/T_c$, now denoted with an index for clarity, and the vacuum energy difference $\Delta V(0)$. The bounce solution, as approximated by the minimised path, is described in Section 4.3.1. Though we realise that this may not be the trajectory in field space taken by the true bounce, it allows us to apply the undershooting/overshooting procedure to approximate the phase transition properties.

For non-sliding parameter regions, we describe the vacuum structure of potential at tree level and at one loop level in Section 4.1. We then analytically derive some desirable phase transition properties in the high and low temperature expansion. The expressions found match well with the numerically determined parameter points, where the validity of the low/high temperature expansion holds. We determine a method to scan over the parameter space of the two field potential for fixed strength ξ_c.

We further constrain our parameter space to only include phase transitions that are expected to have runaway bubble walls during the phase transition, according to the Bödeker-Moore criterion [31]. This is a choice; the non-runaway region of the non-sliding parameter space is left for future investigations. We chose this region because it is the region of maximal supercooling for the non-sliding parameter space, see Section 4.4. This region is of particular interest in two field models [31, 32]. We draw out the perimeter of this *runaway region* for various phase transition properties against the strength ξ_c. We finally calculate various measures of the strength of the phase transition and other phase transition properties for the perimeter of the runaway region. Some of the more advanced properties calculated are those of an effective friction parameter, with and without hydrodynamics considered into the calculation. We also look at the acoustically-generated gravitational wave relic density produced from the electroweak phase transition [33].

Finally, we summarise our findings and discuss future directions in Chapter 5.

Chapter 2

A recipe for arbitrarily strong phase transitions

"N-now th-that that don't ~~kill~~ slide me
Can only make me stronger"

A variation of Stronger by Kayne West, Graduation album

Since the discovery of a scalar particle of mass 125 GeV at the Large Hadron Collider [3, 4], the question of how electroweak symmetry breaking happened in the early universe has gained even more urgency. Also the problem of how to embed the Higgs into a 'natural' framework remains.

Supersymmetric extensions to the Standard Model (SM) are strong candidates for a fundamental theory that describe observations in particle physics and cosmology [34]. These include (a) elegantly unifying all forces at a grand unification scale, (b) providing a dynamical mechanism for electroweak symmetry breaking, and (c) containing a rich dark matter particle sector. Other popular areas of research using supersymmetric models are the theoretical developments [35–43] into obtaining a strong first order electroweak phase transition. Such phase transitions are necessary for electroweak baryogenesis (for a recent review see e.g. [44, 45]), i.e. an explanation for the observed matter-antimatter asymmetry of the universe through a mechanism present during the electroweak phase transition.

There is a similar demand for an understanding of how to obtain a strong phase transition in non-supersymmetric models [24, 46–55]. However, there does not currently exist a universal link between a strong phase transition and the zero temperature phenomenology of any given model. One notable work categorises multiple models into three classes, distinguished by whether a strong phase transition is driven by tree level, loop level, or

thermal physics [56]. A strong phase transition in [56] carries the notion of having a large barrier separating the broken and symmetric vacua. They also remark on the zero temperature phenomenology of parameter regions that exhibit a strong phase transition. Our paper adopts a similar approach to studying the electroweak phase transition.

We investigate a new perspective on how to understand the phase transition using a quantity defined at one loop zero temperature: the vacuum energy difference. This very quantity was already mentioned in [42]. We investigate in detail the role that this quantity plays for some basic properties of the phase transition for six models. These models are described in Section 2.1 alongside a review of the one loop effective potential at zero temperature and with thermal corrections included.

Generally, we find a strong correlation between the vacuum energy difference and the strength of the phase transition. This correlation only breaks down if, before the critical temperature, the broken minimum turns into a saddle point upon thermal corrections. This special case can only occur in multi-field models, where it fortunately is further disfavoured once experimental constraints have been applied. So typically a strong first order phase transition is dependent on a mild tuning of the vacuum energy. A tuning at the level of about 30% is mostly sufficient. This allows one to zoom into the regime of strong first order phase transitions in a simple and efficient way, including complicated models such as the Generalised Next-to-Minimal Supersymmetric extension to the Standard Model (GNMSSM).

In Section 2.2 we define the vacuum energy difference. We then derive analytic expressions of this quantity for all but the supersymmetric model. We discuss the scanning procedure and present the numerical results in Section 2.3. The results with and without phenomenological constraints applied are contrasted against each other. Numerical bounds that guarantee a strong phase transition are suggested for phenomenologically viable parameter regions for each model. Three interesting benchmarks scenarios for the GNMSSM data are provided and compared. Finally, we draw up conclusions in Section 2.5.

2.1 The scalar potentials

2.1.1 The models

Throughout this work we will be making reference to the SM, three single field modifications to the SM, and two general singlet extensions of the SM (one of which is supersymmetric). In counting the number of free parameters in each model, we do not include

those appearing through one loop corrections from the top quark and electroweak (EW) gauge bosons[1], each of whose couplings are well determined. We will proceed by briefly describing the models that we use.

SM

For the SM Higgs potential, we use the notation

$$V_{\text{tree}}^{[\text{SM}]}(H) = -\mu_0^2|H|^2 + \lambda_0|H|^4, \tag{2.1}$$

where $H = (H^+, H^0)$ is the complex SM Higgs doublet and the SM Higgs boson arises from $\phi = \text{Re}(\text{H}^0)$. In setting the Higgs mass to be $m_h = 125$ GeV and choosing the Vacuum Expectation Value (VEV) of ϕ, we have no free parameters in this model.

SM with a dimension-six operator

We use the potential [57]

$$V_{\text{tree}}^{[\text{SM}+\phi^6]}(H) = -\mu_0^2|H|^2 + \lambda_0|H|^4 + \frac{1}{M^2}|H|^6. \tag{2.2}$$

We identify the free parameter of this model as the mass scale, M, that appears in the suppression factor of the dimension-six term. The form of this potential can be realised as the low energy description of some strongly coupled models or from integrating out a scalar with a high characteristic mass scale.

SM from Gauge Mediation of Exact Scale Breaking (GMESB)

This model is introduced in ref. [58] as

$$V_{\text{1 loop (0T)}}^{[\text{SM}+\text{log}]}(H) = -\frac{1}{2}m_h^2|H|^2\left(1 + \left(\frac{4\lambda_0 v^2}{m_h^2} - 1\right)\log\left[\frac{|H|^2}{v^2}\right]\right) + \lambda_0|H|^4. \tag{2.3}$$

This potential is the quantum effective potential at zero temperature. It arises when the scale symmetry is broken in a hidden sector through quantum corrections and mediated to the observable sector via gauge interactions only. We identify the free parameter of this theory to be the quartic self-coupling of the Higgs, λ_0. The phase transition of this model has previously been studied in [59].

[1] These SM quantum corrections are governed by the top Yukawa coupling, y_t, and EW gauge couplings, g_2 and g_1.

SM with an additional Coleman-Weinberg scalar

We use the same potential as that of the SM but include a new real scalar X that contributes a Coleman-Weinberg term at zero temperature

$$V^{[\text{SM+scalar}]}_{\text{1 loop (0T)}}(H) = V^{[\text{SM}]}_{\text{1 loop (0T)}}(H) + y^2|H|^2X^2 + \frac{1}{(8\pi)^2}m_X^4(H)\left(\log\left[\frac{m_X^2(H)}{Q^2}\right] - \frac{3}{2}\right), \quad (2.4)$$

where $m_X^2(H) = y^2|H|^2$. The $V^{[\text{SM}]}_{\text{1 loop (0T)}}(H)$ term is the SM one loop Higgs potential. The free parameter of this theory is the coupling, y, of the new scalar to the Higgs. We make the additional assumption that the new scalar does not produce thermal corrections to the potential. We use this model as a probe to distinguish between the impact of zero and finite temperature corrections to the effective potential. This should be kept in mind throughout our discussion in Section 2.4.

SM plus a real singlet (xSM)

We write the potential with a similar notation to refs. [48]

$$V^{[\text{xSM}]}_{\text{tree}}(H,S) = -\mu_0^2|H|^2 + \lambda_0|H|^4 + \frac{a_1}{2}|H|^2S + \frac{a_2}{2}|H|^2S^2 + \frac{b_2}{2}S^2 + \frac{b_3}{3}S^3 + \frac{b_4}{4}S^4. \quad (2.5)$$

Here S is a real singlet scalar field. This potential contains three types of terms: purely H, purely S, and mixed terms. Note that we have cubic terms entering as both an S^3 and $S|H|^2$ term. Essential to phenomenological constraints is the Higgs-singlet mixing angle, α, defined via

$$\begin{pmatrix} h \\ s \end{pmatrix} = \begin{pmatrix} \cos\alpha & \sin\alpha \\ -\sin\alpha & \cos\alpha \end{pmatrix} \begin{pmatrix} \phi \\ S \end{pmatrix}. \quad (2.6)$$

We can recognise $\sin\alpha$ as the singlet component of the SM Higgs, h. In rewriting the parameters μ_0, a_2, b_2, and b_4 in terms of v, v_S, m_h, and m_s (of which v and m_h are fixed) we are left with a total of five free parameters (two of them being tree level cubic terms). We will define the new parameter choice more precisely in Section 2.2.2.

GNMSSM

Supersymmetric extensions of the SM are promising settings to realise a strong phase transition. However, in the Minimal Supersymmetric extension to the Standard Model (MSSM) with superpotential [34]

$$\mathcal{W}_{\text{MSSM}} = \bar{u}\mathbf{y_u}QH_u - \bar{d}\mathbf{y_d}QH_d - \bar{e}\mathbf{y_e}LH_d + \mu H_u \cdot H_d, \quad (2.7)$$

LHC constraints on Higgs properties make a strong phase transition driven by light stops very unlikely [60]. Here $\bar{u}$, $\bar{d}$, $\bar{e}$, Q and L are the usual lepton and quark supermultiplets, $\mathbf{y_u}$, $\mathbf{y_d}$, and $\mathbf{y_e}$ are 3×3 Yukawa matrices, $H_u = (H_u^+, H_u^0)$ and $H_d = (H_d^0, H_d^-)$ are the "up-type" and "down-type" complex Higgs doublets, and μ is the supersymmetric analogue of the Higgs mass, commonly referred to as the "μ-parameter".

Singlet extensions of the MSSM have attractive features for Higgs phenomenology. For instance, there are mechanisms to increase the natural upper bound of the lightest CP-even Higgs bosons mass (see e.g. [61, 62]). Also these models often generate a strong phase transition [35–38, 42, 43, 63]. Singlet extensions of the MSSM are often distinguished by discrete symmetries. Here we study the most general singlet extension, the Generalised Next-to-Minimal Supersymmetric extension to the Standard Model (GNMSSM) with the superpotential

$$\mathcal{W} = \mathcal{W}_{\text{MSSM}} + \lambda S H_u \cdot H_d + k_1 S + \frac{1}{2} k_2 S^2 + \frac{1}{3} k_3 S^3, \tag{2.8}$$

where S is a chiral singlet superfield and λ, k_1, k_2, and k_3 encode couplings and masses. This model can be derived in a top-down approach based on a discrete R symmetry as shown in [64]. Not having a discrete symmetry automatically evades a possible domain wall problem that plagues more constrained setups [65]. Adding the usual soft supersymmetry breaking terms, the tree level scalar potential is given by

$$\begin{aligned} V_{\text{tree}}^{[\text{GNMSSM}]} = \; & \left(|\mu + \lambda S|^2 + m_{H_u}^2\right) |H_u|^2 + \left(|\mu + \lambda S|^2 + m_{H_d}^2\right) |H_d|^2 + m_S^2 |S|^2 \\ & + |\lambda H_u \cdot H_d + k_1 + k_2 S + k_3 S^2|^2 + \frac{1}{8}(g_2^2 + g_1^2)\left(|H_u|^2 - |H_d|^2\right)^2 + \frac{1}{2} g_2^2 |H_d^\dagger H_u|^2 \\ & + \left[\left((b\mu + A_\lambda \lambda S) H_u \cdot H_d + A_{k_1} k_1 S + \frac{1}{2} A_{k_2} k_2 S^2 + \frac{1}{3} A_{k_3} k_3 S^3\right) + h.c\right]. \end{aligned} \tag{2.9}$$

The soft supersymmetry breaking parameters are m_{H_u}, m_{H_d}, m_S, b, A_λ, A_{k_1}, A_{k_2}, and A_{k_3}. These are all mass dimension one and take on values of the order of the supersymmetry breaking scale, $m_{\text{SUSY}} \sim \mathcal{O}(1\text{ TeV})$. We decompose the Higgs gauge-eigenstates into the mass-eigenstates via

$$\begin{pmatrix} H_u^0 \\ H_d^0 \\ S \end{pmatrix} = \begin{pmatrix} v \sin\beta \\ v \cos\beta \\ v_S \end{pmatrix} + \frac{1}{\sqrt{2}} \mathbf{R}_{0^+} \begin{pmatrix} h^0 \\ H^0 \\ s^0 \end{pmatrix} + \frac{i}{\sqrt{2}} \mathbf{R}_{0^-} \begin{pmatrix} G^0 \\ A^0 \\ \eta^0 \end{pmatrix}, \tag{2.10}$$

$$\begin{pmatrix} H_u^+ \\ H_d^{-*} \end{pmatrix} = \mathbf{R}_{\pm} \begin{pmatrix} G^+ \\ H^+ \end{pmatrix}, \tag{2.11}$$

where the $\mathbf{R}$'s are the relevant rotation matrices. We only need to understand the contents of $\mathbf{R}_{0^+}$ (the CP-even mass mixing matrix) for this study. In order to more easily compare the phenomenology of the GNMSSM to that of the xSM, we decouple the heavy CP-even Higgs boson, H^0. In practice this means that we reduce the three-dimensional field space of eq. (2.10) into a two-dimensional field space by looking in the $\tan\beta$ direction

$$\begin{pmatrix} H_u^0 \\ H_d^0 \\ S \end{pmatrix} = \begin{pmatrix} \phi \sin\beta \\ \phi \cos\beta \\ S \end{pmatrix} = \begin{pmatrix} \sin\beta & 0 \\ \cos\beta & 0 \\ 0 & 1 \end{pmatrix} \begin{pmatrix} \phi \\ S \end{pmatrix}. \tag{2.12}$$

We will be scanning for parameter points where $\tan\beta$ varies from low to medium values so we will keep the β-dependence explicit throughout this work. Just as in the xSM, we recognise $\sin\alpha$ as the singlet component of the CP-even Higgs state, h^0. We allow for either the lightest or next-to-lightest state [61] to be h^0, recognised as the 125 GeV Higgs boson.

It is well known that Higgs sectors of supersymmetric extensions to the SM suffer from a tree level bound on the lightest CP-even state (see ref. [34] for a review). Radiative corrections from the stop sector are crucial. The stop squared-masses are given by

$$\begin{aligned} m_{\tilde{t}_1}^2 &= \frac{1}{2}\left(m_{\tilde{t}_L}^2 + m_{\tilde{t}_R}^2 + \sqrt{(m_{\tilde{t}_L}^2 - m_{\tilde{t}_R}^2)^2 + 4m_{X_t}^4}\right) \\ m_{\tilde{t}_2}^2 &= \frac{1}{2}\left(m_{\tilde{t}_L}^2 + m_{\tilde{t}_R}^2 - \sqrt{(m_{\tilde{t}_L}^2 - m_{\tilde{t}_R}^2)^2 + 4m_{X_t}^4}\right), \end{aligned} \tag{2.13}$$

where the squared-mass matrix in the gauge-eigenstate basis $(\tilde{t}_L, \tilde{t}_R)$ is given by

$$\mathbf{m}_{\tilde{\mathbf{t}}}^{\mathbf{2}} = \begin{pmatrix} m_{\tilde{t}_L}^2 = m_{Q_3}^2 + y_t^2|H_u^0|^2 + \Delta_{\tilde{u}_L} & m_{X_t}^2 = A_t^* y_t (H_u^0)^* - (\mu + \lambda S) y_t H_d^0 \\ (m_{X_t}^2)^* = A_t y_t H_u^0 - (\mu + \lambda S)^* y_t (H_d^0)^* & m_{\tilde{t}_R}^2 = m_{\tilde{u}_3}^2 + y_t^2|H_u^0|^2 + \Delta_{\tilde{u}_R} \end{pmatrix}, \tag{2.14}$$

$$\text{and } \Delta_{\tilde{u}_L} = \frac{1}{4}\left(g_2^2 - \frac{1}{3}g_1^2\right)\left(|H_u^0|^2 - |H_d^0|^2\right), \; \Delta_{\tilde{u}_R} = \frac{1}{3}g_1^2\left(|H_u^0|^2 - |H_d^0|^2\right), \tag{2.15}$$

and m_{Q_3} and $m_{\tilde{u}_3}$ are the stop soft masses, A_t is a third generation soft parameter, and y_t is the top Yukawa coupling.

Assuming there are no CP violating phases and all terms in the potential are real, we have a total of 16 parameters in this theory. However, not all of these are free parameters.

Applying the minimum conditions and assuming that only the real parts of the fields are non-zero in the minimum, we reparameterise the Higgs mass-squared soft parameters ($m^2_{H_u}$, $m^2_{H_d}$, and m^2_S) by the VEVs in the broken phase (v, $\tan\beta$, and v_S). We also choose to remove the singlet linear term in the potential by taking $A_{k_1} = -k_2$, meaning that a local extremum will exist at the origin in field space. Finally, we choose a special setup for the stop soft parameters. Namely that we fix $A_t = (\mu + \lambda v_S)\cot\beta$ so that the off-diagonal elements of eq. (2.14) vanish at the broken minimum. Furthermore, we impose that the stop soft mass parameters are nearly degenerate, $m_{Q_3} - m_{\overline{u}_3} = 100$ GeV. The value of m_{Q_3} is fixed such that we have a suitable Higgs with mass 125 GeV. We then count a total of 11 free parameters in this theory. A brief summary of the free parameters and scan procedure can be found in Appendix B.

2.1.2 At one loop zero temperature

The general form of the one loop zero temperature effective potential in the models we study is

$$V_{1\text{ loop }(0\text{T})}(\phi, S) = V_{\text{tree}}(\phi, S) + V_{\text{CT}}(\phi, S) + V_{\text{CW}}(\phi, S), \tag{2.16}$$

where $\phi = \text{Re}(\text{H}^0)$ is the SM-like Higgs field and S is a singlet field under each of the SM gauge groups. The individual terms are given by

$$\begin{aligned} V_{\text{tree}}(\phi, S) &= -\mu_0^2\phi^2 + \lambda_0\phi^4 + V_{\text{tree}}^{[\text{non-SM}]}(\phi, S), \\ V_{\text{CT}}(\phi, S) &= \frac{1}{2}\delta m_\phi^2\phi^2 + \frac{1}{2}\delta m_S^2 S^2 + \frac{1}{4}\delta\lambda_0\phi^4, \\ V_{\text{CW}}(\phi, S) &= \frac{1}{(8\pi)^2}\sum_i g_i(-1)^{2s_i} m_i^4(\phi, S)\left[\log\left(\frac{m_i^2(\phi, S)}{Q^2}\right) - \frac{3}{2}\right], \end{aligned} \tag{2.17}$$

where the δ's are the one loop counter terms (CT) and the index i runs over all bosons and fermions, with g_i degrees of freedom and spin s_i, considered at one loop. Note that we use the Coleman-Weinberg (CW) effective potential in the modified DR scheme [66] and Q is the renormalisation scale, chosen to be the mass of the top quark, m_t, throughout this investigation. We will adopt the convention that the VEVs of ϕ and S in the broken vacuum at zero temperature are given by $\langle\phi\rangle = v = 174.2$ GeV and $\langle S\rangle = v_S$, respectively, and denote the pole mass of the i^{th} particle by $m_i = m_i(\phi = v, S = v_S)$.

We choose the renormalisation conditions

$$\left.\frac{\partial V_{\text{tree}}}{\partial \phi}\right|_{\text{broken}} = \left.\frac{\partial V_{1\text{ loop (0T)}}}{\partial \phi}\right|_{\text{broken}}, \tag{2.18}$$

$$\left.\frac{\partial V_{\text{tree}}}{\partial S}\right|_{\text{broken}} = \left.\frac{\partial V_{1\text{ loop (0T)}}}{\partial S}\right|_{\text{broken}}, \tag{2.19}$$

$$\left.\frac{\partial^2 V_{\text{tree}}}{\partial \phi^2}\right|_{\text{broken}} = \left.\frac{\partial^2 V_{1\text{ loop (0T)}}}{\partial \phi^2}\right|_{\text{broken}}. \tag{2.20}$$

The condition in eq. (2.20) means that the Higgs mass is unchanged upon radiative corrections. This condition cannot be applied to the GNMSSM due to the tree level bound on the lightest CP-even Higgs state. Therefore the $\delta\lambda_0$ counter term in eq. (2.17) is not included as part of the renormalisation conditions for the GNMSSM. The other two conditions keep the VEVs in the broken vacuum the same at one loop as their tree level values. Note that we have chosen renormalisation conditions only in the broken phase, which is sufficient for our purpose. For a more general analysis, including renormalisation conditions related to the symmetric phase, see ref. [25].

2.1.3 At one loop finite temperature

In order to study cosmological phase transitions in a quantum field theory framework, the one loop effective potential ought to take into account a temperature-dependent piece. We include thermal corrections at one loop, such that the thermal effective potential reads

$$V_{1\text{ loop}}(\phi, S; T) = V_{1\text{ loop (0T)}}(\phi, S) + V_{\text{T}}(\phi, S; T), \tag{2.21}$$

where [67]

$$V_{\text{T}}(\phi, S; T) = \sum_{i=f,b}^{\infty} \frac{(-1)^{2s_i} g_i T^4}{2\pi^2} \int_0^{\infty} dx x^2 \log\left[1 + (-1)^{2s_i+1} \exp\left(-\sqrt{x^2 + \frac{m_i^2(\phi, S)}{T^2}}\right)\right], \tag{2.22}$$

and T is the temperature of the surrounding plasma. The sum is over all relevant fermions and bosons in the plasma. Rather than numerically evaluating the integral in eq. (2.22), we will use the potential in the form of a piecewise function built up of three parts, as described below. Each part is determined by the value of $m_i(\phi, S)/T$ for each particle. Note that we are going to mostly focus on the limit of very strong phase transitions, where thermal resummations [68] of the potential do not play a crucial role, so we ignore these for now. In Section 2.4 we briefly investigate the effect of a one loop resummation.

The potential in eq. (2.22) can be rewritten into an analytic form within two approx-

imations: a low temperature limit, where $m_i(\phi, S)/T$ is large, and a high temperature limit, where $m_i(\phi, S)/T$ is small [67, 69]. We use interpolation functions for intermediate temperatures, during which the low and high temperature approximations differ from the exact value by no more than 4%. The interpolation functions are numerical fits determined in [70]. The analytic form of these finite temperature contributions depends on whether the i^{th} particle is a boson or a fermion. Notably, only bosonic thermal contributions contain temperature-dependent cubic terms which may alter the strength of the phase transition. All field-dependence appears through the field-dependent mass of the contributing particle, $m_i(\phi, S)$. For simplicity, we have omitted writing in the explicit field-dependence of the $m_{f/b}$ mass terms in the piecewise expressions below. The expression for an individual fermionic thermal contribution is

$$V_T^{(f)} = g_f T^4 \times \begin{cases} \frac{1}{48}\left(\frac{m_f}{T}\right)^2 + \frac{1}{(8\pi)^2}\left(\frac{m_f}{T}\right)^4 \ln\left[\frac{m_f^2}{c_f T^2}\right], & \text{for } \frac{m_f}{T} < 1.1, \\ \frac{-0.6087 + 0.0856\left(\frac{m_f}{T}\right)}{6.321 - 0.725\left(\frac{m_f}{T}\right) + \left(\frac{m_f}{T}\right)^2}, & \text{for } 1.1 < \frac{m_f}{T} < 3.4, \\ \left(\frac{m_f}{2\pi T}\right)^{3/2} \exp\left(-\frac{m_f}{T}\right)\left(1 + \frac{15}{8}\frac{T}{m_f}\right), & \text{for } \frac{m_f}{T} > 3.4. \end{cases} \tag{2.23}$$

The expression for an individual bosonic thermal contribution is

$$V_T^{(b)} = g_b T^4 \times \begin{cases} \frac{1}{24}\left(\frac{m_b}{T}\right)^2 - \frac{1}{12\pi}\left(\frac{m_b}{T}\right)^3 - \frac{1}{(8\pi)^2}\left(\frac{m_b}{T}\right)^4 \ln\left[\frac{m_b^2}{c_b T^2}\right], & \text{for } \frac{m_b}{T} < 1.8, \\ \frac{-0.3904 + 0.0507\left(\frac{m_b}{T}\right)}{5.219 - 1.885\left(\frac{m_b}{T}\right) + \left(\frac{m_b}{T}\right)^2}, & \text{for } 1.8 < \frac{m_b}{T} < 4.5, \\ \left(\frac{m_b}{2\pi T}\right)^{3/2} \exp\left(-\frac{m_b}{T}\right)\left(1 + \frac{15}{8}\frac{T}{m_b}\right), & \text{for } \frac{m_b}{T} > 4.5, \end{cases} \tag{2.24}$$

where $\log(c_b) = 5.41$ and $\log(c_f) = 2.64$ [67, 69]. For early universe considerations, such as electroweak baryogenesis, we are interested in the strength of the phase transition. In this work, the critical temperature is defined as the temperature at which the electroweak broken and symmetric vacua are degenerate. Given our chosen VEV convention, a strong phase transition is defined[2] by $\xi \equiv \sqrt{2}\, v_c/T_c \gtrsim 1$. Here v_c is the value of the ϕ field in the broken vacuum at critical temperature T_c. Note that here we have dropped the subscript "c" for convenience, as it is always evaluated at critical temperature for this work.

[2]The factor of $\sqrt{2}$ accounts for the chosen normalisation of the Higgs field. This condition satisfies the baryon preservation criteria [21, 22].

2.2 The vacuum energy difference

We define the one loop vacuum energy difference at zero temperature between the broken vacuum and symmetric extremum to be

$$\begin{aligned}\Delta V_{1\text{ loop (0T)}} &= V_{1\text{ loop (0T)}}\big|_{\text{broken}} - V_{1\text{ loop (0T)}}\big|_{\text{symmetric}} \\ &= V_{1\text{ loop (0T)}}(v, v_S) - V_{1\text{ loop (0T)}}(0, \tilde{v}_S) \\ &= \Delta V_{\text{tree}} + \Delta V_{\text{rad}},\end{aligned} \tag{2.25}$$

where we have defined the quantities

$$\begin{aligned}\Delta V_{\text{tree}} = &\quad V_{\text{tree}}(v, v_S) - V_{\text{tree}}(0, \tilde{v}_S), \\ \Delta V_{\text{rad}} = &\quad [V_{\text{CT}} + \Delta V_{\text{CW}}](v, v_S) - [V_{\text{CT}} + \Delta V_{\text{CW}}](0, \tilde{v}_S),\end{aligned} \tag{2.26}$$

and $\tilde{v}_S$ is the value of the singlet field S in the symmetric extremum. Note that the vacuum energy difference takes on negative values if the broken vacuum is the global minimum of the potential.

The potential difference between the symmetric and broken extrema is temperature-dependent. The critical temperature is defined as the temperature at which this potential difference is zero. The hypothesis we want to investigate in the following work is:

The smaller the value of $|\Delta V_{1\text{ loop (0T)}}|$*, the stronger the phase transition.*

A decrease in $|\Delta V_{1\text{ loop (0T)}}|$ is expected to decrease the critical temperature and therefore increase the strength of the phase transition ξ. The concept of the vacuum energy difference is a more precise prescription of the notion of "flat potentials" in ref. [54].

As we will see below, the one loop vacuum energy difference is often simply related to the free parameters of the models we investigate. In each model, we consider one loop (zero temperature and thermal) contributions from the top quark, t, and the EW gauge bosons, $W^{\pm}$ and Z^0. In the GNMSSM, we also consider the one loop (zero temperature and thermal) contributions from the stops, $\tilde{t}_1$ and $\tilde{t}_2$, the supersymmetric partners of the SM top quark.

In this work we approximate the effective potential at one loop. The impact of higher loop orders on the effective potential is model dependent. We expect higher loop order corrections to be more relevant for Coleman-Weinberg type models, where radiative cor-

rections play a large role in determining the shape of the potential. This is not the case for parameter points with a weaker phase transition, such as the SM, since the depth of the broken vacuum is effectively set by the observed Higgs mass. A possible exception is the GNMSSM, where the Higgs mass receives crucial one loop contributions. For a weak phase transition in singlet extensions, the potential at the symmetric extremum is very close to the potential value at the origin. Loop effects could restore the symmetry in the singlet direction and we would no longer be able to realise the necessary vacuum structure to lower the difference between the two extrema. Note that any loop effects affecting this structure would come with an S-dependence only because $\phi = 0$.

Higher loop order corrections could have a large impact on potentials with a very small vacuum energy difference, i.e. the broken and symmetric extrema are close to degeneracy at zero temperature. We expect this to happen for very finely-tuned regions of parameter space. Overall, we do not expect higher loop effects to have much impact on the depth of the broken vacuum or symmetric extremum, unless they are close to degeneracy. This is the region that we hypothesise as providing the strongest phase transitions.

Note that we should remain cautious regarding the gauge-dependence of our results [71–73]. Interestingly enough, ref. [74, 75] suggests that for certain models the potential evaluated at its true minimum is gauge-*invariant* at one-loop. Such works ought to be taken further to quantify whether this is true for each model we explore.

2.2.1 The vacuum energy difference in single field models

Here we apply the minimum condition and use the Higgs mass to rewrite the quartic coupling. In the SM, this means $\mu_0^2 = 2\lambda_0 v^2$ and $m_h^2 = 4\lambda_0 v^2$. We then read off the tree level vacuum energy difference as

$$\Delta V_{\text{tree}}^{[\text{SM}]} = -\lambda_0 v^4 = -\frac{1}{4} m_h^2 v^2. \tag{2.27}$$

Including the top quark, $W^\pm$, and Z^0-boson one loop corrections, we find the one loop zero temperature vacuum energy difference to be

$$\begin{aligned} \Delta V_{\text{1 loop (0T)}}^{[\text{SM}]} &= -\frac{1}{4} m_h^2 v^2 - \frac{2}{(16\pi)^2} \left(g_t m_t^4 - g_W m_W^4 - g_Z m_Z^4 \right) \\ &= -1.185 \times 10^8 \text{ GeV}^4 - \frac{2}{(16\pi)^2} \left(g_t m_t^4 - g_W m_W^4 - g_Z m_Z^4 \right) \\ &= -1.267 \times 10^8 \text{ GeV}^4. \end{aligned} \tag{2.28}$$

We see that quantum corrections do not drastically affect the vacuum energy difference in the SM. The top quark dominates the radiative correction and decreases the vacuum energy difference by 7.2%. Including the EW gauge bosons, it decreases by 6.9%. In other words, the vacuum energy difference in the SM is effectively set by the Higgs mass (the tree level contribution).

Let us repeat this procedure for other extensions of the SM. For the SM with a dimension-six term

$$\Delta V_{\text{1 loop (0T)}}^{[\text{SM}+\phi^6]} = -\frac{1}{4}m_h^2 v^2 + \frac{v^6}{M^2} - \frac{2}{(16\pi)^2}\left(g_t m_t^4 - g_W m_W^4 - g_Z m_Z^4\right), \tag{2.29}$$

for the SM from GMESB

$$\Delta V_{\text{1 loop (0T)}}^{[\text{SM}+\log]} = -\frac{1}{2}m_h^2 v^2 + \lambda_0 v^4, \tag{2.30}$$

and for the SM with an additional CW scalar

$$\Delta V_{\text{1 loop (0T)}}^{[\text{SM}+\text{scalar}]} = -\frac{1}{4}m_h^2 v^2 - \frac{2}{(16\pi)^2}\left(g_t m_t^4 - g_W m_W^4 - g_Z m_Z^4 - y^4 v^4\right). \tag{2.31}$$

In all these models the vacuum energy difference can be chosen independently of the Higgs mass, using the remaining free parameter.

2.2.2 The vacuum energy difference (xSM)

Applying the minimum conditions in the broken vacuum,

$$\left.\frac{\partial V_{\text{tree}}^{[\text{xSM}]}}{\partial \phi}\right|_{\text{broken}} = 0 \quad \text{and} \quad \left.\frac{\partial V_{\text{tree}}^{[\text{xSM}]}}{\partial S}\right|_{\text{broken}} = 0,$$

we find

$$\mu^2 = 2\lambda_0 v^2 - \left(\frac{a_1}{2v_S} + \frac{a_2}{2}\right)v_S^2 \quad \text{and} \quad b_2 = -\left(\frac{a_1}{2v_S} + a_2\right)v^2 - \left(\frac{b_3}{v_S} + b_4\right)v_S^2.$$

This gives us a tree level vacuum energy difference of

$$\begin{aligned}\Delta V_{\text{tree}}^{[\text{xSM}]} = \; & -\lambda_0 v^4 - \left[\left(\frac{a_1}{2v_S} + a_2\right)v^2 + \frac{b_4}{2}\left(v_S^2 - \tilde{v}_S^2\right)\right]\left(\frac{v_S^2 - \tilde{v}_S^2}{2}\right) \\ & -\frac{b_3}{6}\left(v_S - \tilde{v}_S\right)^2\left(v_S + 2\tilde{v}_S\right),\end{aligned} \tag{2.32}$$

where the singlet VEV in the symmetric vacuum is given by

$$\tilde{v}_S = -\frac{b_3}{2b_4} \pm \sqrt{\left(\frac{b_3}{2b_4}\right)^2 - \frac{b_2}{b_4}}. \tag{2.33}$$

The sign in eq. (2.33) is determined by whichever minimum has the lowest value of the potential. All one loop contributions considered here are the same as those in the SM. The one loop zero temperature vacuum energy difference is therefore given by

$$\begin{aligned} \Delta V^{[\text{xSM}]}_{1\text{ loop (0T)}} = \quad & -\lambda_0 v^4 - \frac{2}{(16\pi)^2}\left(g_t m_t^4 - g_W m_W^4 - g_Z m_Z^4\right) \\ & - \left[\left(\frac{a_1}{2v_S} + a_2\right) v^2 + \frac{b_4}{2}\left(v_S^2 - \tilde{v}_S^2\right)\right]\left(\frac{v_S^2 - \tilde{v}_S^2}{2}\right) \\ & - \frac{b_3}{6}\left(v_S - \tilde{v}_S\right)^2\left(v_S + 2\tilde{v}_S\right). \end{aligned} \tag{2.34}$$

The first line of eq. (2.34) is algebraically identical to the SM vacuum energy difference at one loop prior to fixing λ_0 in favour of the SM Higgs mass, m_h. Note that in the case of $\tilde{v}_S = v_S$, we recover the SM result.

We rewrite the quartic terms, a_2 and b_4, in favour of the CP-even mass eigenstates, m_{ϕ_1} and m_{ϕ_2}, where $m_{\phi_1} < m_{\phi_2}$,

$$m^2_{\phi_1,\phi_2} = \frac{M_{11}^2 + M_{22}^2}{2} \mp \sqrt{\left(\frac{M_{11}^2 - M_{22}^2}{2}\right)^2 + M_{12}^4}, \tag{2.35}$$

and the scalar mass squared matrix is given by

$$M^2 = \begin{pmatrix} 4\lambda_0 v^2 & v_S v\left(\frac{a_1}{2v_S} + a_2\right) \\ v_S v\left(\frac{a_1}{2v_S} + a_2\right) & -\frac{a_1 v^2}{4v_S} + v_S^2\left(\frac{b_3}{2v_S} + b_4\right) \end{pmatrix}. \tag{2.36}$$

This is in agreement with ref. [48]. Note that our chosen particle content in the loop and renormalisation conditions prevent the above matrix from changing at the broken minimum upon the inclusion of one loop effects. Using expressions in the form

$$\frac{m^2_{\phi_1} + m^2_{\phi_2}}{2} = \frac{M_{11}^2 + M_{22}^2}{2}, \tag{2.37}$$

$$\left(\frac{m_{\phi_2}^2 - m_{\phi_1}^2}{2}\right)^2 = \left(\frac{M_{11}^2 - M_{22}^2}{2}\right)^2 + M_{12}^4, \tag{2.38}$$

both m_{ϕ_1} and m_{ϕ_2} are recognised with the SM-like Higgs mass and singlet mass (m_h and m_s, respectively) depending on the ordering of their mass values. Therefore

$$(a_2)_\pm = -\frac{a_1}{2v_S} \pm \frac{1}{v_S v}\sqrt{\left(m_{\phi_1}^2 - 4\lambda_0 v^2\right)\left(4\lambda_0 v^2 - m_{\phi_2}^2\right)} \text{ and} \tag{2.39}$$

$$b_4 = \frac{1}{v_S^2}\left[m_{\phi_1}^2 + m_{\phi_2}^2 - 4\lambda_0 v^2 + \frac{a_1}{2}\frac{v^2}{v_S} - \frac{b_3}{3}v_S\right]. \tag{2.40}$$

Given that the quartic coupling, a_2, must be a real-valued quantity, we find

$$m_{\phi_1}^2 \leq 4\lambda_0 v^2 \leq m_{\phi_2}^2. \tag{2.41}$$

Altogether, we find the one loop zero temperature vacuum energy difference to be

$$\begin{aligned}\Delta V_{1\text{ loop }(0\text{T})}^{[\text{xSM}]} = \quad & -\lambda_0 v^4 - \left[\pm\frac{v}{v_S}\sqrt{(m_h^2 - 4\lambda_0 v^2)(4\lambda_0 v^2 - m_s^2)}\right. \\ & \left. + \frac{1}{2}\left(m_h^2 + m_s^2 - 4\lambda_0 v^2 + \frac{a_1 v^2}{2v_S} - \frac{b_3}{3}v_S\right)\left(1 - \frac{\tilde{v}_S^2}{v_S^2}\right)\right]\left(\frac{v_S^2 - \tilde{v}_S^2}{2}\right) \\ & - \frac{b_3}{6}\left(v_S - \tilde{v}_S\right)^2\left(2\tilde{v}_S + v_S\right) - \frac{2}{(16\pi)^2}\left(g_t m_t^4 - g_W m_W^4 - g_Z m_Z^4\right).\end{aligned} \tag{2.42}$$

Identifying the free parameters, the above expression contains the two cubic terms (a_1 and b_3), two physical Higgs masses (m_h and m_s), three VEVs (v, v_S and $\tilde{v}_S$), and the quartic Higgs self-coupling (λ_0). We can again see that we are free to choose the vacuum energy difference, via the free parameters of the model, despite the Higgs mass being fixed.

$\mathbb{Z}_2$ symmetric case (with broken $\mathbb{Z}_2$ at zero temperature)

By imposing a $\mathbb{Z}_2$ discrete symmetry on the singlet the cubic terms vanish, giving a model referred to as the $\mathbb{Z}_2$xSM. Setting the cubic terms to zero in eq. (2.42), we find a simple expression for the one loop vacuum energy difference at zero temperature,

$$\Delta V_{1\text{ loop }(0\text{T})}^{[\mathbb{Z}_2\text{xSM}]} = -\frac{1}{4}m_h^2 v^2\left(1 + \frac{m_h^2 - 4\lambda_0 v^2}{m_s^2}\right)^{-1} - \frac{2}{(16\pi)^2}\left(g_t m_t^4 - g_W m_W^4 - g_Z m_Z^4\right). \tag{2.43}$$

Note that this expression assumes that v_S is non-zero, so the $\mathbb{Z}_2$ symmetry is spontaneously broken. This expression is almost identical to the SM expression in eq. (2.28) with the exception of a multiplicative factor on the tree level term. For this factor to be less than

one we must have $4\lambda_0 v^2 \leq m_h^2$, hence $m_s < m_h$ is the only way in which a vacuum energy difference higher than the SM can be obtained. A strange feature is that eq. (2.43) is independent of the potential's structure in the singlet direction: only m_s and λ_0 appear as free parameters in the vacuum energy difference.

Let us replace λ_0 by a new parameter, ϵ, defined by

$$4\lambda_0 v^2 = \epsilon m_h^2 + (1-\epsilon) m_s^2. \tag{2.44}$$

The inequality of eq. (2.41) translates into $0 \leq \epsilon \leq 1$. This allows us to rewrite the vacuum energy difference in the $\mathbb{Z}_2$xSM model as

$$\Delta V_{\text{1 loop (0T)}}^{[\mathbb{Z}_2\text{xSM}]} = -\frac{1}{4}\left[\frac{m_h^2 m_s^2}{(1-\epsilon)m_h^2 + \epsilon m_s^2}\right] v^2 - \frac{2}{(16\pi)^2}\left(g_t m_t^4 - g_W m_W^4 - g_Z m_Z^4\right). \tag{2.45}$$

The lowest value for $|\Delta V_{\text{1 loop (0T)}}^{[\mathbb{Z}_2\text{xSM}]}|$ is bounded by the one loop contribution. This happens when the tree level contribution vanishes, which is only possible if m_s goes to zero. We can rewrite eq. (2.36) into a more useful form, where the Higgs mass squared elements' dependence on m_h^2, m_s^2, and ϵ is explicit. In the gauge eigenstate basis, the scalar mass squared matrix is given by

$$M^2 = \begin{pmatrix} \epsilon m_h^2 + (1-\epsilon) m_s^2 & \pm\sqrt{\epsilon(1-\epsilon)}(m_h^2 - m_s^2) \\ \pm\sqrt{\epsilon(1-\epsilon)}(m_h^2 - m_s^2) & (1-\epsilon)m_h^2 + \epsilon m_s^2 + \dfrac{a_1 v^2}{4 v_S} - \dfrac{b_3}{6} v_S \end{pmatrix}. \tag{2.46}$$

Furthermore, we can rewrite the tree level potential such that the importance of ϵ is clearer,

$$\begin{aligned} V_{\text{tree}}^{[\mathbb{Z}_2\text{xSM}]} = \; & \frac{1}{2} m_h^2 \left[\left(\frac{\phi^2}{2v^2} - 1\right)\phi^2 \epsilon + \left(\frac{S^2}{2v_S^2} - 1\right) S^2 (1-\epsilon)\right] \\ & + \frac{1}{2} m_s^2 \left[\left(\frac{S^2}{2v_S^2} - 1\right) S^2 \epsilon + \left(\frac{\phi^2}{2v^2} - 1\right)\phi^2 (1-\epsilon)\right] \\ & \pm \frac{1}{2}(m_h^2 - m_s^2)\sqrt{\epsilon(1-\epsilon)}\left[\frac{v_S}{v}\phi^2 + \frac{v}{v_S} S^2 - \frac{1}{v_S v}\phi^2 S^2\right]. \end{aligned} \tag{2.47}$$

In the limit that $\epsilon \to 1$ ($\epsilon \to 0$) the tree level potential collapses to a massive Φ^4-theory, where $\Phi \to \phi$ ($\Phi \to S$). The other piece of the potential corresponds to an invisible sector that is phenomenologically inaccessible since the ϕ and S fields no longer mix. Thus we

expect the $\mathbb{Z}_2$xSM to behave in a similar manner to the massive ϕ^4 theory close to these limits. Taking the tree level piece of eq. (2.45) and solving for the singlet's mass, we find

$$m_s = m_h \left(1 + \frac{1}{1-\epsilon}\left[\frac{\Delta V_{\text{tree}}^{[\text{SM}]}}{\Delta V_{\text{tree}}^{[\mathbb{Z}_2\text{xSM}]}} - 1\right]\right)^{-1/2}. \tag{2.48}$$

If we take $\Delta V_{\text{tree}}^{[\mathbb{Z}_2\text{xSM}]} \to 0$, then eq. (2.48) suggests that the singlet's mass vanishes irrespective of the value of ϵ. For the case of $\epsilon = 0$, the singlet mass is determined by the vacuum energy difference, since $\Delta V_{\text{tree}}^{[\mathbb{Z}_2\text{xSM}]} = -m_s^2 v^2/4$. For the case of $\epsilon = 1$, it naively appears that the singlet mass must be zero and we recover the SM. However, there is one special parameter choice that allows the SM Higgs and singlet fields to coexist. This happens if $v_S = 0$, whereby the two fields decouple yet the mixing term does not disappear. The limit $\epsilon \to 1$ in eq. (2.48) is no longer so trivial.

$\mathbb{Z}_2$ symmetric case (with unbroken $\mathbb{Z}_2$ at zero temperature)

In the special case of a $\mathbb{Z}_2$ symmetry with $v_S = 0$, the minimum conditions are different to the previous case. This change in minimum conditions modifies many of the previous expressions. Firstly, the pure ϕ couplings would be the same as those in the SM, $m_h^2 = 2\mu_0^2$ and $\lambda_0 = m_h^2/(4v^2)$, since the singlet VEV is zero in the broken phase. This is equivalent to setting $\epsilon = 1$ in eq (2.44). Secondly, we can express b_4 in terms of the VEV of the singlet field in the symmetric vacuum, $b_4 = -b_2/\tilde{v}_S^2$. The vacuum energy difference is given by

$$\Delta V_{1\text{ loop (0T)}}^{[\mathbb{Z}_2\text{xSM}]} = -\frac{1}{4}m_h^2 v^2 - \frac{1}{4}b_2\tilde{v}_S^2 - \frac{2}{(16\pi)^2}\left(g_t m_t^4 - g_W m_W^4 - g_Z m_Z^4\right). \tag{2.49}$$

Compared to the SM vacuum energy difference there is an extra tree level piece in eq. (2.49), which has the opposite sign to the SM piece if $b_2 < 0$. In other words, the tree level contribution to the vacuum energy difference will be reduced compared to the SM if $\tilde{v}_S \neq 0$. Since the overall size of this extra term determines the vacuum energy difference, we should investigate this term more closely. Rewriting b_2 in terms of the singlet mass and coupling a_2,

$$b_2 = 2m_s^2 - a_2 v^2, \tag{2.50}$$

we find an upper bound for the singlet mass of $m_s^2 < a_2 v^2/2$. This bound is necessary to decrease $|\Delta V_{1\text{ loop (0T)}}^{[\mathbb{Z}_2\text{xSM}]}|$ compared to the SM value. This implies that in order to have $\tilde{v}_S \neq 0$ and the singlet heavier that the SM Higgs, $m_s > m_h$, we require a relatively large coupling $a_2 \gtrsim 1$. From perturbative unitarity arguments the maximum value of a_2 is about

8π [76], which translates to an upper bound for the singlet mass of $m_s \sim 600$ GeV. The singlet mass in the unbroken $\mathbb{Z}_2$ case is given by

$$m_s = \sqrt{\frac{1}{2}a_2 v^2 + \frac{2}{\tilde{v}_S^2}\left(\Delta V_{\text{tree}}^{[\text{SM}]} - \Delta V_{\text{tree}}^{[\mathbb{Z}_2\text{xSM}]}\right)}. \tag{2.51}$$

In contrast to eq. (2.48), the singlet mass does not vanish as we take $\Delta V_{\text{tree}}^{[\mathbb{Z}_2\text{xSM}]} \to 0$. In order for the singlet mass to be positive within this limit, it is required that $a_2\tilde{v}_S^2 > m_h^2$. Given the maximum value of $a_2 \sim 8\pi$, we find that $|\tilde{v}_S| \gtrsim 25$ GeV. The $a_2 v^2/2$ term in eq. (2.51) protects the mass of the singlet from vanishing as $\Delta V_{\text{tree}}^{[\mathbb{Z}_2\text{xSM}]} \to 0$. Consequently, the behaviour in taking the vacuum energy difference to zero in the unbroken $\mathbb{Z}_2$ case differs drastically compared to the behaviour in the broken $\mathbb{Z}_2$ case.

2.2.3 The vacuum energy difference (GNMSSM)

To the tree level potential, we apply the usual minimal conditions to eliminate the $m_{H_u}^2$, $m_{H_d}^2$, and m_S^2 soft mass parameters in favour of $\tan\beta$ and the VEVs, v and v_S. The rest of the analytic work that we concern ourselves with regards the potential in the real singlet direction, $s = \text{Re(S)}$, defined as the potential at $H_u = H_d = 0$. The resulting potential takes the form

$$V_{\text{tree (singlet)}}^{[\text{GNMSSM}]} = \; k_1^2 + [m_S^2 + k_2(A_{k_2} + k_2) + k_1 k_3]s^2 + \frac{2}{3}k_3(A_{k_3} + 3k_2)s^3 + k_3^2 s^4, \tag{2.52}$$

where we have chosen $A_{k_1} = -k_2$ in order to remove the linear term in this potential without loss of generality[3]. Solving for the extrema in the singlet direction, we find a trivial extremum at $s = 0$ whose extremum nature depends on the sign of the quadratic term in eq. (2.52). Note that for a potential bounded from below, we can only have three shapes for the potential in the singlet direction:

- Minimum at $s = 0$: this is the only extremum.
- Minimum at $s = 0$: there exist two additional extrema, one maximum and one minimum. Both additional extrema have s-values of the same sign, with the minimum having the greater magnitude of s.
- Maximum at $s = 0$: there exist two additional extrema, both minima, whose s-values have opposite sign.

[3] We can recover an arbitrary value of the chosen parameter by a shift in field s.

In the GNMSSM, we find that the additional extrema are located at

$$\langle s\rangle_{\pm} = -\frac{A_{k_3}+3k_2}{4k_3} \pm \sqrt{\left[\frac{A_{k_3}+3k_2}{4k_3}\right]^2 - \frac{1}{2k_3^2}\left[m_S^2 + k_2(A_{k_2}+k_2) + 2k_1k_3\right]}. \tag{2.53}$$

For three extrema in the singlet direction, this requires the condition that

$$(A_{k_3}+3k_2)^2 - 8\left[m_S^2 + k_2(A_{k_2}+k_2) + 2k_1k_3\right] \geq 0. \tag{2.54}$$

In meeting this condition, assuming small values of k_3, and $A_{k_3} \sim k_2 \sim m_{\rm SUSY}$, there is a strong tendency for an additional minimum to exist at very large singlet field values. This is of course without a tuning of A_{k_3} and k_2. It is interesting to note that a tuning to make the ratio $(A_{k_3}+3k_2)/(k_3)$ smaller is analogous to forcing the effective b_3 trilinear singlet term (as appears in the xSM model) to be zero. To clarify, we can express the ratio in terms of an effective b_3 parameter in place of A_{k_3} and k_2

$$\left|\frac{A_{k_3}+3k_2}{4k_3}\right| \sim \left|\frac{b_3}{8k_3^2}\right|. \tag{2.55}$$

The essential point here is that by capping the additional minimum to less than 10 TeV, small values of $k_3 < 10^{-3}$ set $|b_3| \lesssim 0.1$ GeV. In contrast, large values of $k_3 \sim 1$ allow for a far larger cubic term, $|b_3| \sim 80$ TeV, but at the risk of other complications to the model. Recall that λ and k_3 are the trilinear couplings that appear in the superpotential of eq. (2.8). Namely that both λ and k_3 are large, in tension with theoretical constraints due to the presence of a Landau pole [77]. In the numerical analysis, we consider points for the GNMSSM with a cap of 10 TeV on the singlet VEV in the symmetric extrema and are thus biased toward a large λ and large k_3 parameter space.

2.3 Numerical scan

By means of a numerical scan over a selected parameter space, we look at various distributions related to the variables v_c, T_c, ξ, and $\Delta V_{1\text{ loop }(0\text{T})}$. The scans are conducted with the aim of covering the range of possibilities. Hence the density of parameter points in the plots is not necessarily representative of the statistical likelihood of landing in any particular region. In our numerical analysis, we vary most of the dimensionful parameters between 0 GeV and 1000 GeV to the appropriate power. For details see Appendices A and B.

2.3.1 Phenomenological constraints

For the $\mathbb{Z}_2$xSM and xSM models, we apply the constraints from [78]. This constrains the value of the mixing angle, $|\sin\alpha|$, against the mass of the singlet, m_s. For singlet masses below 80 GeV there is a bound of $|\cos\alpha| \geq 0.985$ ($|\sin\alpha| \leq 0.173$). This bound comes from collider exclusion limits, including LHC Higgs signal rates. For singlet masses between $80-180$ GeV the mixing angle is constrained by LEP and LHC exclusion bounds. For singlet masses greater than 180 GeV, we apply the constraint of quantum corrections to the $W^{\pm}$ boson mass [79]. We expect the validity of the high singlet mass constraint to breakdown in supersymmetric models due to additional particle content contributing to loop corrections. For the GNMSSM, we instead apply a bound of $|\sin\alpha| \leq 0.55$ for parameter points with a singlet mass greater than 180 GeV [80]. We cut out stop masses below $m_{\tilde{t}_2} \leq 95.7$ GeV, in accordance with [81], but our analysis is not sensitive to this choice.

2.3.2 Scan procedure

We produce random parameter configurations by using flat distributions of the parameters, unless stated otherwise (see Appendices A and B). We then test if these points pass theoretical and/or phenomenological constraints. These tests are based upon desired features of the one loop zero temperature potential and mass spectrum. All parameter points are subject to theoretically motivated cuts, such as (i) the broken vacuum is the absolute minimum of the one loop zero temperature effective potential, (ii) positivity and non-degeneracy of all physical squared masses, (iii) positivity of the quartic couplings[4], and (iv) the imaginary singlet direction does not acquire a VEV.

Procedure in the single field model scans

Starting from the one loop zero temperature potential, we scan over regular intervals of the vacuum energy difference, $\Delta V_{1\text{ loop }(0\text{T})}$, whilst recording the corresponding free parameter of the model. Initially taking the minimum and maximum temperature to be 0 GeV to 200 GeV respectively, we use a simple algorithm to iteratively determine the critical temperature. Temperatures are updated according to whether the broken vacuum is higher or lower than the symmetric extremum in the current iteration. The final VEV of ϕ and temperature are recorded as the critical values for each parameter point.

[4] In the xSM, this means $\lambda_0, > 0$ and $b_4 > 0$, but a_2 can have either sign.

Procedure in the xSM

Since the algebraic form of the one loop zero temperature vacuum energy difference is generally quite complicated, we adopt a semi-analytic approach to study this model. Rather than scanning over regular intervals of the one loop vacuum energy difference, we perform a random scan over the free parameters and rely on a set of conditions to ensure the potential is theoretically well-behaved, i.e. bounded from below with the broken vacuum as the absolute minimum. Our numerical work confirms that the expressions for the vacuum energy difference in Section 2.2.2 are correct.

For the $\mathbb{Z}_2$ case, we also randomly assign values to the free parameters in accordance with the ranges in Table A.1 found in Appendix A. For the unbroken $\mathbb{Z}_2$ case, λ_0 is fixed by m_h, and rather than reparameterising, we scan over the remaining quartics, a_2 and b_4, as well as the singlet mass, m_s.

Procedure in the GNMSSM

This model is investigated through an almost entirely numerical manner. The code written to generate GNMSSM parameter points sequentially performs checks at tree, one loop zero temperature, and one loop finite temperature level.

1. **Tree level parameter point scan:**

   (a) Randomly assign a numerical value to the tree level parameters, in accordance with Table B.1 in Appendix B.

   (b) Find A_{k_1} and A_λ such that (i) no linear singlet term exists in the potential (we find $A_{k_1} = -k_2$ is always the case at tree level) and (ii) that the broken vacuum is lower than the minimum value in the ($\phi = 0$) singlet direction.

   (c) Check the mass spectrum of the Higgs sector. Pass any points that find (i) the h^0 state with mass between 0.5×125 GeV and 125 GeV, (ii) the H^0, A^0, and $H^\pm$ states have masses exceeding 200 GeV, and (iii) both singlet-dominant states are positive in mass.

2. **One loop zero temperature parameter point scan:**

   (a) To reduce the number of parameters, we choose the off-diagonal terms of the stop squared-mass matrix to be zero at the minimum, i.e. $A_t = (\mu + \lambda v_S)\cot\beta$. Furthermore, for the diagonal terms we take $m_{Q_3} = m_{\bar{u}_3} + \Delta m_3$, where $\Delta m_3 = 100$ GeV. The phase transition is not affected by these choices since it is not induced by light stops.

(b) Given the range $\Delta m_3 < m_{Q_3} \leq m_{\text{SUSY}}$, we perform a scan over m_{Q_3} until the stop contribution to the one loop potential results in a numerical value of $m_{h^0} = 125$ GeV. All points find m_{h^0} accurate to within ± 0.02 GeV.

3. **One loop finite temperature parameter point scan:**

   (a) Numerically scan over the temperature between 0 GeV and 200 GeV, finding the broken and symmetric extrema at each temperature.

   (b) Reiterate the above step multiple times, closing in on the temperature at which the vacuum energy difference is zero. Record the critical temperature T_c and critical field values: v_c, $(\tan\beta)_c$, $(v_S)_c$, and $(\tilde{v}_S)_c$.

2.3.3 Numerical results

Let us discuss the main qualitative features of the numerical results. These features are best captured by Figures 2.1, 2.2, 2.5, and 2.6. All of these figures show that an increase in the vacuum energy difference at one loop zero temperature increases the strength of the phase transition. However, the precise relation between the strength of the phase transition and the vacuum energy difference requires a detailed investigation.

Single field models

For the single field models investigated, we can understand that the strength of the phase transition ξ increases as a result of two effects. The first is that the broken vacuum at critical temperature remains close to its zero temperature field VEV. The second is that the critical temperature decreases with the magnitude of the vacuum energy difference. So in the limit $|\Delta V_{1\text{ loop }(0\text{T})}| \to 0$,

$$v_c \to v \text{ and } T_c \to 0 \Rightarrow \xi \to \infty. \tag{2.56}$$

Clearly one would expect metastability of the symmetric phase in the limit of large ξ, but this is not the focus of the current discussion. One interesting observation from Figure 2.1 is that there exists a universal behaviour at low values of $|\Delta V_{1\text{ loop }(0\text{T})}|$. To understand the reason for such behaviour we need an expression for the strength at low critical temperature values.

In order to determine an analytic form for the strength of the phase transition we must take care to use the correct analytic limit for the thermal potential. In the cases we investigate, the high temperature expansion is always valid close to the symmetric

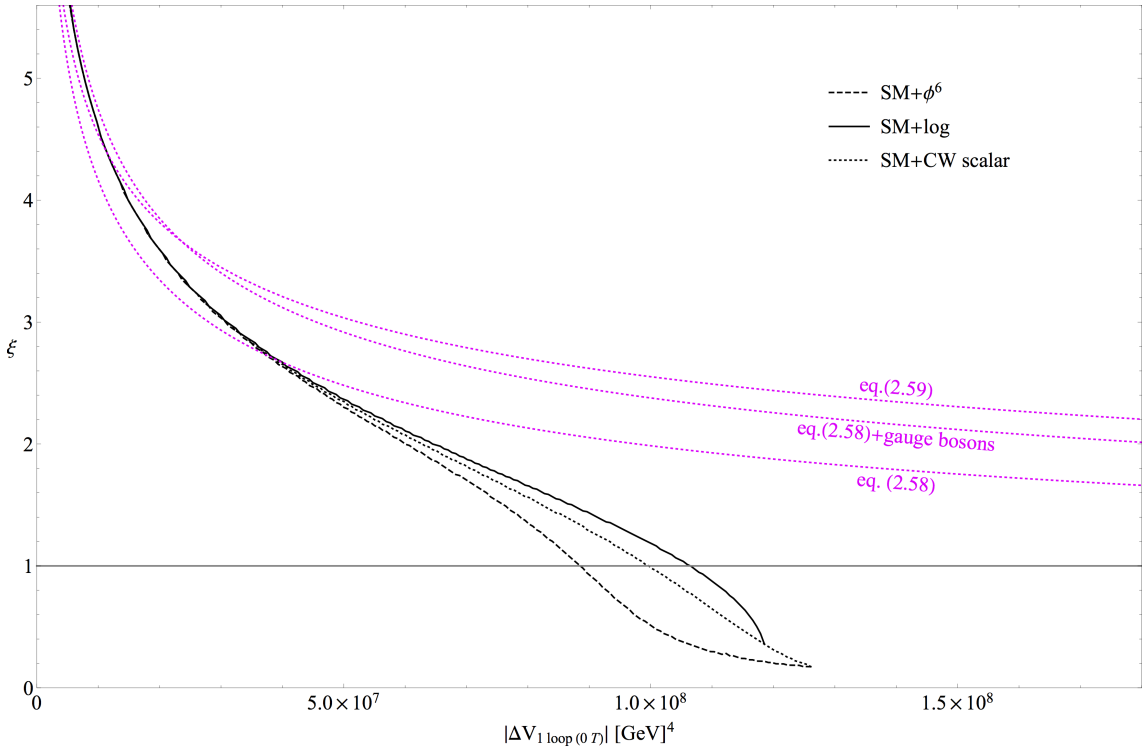

Figure 2.1: Strength of the phase transition, ξ, against the magnitude of the vacuum energy difference, $|\Delta V_{1\ \mathrm{loop}\ (0\mathrm{T})}|$, for the single field models. The magenta curves display the prediction for the strength ξ when the broken minimum is considered in a low temperature expansion. Also shown is the ξ=1 line. Points above this line are considered to have a strong phase transition.

extremum. In terms of the dynamics of increasing temperature, the value of the potential in the symmetric extremum is shifted proportional to T^4. However, in a neighbourhood of the broken vacuum, we are in a low temperature regime. In the low temperature limit, the thermal contribution to the potential is given by [67]

$$\Delta V_{\mathrm{low\ T}}(\phi,T) = \sum_{i=f,b}^{\infty} g_i T^4 \left(\frac{m_i(\phi)}{2\pi T}\right)^{3/2} \exp\left(-\frac{m_i(\phi)}{T}\right)\left(1+\frac{15}{8}\frac{T}{m_i(\phi)}\right). \tag{2.57}$$

In the cases we consider in Figure 2.1, the top quark contribution dominates the expression in eq. (2.57) and so we will neglect the contribution from the EW gauge bosons. Since the vacuum energy difference is zero at the critical temperature, one may equate the required thermal contribution to the vacuum energy difference with the zero temperature value. Assuming $v_c \approx v$ for parameter regions with a low critical temperature, we can derive an equation for ξ as follows

$$\frac{|\Delta V_{1\ \mathrm{loop}\ (0\mathrm{T})}|}{4v^4} \approx g_t \xi^{-4}\left[\frac{7\pi^2}{720} - \left(\frac{y_t}{\sqrt{2}}\frac{\xi}{2\pi}\right)^{3/2}\exp\left(-\frac{y_t}{\sqrt{2}}\xi\right)\left(1+\frac{15}{8}\frac{\sqrt{2}}{y_t\xi}\right)\right], \tag{2.58}$$

where $g_t = 12$ is the number of degrees of freedom of the top quark. Taking the limit that

the strength ξ is very large, the exponential term suppresses all ξ-dependent terms inside the square bracket in eq. (2.58). The strength of the phase transition is then estimated by

$$\xi \approx \sqrt{2}v \left(\frac{7\pi^2}{720} \frac{g_t}{|\Delta V_{1 \text{ loop } (0\text{T})}|} \right)^{1/4} . \tag{2.59}$$

The approximations in eqs. (2.58) and (2.59) are shown in Figure 2.1 and reproduce our numerical result reasonably well for large values of ξ. As ξ becomes larger than about 5, also the gauge bosons will reach a low temperature regime in the broken phase and should be included. Adding them in eq. (2.58) leads to a slightly better approximation labelled as "eq. (2.58)+gauge bosons" in Figure 2.1. So for very strong phase transitions, the observed universal behaviour is fixed by the number of relevant degrees of freedom in the plasma. These are the particles which become massless in the symmetric phase and Boltzmann suppressed in the broken phase. Finally, we can use eq. (2.59) to derive a simple estimate for the critical temperature,

$$T_c \approx \left(\frac{720}{7\pi^2 g_t} |\Delta V_{1 \text{ loop } (0\text{T})}| \right)^{1/4} . \tag{2.60}$$

In order to guarantee a strong phase transition for each of the single field modifications to the SM, we find bounds on each of the free parameters (see Table 2.1). For the SM with a dimension-six operator, the mass suppression favouring a low scale cutoff has been studied in ref. [46, 47]. These translate as bounds on the vacuum energy difference of

$$|\Delta V_{1 \text{ loop } (0\text{T})}| < \begin{cases} 8.83 \times 10^7 \text{ GeV}^4 & \text{for the SM} + \phi^6, \\ 1.06 \times 10^8 \text{ GeV}^4 & \text{for the SM} + \text{log}, \\ 9.95 \times 10^7 \text{ GeV}^4 & \text{for the SM} + \text{CW scalar}. \end{cases} \tag{2.61}$$

Each hints at the necessity for below TeV scale physics and additional scalar states/extended Higgs sectors. It is interesting to note that a very mild modification of the vacuum energy by about 25% is sufficient to induce a strong first order phase transition.

Model:	SM+ϕ^6	SM+log	SM+CW scalar
Free parameter:	M	λ_0	y
Bound:	< 854 GeV	> 0.142	> 2.47

Table 2.1: Bounds on the free parameters in the single field models that guarantee a strong phase transition.

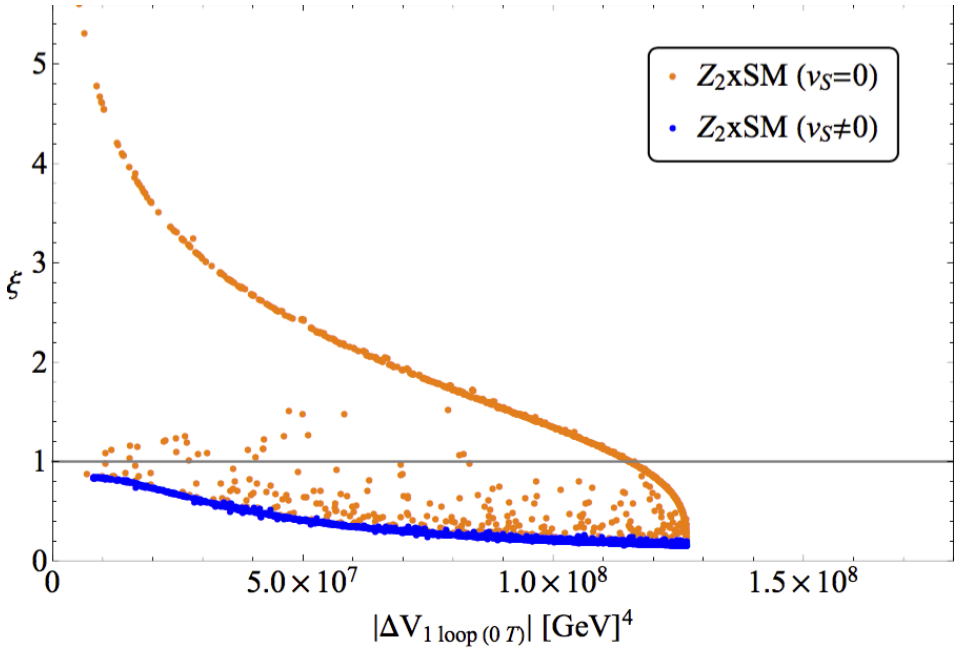

(a) Without phenomenological constraints.

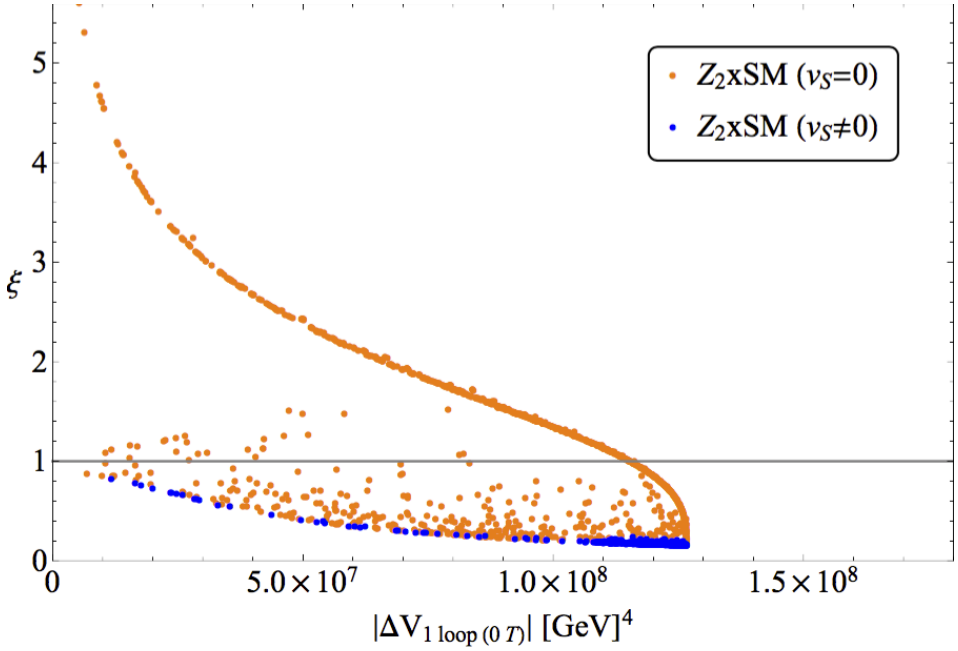

(b) With phenomenological constraints.

Figure 2.2: Strength of the phase transition, ξ, against the magnitude of the vacuum energy difference, $|\Delta V_{1\text{ loop }(0\text{T})}|$, for the $\mathbb{Z}_2$xSM ($v_S = 0$) and $\mathbb{Z}_2$xSM ($v_S \neq 0$) singlet extensions. Also shown is the ξ=1 line.

Non-supersymmetric singlet extension

Next we will remark on Figure 2.2, which shows parameter points for the $\mathbb{Z}_2$xSM, where the $\mathbb{Z}_2$ symmetry is either spontaneously broken ($v_S \neq 0$) or unbroken ($v_S = 0$) at zero temperature. The universal behaviour seen in Figure 2.1 is also observed for a number of parameter points in the unbroken case. However, there are some parameter points that do

not follow this universal curve and instead fall somewhere between this curve and another branch. This other branch happens to be traced out by all points in the spontaneously broken case. Unfortunately, this second branch fails to meet the hypothesis that the phase transition becomes strong (let alone arbitrarily strong) as $|\Delta V_{1\text{ loop }(0\text{T})}|$ is decreased.

This second branch exists because the second derivative of the broken vacuum changes sign in one direction as the potential is thermally evolved to the critical temperature. This is to say that we lose control over the broken vacuum and it no longer remains close to its zero temperature location in field space. Instead the broken vacuum slides quickly across field space upon small changes in temperature. In such scenarios, we observe that the broken vacuum always slides toward the symmetric phase as the temperature is increased. This sliding of the broken vacuum is analogous to saying that the tree level barrier between the symmetric and broken vacua virtually disappears. The only barrier remaining is that generated through the cubic terms of the EW gauge bosons. The phase transition is therefore SM-like with the physical Higgs mass replaced by its value at $\phi = 0$ and $S = \tilde{v}_S$. See Section 4.1.4 in the final chapter for more details. To avoid such scenarios, one must ensure that the Higgs squared mass matrix is always positive in a neighbourhood of the broken vacuum. The size of this neighbourhood has to be larger if the critical temperature is higher, because then the broken minimum moves more in field space under thermal effects. Therefore, we revise our original hypothesis in Section 2.2:

The smaller the value of $|\Delta V_{1\text{ loop }(0\text{T})}|$, the lower the critical temperature. Further, the strength of the phase transition ξ will become arbitrarily strong so long as the Higgs squared mass matrix remains positive in the neighbourhood of the broken vacuum.

We must stress again that in the current work we choose to use the one loop approximation to the effective potential. In some models the tree level approximation will be sufficient to indicate a first order phase transition, while in other models higher loop orders will have non-negligible impact and need to be included.

Let us consider the case where the $\mathbb{Z}_2$ symmetry is unbroken at zero temperature. Parameter points that undergo spontaneous $\mathbb{Z}_2$ breaking between zero temperature and the critical temperature are those observed either between the two branches in Figure 2.2 or lie on the same branch as the parameter points in the $\mathbb{Z}_2$ broken at zero temperature case. The points on the "universal" branch remain unbroken up to the critical temperature. What we call sliding behaviour therefore carries the notion of a parameter point *falling off the universal branch and, perhaps, onto the lower branch below.*

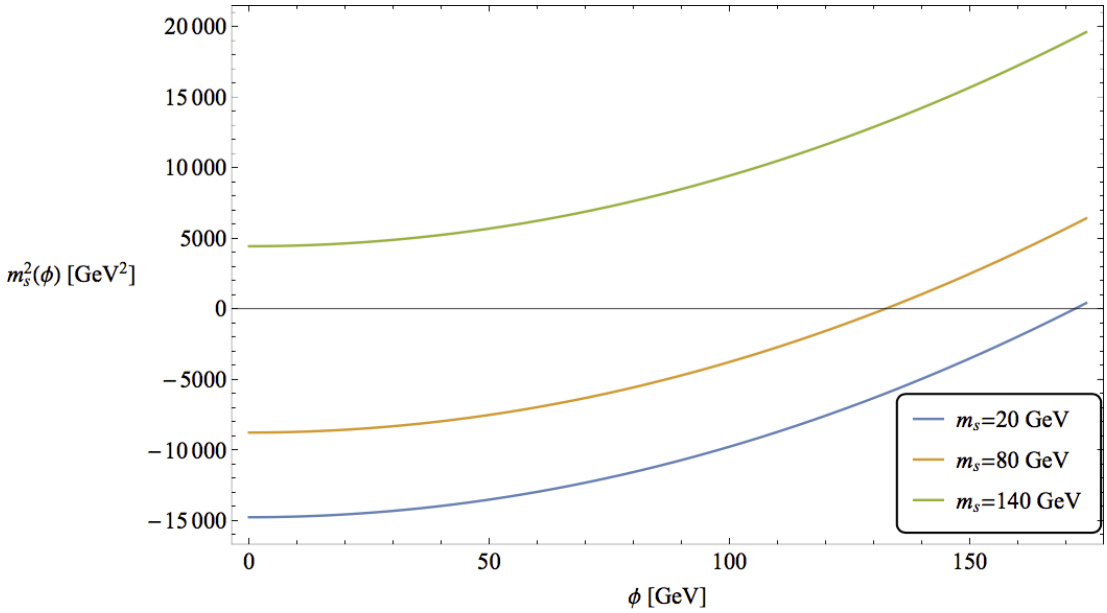

(a) Fixed coupling, $a_2 = 1.0$.

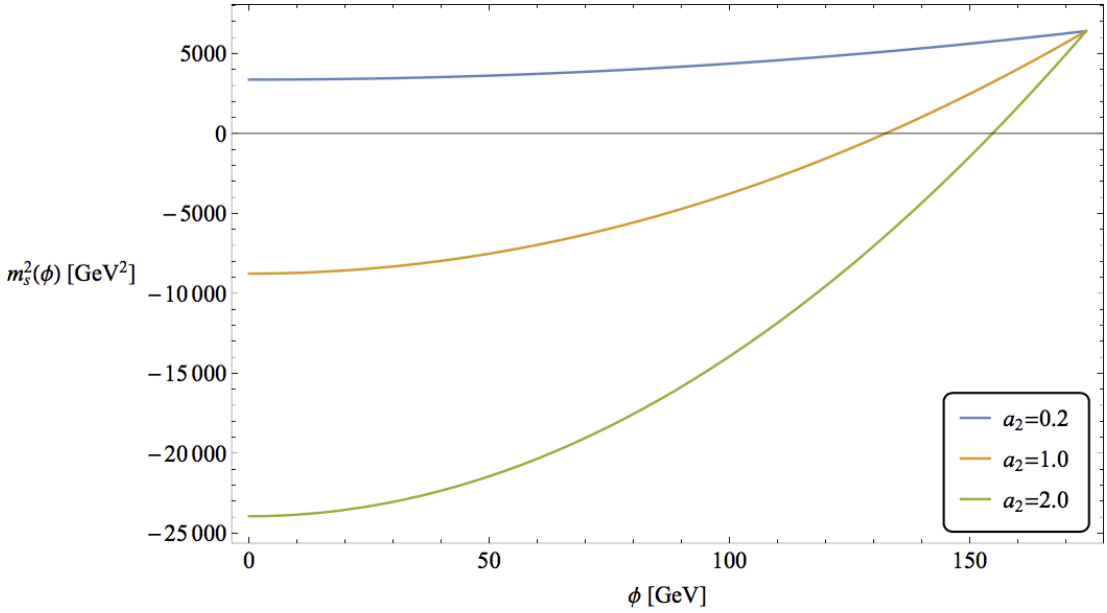

(b) Fixed singlet mass, $m_s = 80$ GeV.

Figure 2.3: Plot of the field-dependent singlet mass at $S = 0$ against the ϕ direction for various values of m_s and a_2 in the $\mathbb{Z}_2$xSM (unbroken). The $\mathbb{Z}_2$ symmetry spontaneously breaks at the value of ϕ where the singlet mass squared changes sign. The value of m_s controls the offset of the singlet mass away from $m_s(\phi) = 0$. For a given value of a_2, a lighter singlet mass brings the $\mathbb{Z}_2$ breaking critical field value closer to the zero temperature VEV, v. For a given value of m_s, the higher the value of the quartic coupling a_2, the closer the $\mathbb{Z}_2$ breaking critical field value is to the zero temperature VEV, v.

For the case where the $\mathbb{Z}_2$ symmetry is unbroken at zero temperature, the field-dependent singlet mass at $S = 0$ is given by

$$m_s^2(\phi) = m_s^2 + \frac{a_2}{2}(\phi^2 - v^2), \tag{2.62}$$

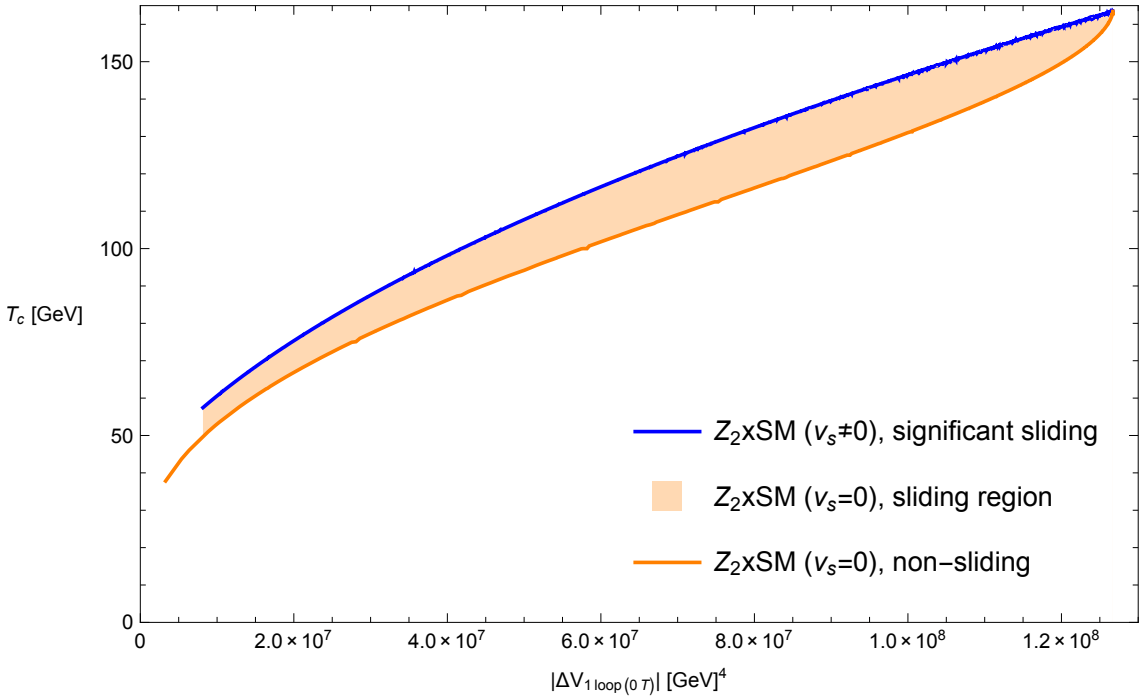

Figure 2.4: Critical temperature of the phase transition, T_c, against the magnitude of the vacuum energy difference, $|\Delta V_{1\text{ loop }(0\mathrm{T})}|$, for the $\mathbb{Z}_2$xSM. This plot outlines the full parameter region using the same parameter points that appear in Figure 2.2. The colour coding is also the same but we use a different shade of orange to show where the non-sliding and sliding parameter points exist.

where m_s is the mass of the singlet at $\phi = v$. Figure 2.3 shows how the critical Higgs field value (where the $\mathbb{Z}_2$ symmetry breaks) depends on the zero temperature quantities m_s and a_2. To avoid the $\mathbb{Z}_2$ symmetry breaking due to thermal effects, we must ensure that the mass-squared value of the singlet remains positive in the broken minimum up to the critical temperature. One may thus always guarantee a strong phase transition using our hypothesis by choosing m_s and a_2 such that eq. (2.62) is positive. A sliding singlet occurs for a light singlet mass and large a_2 coupling. In these cases, the small singlet mass results from a more or less severe tuning between bare and electroweak symmetry breaking induced terms.

As a result of sliding behaviour, taking $\Delta V_{1\text{ loop }(0\mathrm{T})} \to 0$ does not always guarantee a strong phase transition. However, we observe that $\Delta V_{1\text{ loop }(0\mathrm{T})} \to 0$ does generally lead a decrease of the critical temperature. This can be seen in Figure 2.4, which uses the same parameter points and similar colour coding to Figure 2.2. Rather than showing the parameter points, we have interpolated between them and outlined the parameter region instead. This is because, for all of the models investigated in this work, their parameter points appear somewhere between the non-sliding and significant sliding boundaries. Therefore, we cannot guarantee a strong phase transition as $\Delta V_{1\text{ loop }(0\mathrm{T})} \to 0$ because the Higgs VEV v_c tends to change drastically upon sliding.

It should be noted that phenomenological constraints only apply at zero temperature. Therefore all parameter points in the $\mathbb{Z}_2$ unbroken case are viable candidates for a theory beyond the SM, since there is no Higgs-singlet mixing at zero temperature. However, a spontaneous breaking of the $\mathbb{Z}_2$ symmetry before the start of the electroweak phase transition disfavours a strong phase transition. A more striking observation is that if the $\mathbb{Z}_2$ is spontaneously broken at zero temperature, none of the parameter points have a strong phase transition. This may be slightly modified by thermal effects, e.g. an enhancement of the thermally-induced barrier when the Higgs and singlet are included. Let us also note that in the case of spontaneous $\mathbb{Z}_2$ breaking, phenomenological constraints remove most of our parameter points. So spontaneous $\mathbb{Z}_2$ breaking before the critical temperature is phenomenologically disfavoured and, if realised, does not lead to a strong phase transition through $T = 0$ effects. This observation is consistent with the findings in ref. [48, 50, 51].

Let us now turn to the xSM with the $\mathbb{Z}_2$ explicitly broken at zero temperature. The parameter points for this model can be found in Figure 2.5. In comparison with the $\mathbb{Z}_2$xSM cases in Figure 2.2, we observe identical behaviour including the universal behaviour at low $|\Delta V_{1\text{ loop }(0\text{T})}|$. As for the physics, the main qualitative difference between the xSM and $\mathbb{Z}_2$xSM is that the $\mathbb{Z}_2$ is explicitly broken rather than *possibly* spontaneously broken. An interesting contrast between the xSM and $\mathbb{Z}_2$xSM ($v_S \neq 0$) case is that a lot of parameter points in the xSM do follow our hypothesis. This suggests that for a very strong phase transition and a non-zero Higgs-singlet mixing at zero temperature, the potential must contain non-thermal cubic terms for our hypothesis to succeed. In support of this statement, we find that all parameter points on the undesirable branch (traced by $\mathbb{Z}_2$xSM ($v_S \neq 0$) in Figure 2.2) vanish if we demand a large cubic term, $a_1 > 250$ GeV. We also observe that phenomenological constraints remove the majority of parameter points. Those surviving strictly follow our hypothesis that a tuning of the vacuum energy difference leads to a strong phase transition. After imposing phenomenological constraints, a strong phase transition is guaranteed if $|\Delta V_{1\text{ loop }(0\text{T})}| < 1.03 \times 10^8$ GeV^4, i.e. again a 25% tuning in the vacuum energy is sufficient.

These results are consistent with the findings of ref. [50]. The only exception is that we have not found any parameter points with a strong phase transition in the one loop $\mathbb{Z}_2$xSM ($v_S \neq 0$) model. This very feature was noted in [50] as being contradictory to other literature, such as [82]. We have identified that the $\mathbb{Z}_2$xSM with $\langle S \rangle = 0$ and $\langle S \rangle \neq 0$ in the broken vacuum at critical temperature lead to very different behaviour as $\Delta V_{1\text{ loop }(0\text{T})} \to 0$. This is understood in ref. [50] and here by the fact that we can only

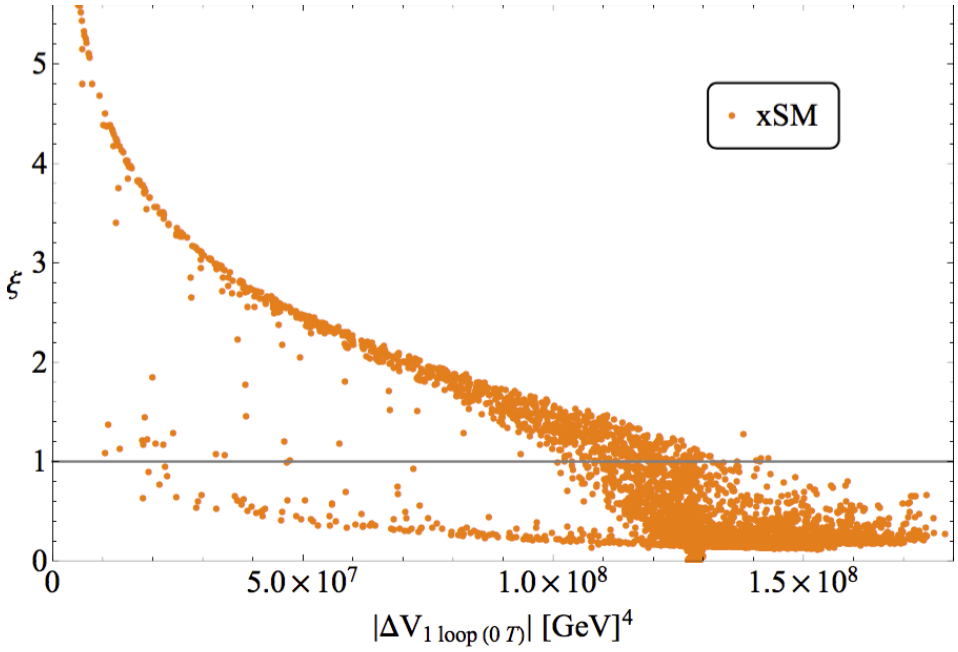

(a) Without phenomenological constraints.

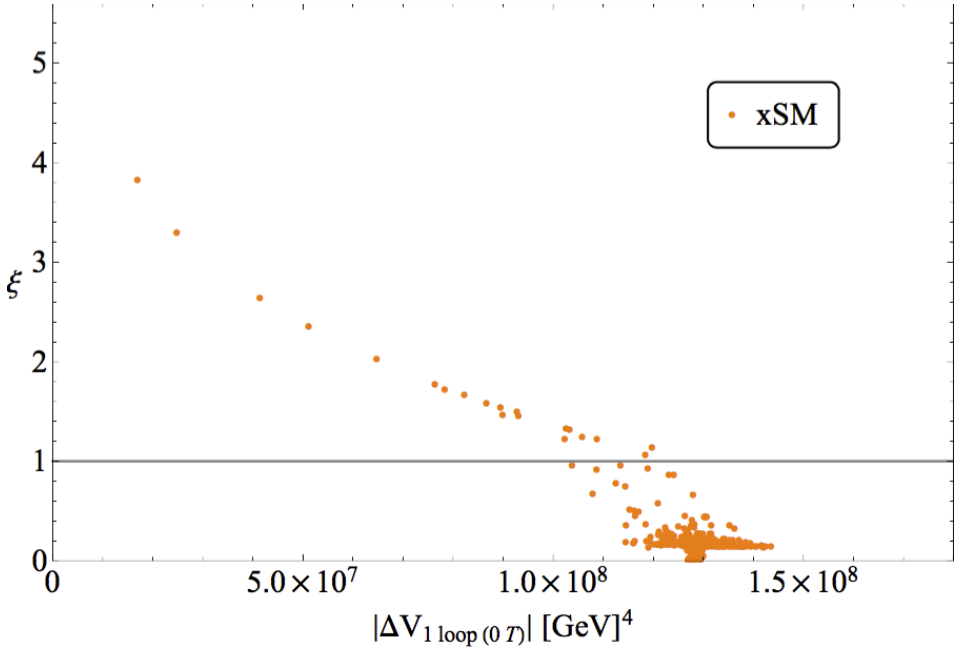

(b) With phenomenological constraints.

Figure 2.5: Distribution of the strength of the phase transition, ξ, against the magnitude of the vacuum energy difference, $|\Delta V_{1\text{ loop }(0\text{T})}|$, for the xSM with the $\mathbb{Z}_2$ explicitly broken at zero temperature. Also shown is the ξ=1 line.

retain a tree level barrier at critical temperature if $\langle S \rangle = 0$ in the broken vacuum. In the unbroken case, a very strong phase transition is much more natural to realise.

GNMSSM

Let us now turn to the GNMSSM. Comparing Figures 2.5 and 2.6 there is little difference between the GNMSSM and the non-supersymmetric singlet extended cases. However, we

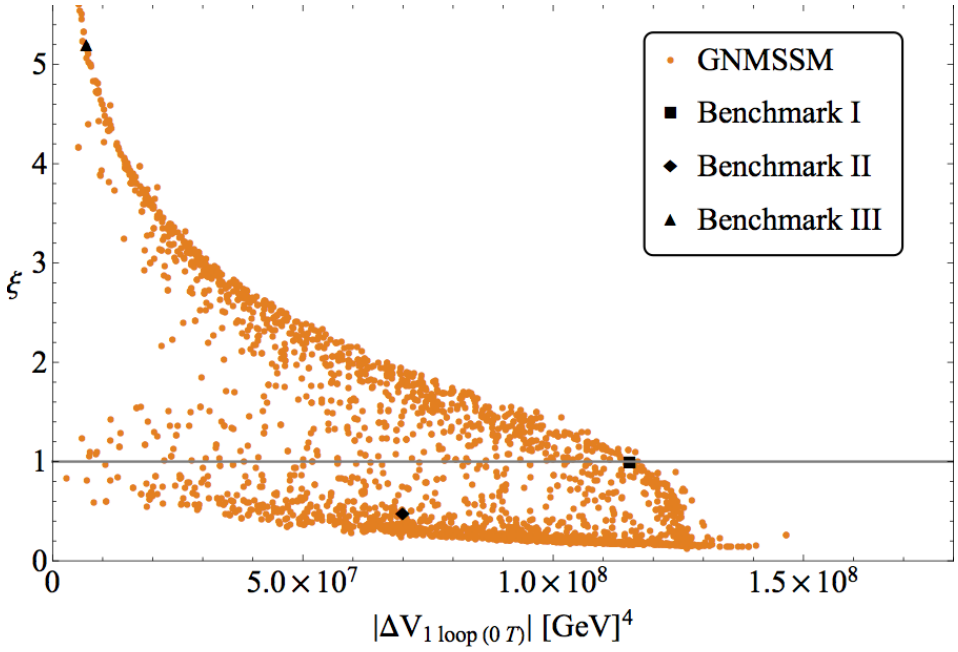

(a) Without phenomenological constraints.

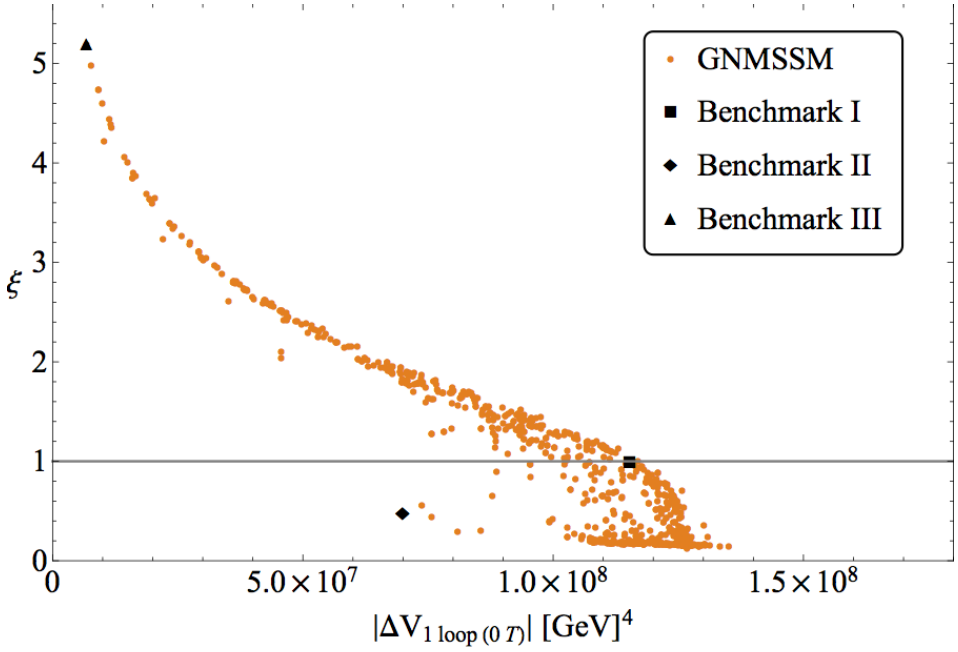

(b) With phenomenological constraints.

Figure 2.6: Distribution of the strength of the phase transition, ξ, against the magnitude of the vacuum energy difference, $|\Delta V_{1\text{ loop }(0\text{T})}|$, for the GNMSSM. The three benchmark models, chosen from the GNMSSM data set and discussed in Section 2.3.4, are marked above. Also shown is the ξ=1 line.

notice that the GNMSSM parameter points are more dispersed between the two branches. We suspect that this is because our scanning procedure happens to capture some of the more finely-tuned parameter regions of the supersymmetric theory. This is apparent when

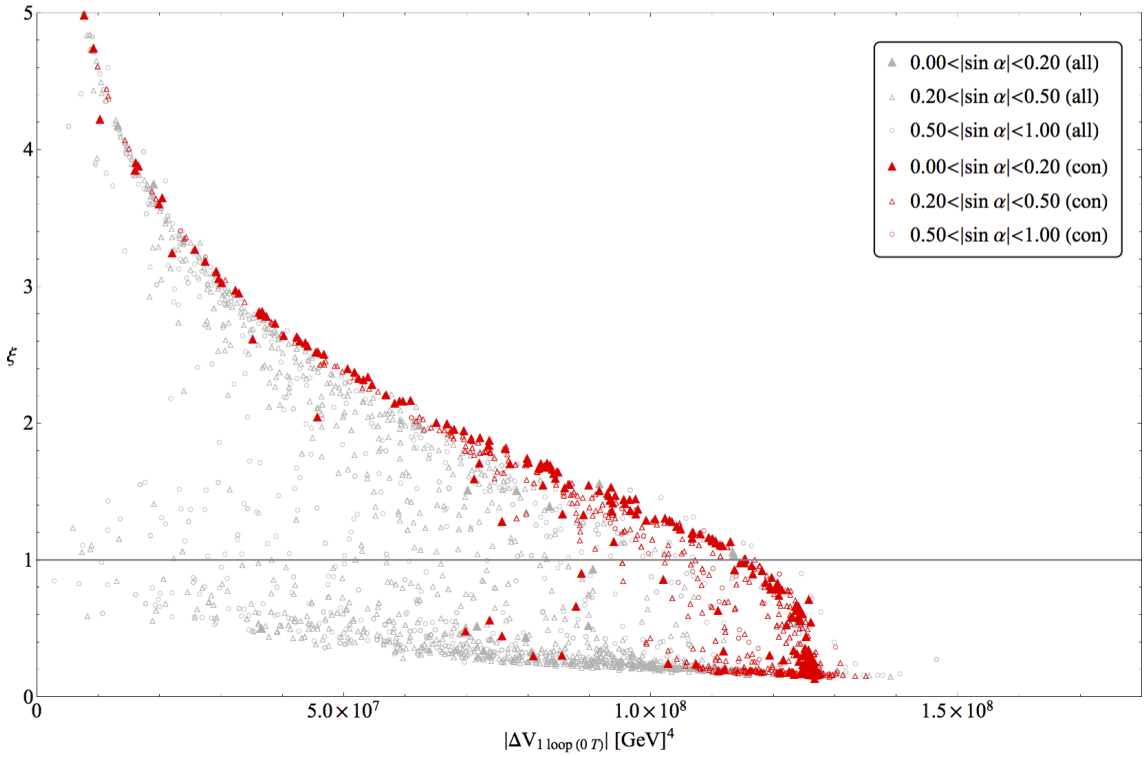

Figure 2.7: Distribution of the strength of the phase transition, ξ, against the magnitude of the vacuum energy difference, $|\Delta V_{1\text{ loop }(0\mathrm{T})}|$, for the GNMSSM with the mixing shown. Note in the key: (all) denotes all of the parameter points and (con) denotes the parameter points that satisfy phenomenology constraints.

we look at the tree level expression for the singlet mass at $S = 0$,

$$m_s^2(\phi) = m_s^2 + \lambda(\lambda - k_3 \sin 2\beta)(\phi^2 - v^2), \tag{2.63}$$

which is the GNMSSM analog of eq. (2.62). Unlike in the xSM where we perform a scan over potentially large values of the a_2 coupling through eq. (2.39), we are forced in the GNMSSM to keep the λ value small to avoid running into a Landau pole [77]. These couplings are crucial since they control the second derivative of the singlet field-dependent mass at $S = 0$, and hence the chance of finding a parameter point where the potential is destabilised in the singlet direction. An example of such a situation is benchmark II, with related Figure 2.10, discussed in Section 2.3.4. Like in the general xSM many parameter points are excluded by phenomenological constraints, in particular, because of too large a Higgs-singlet mixing. For the remaining points, there is a clear relationship between the vacuum energy difference and the strength of the phase transition ξ. Our estimates for the strength of the phase transition, eq. (2.59), and critical temperature, eq. (2.60), still apply.

Interestingly, we observe a tendency for points with small mixing, $|\sin\alpha| < 0.2$, to lead

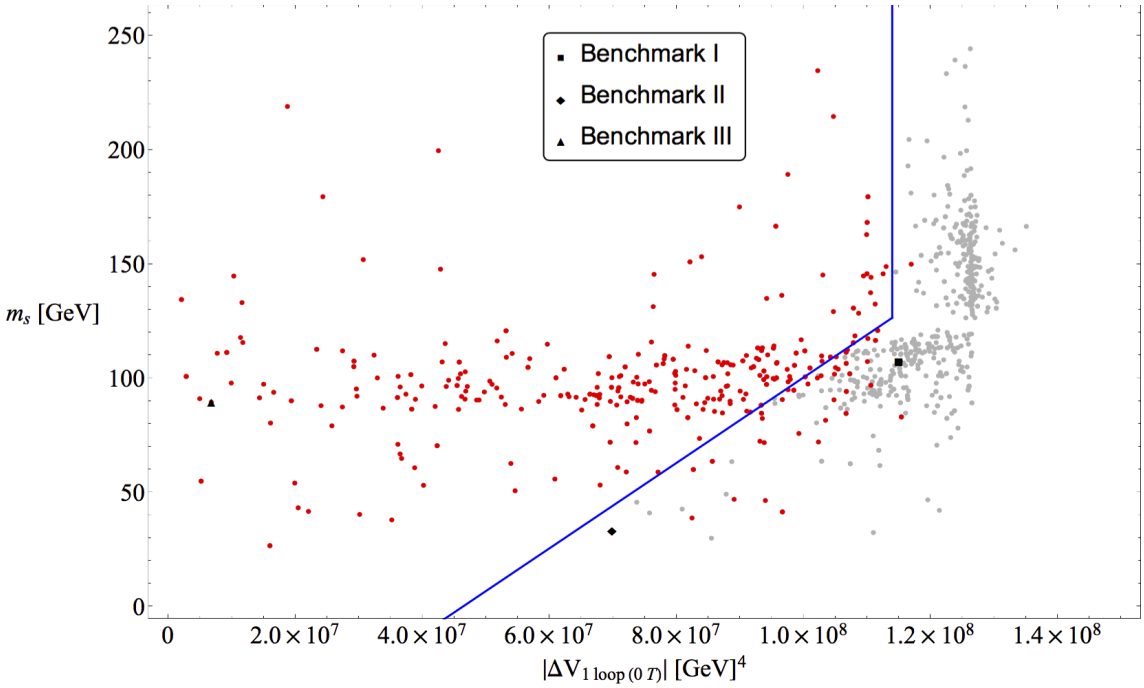

Figure 2.8: Plot of the singlet mass, m_s, against the vacuum energy difference, $|\Delta V_{1\text{ loop }(0\mathrm{T})}|$, for the GNMSSM data set with phenomenological constraints applied. Parameter points highlighted in red have a strong phase transition ($\xi > 1$), all other points do not ($\xi < 1$). The blue line indicates the bound suggested in eq. (2.64).

to a strong ξ-$|\Delta V_{1\text{ loop }(0\mathrm{T})}|$ correlation, as can be seen from Figure 2.7. Similar findings are reported in ref. [42] which covers the NMSSM in the limit of no mixing, i.e. $|\sin\alpha| \to 0$.

For the data set with phenomenological constraints applied we can see an upper bound of $|\Delta V_{1\text{ loop }(0\mathrm{T})}| < 6.98 \times 10^7$ GeV^4 ensures we have a strong phase transition. However, this bound removes a significant portion of our parameter space with a strong phase transition. In order to capture more parameter points with a strong phase transition, we instead impose the simultaneous constraints

$$\begin{gathered} m_s > (87.1\text{ GeV}) \times \left(\frac{|\Delta V_{1\text{ loop }(0\mathrm{T})}|}{4.65 \times 10^7\text{ GeV}^4} - 1 \right) \\ \text{and } |\Delta V_{1\text{ loop }(0\mathrm{T})}| < 1.14 \times 10^8\text{ GeV}^4. \end{gathered} \tag{2.64}$$

This bound is indicated in Figure 2.8, where it is clear that a significant number of points with a strong phase transition are captured. It should be stressed that the recipe in eq. (2.64) is only applicable to the GNMSSM with phenomenological constraints applied. Without phenomenological constraints applied a significant number of points with a weak phase transition (many small singlet masses with large Higgs-singlet mixing) appear in the parameter space covered by eq. (2.64). For the raw data set, we suggest a modified

bound of

$$m_s > (116\text{ GeV}) \times \left(\frac{|\Delta V_{1\text{ loop }(0\text{T})}|}{1.14\times 10^8\text{ GeV}^4}\right)^{1/2} \quad \text{and } |\Delta V_{1\text{ loop }(0\text{T})}| < 1.14\times 10^8\text{ GeV}^4. \tag{2.65}$$

A similar bound may be found for the non-supersymmetric models. Note how benchmark III comfortably sits within this territory whereas both benchmarks I and II would be excluded by eq. (2.64).

In summary, we find that after applying phenomenological constraints a strong first order phase transition in the GNMSSM requires (modest) tuning of the vacuum energy difference by around roughly 30%, i.e. from -1.3×10^8 GeV^4 to -0.9×10^8 GeV^4. This is not a significant amount of tuning. So a strong first order phase transition is easily realisable in the context of this model.

2.3.4 GNMSSM benchmark models

Here we will look at three benchmarks in our GNMSSM data set that satisfy phenomenological constraints. We have chosen the benchmarks based on the strength of the phase transition ξ and the value of the vacuum energy difference. All three are indicated in Figures 2.6 and 2.8. More specifically, we choose benchmark I (benchmark III) to have a strong phase transition but large (small) value of $|\Delta V_{1\text{ loop }(0\text{T})}|$ and benchmark II to have a weak phase transition but relatively tuned vacuum energy difference. For each benchmark we give the main parameter values (see Table 2.2) and the Higgs mass spectrum (see Table 2.3). The full set of defining parameters is given in Appendix C.

For each benchmark, contour plots of the potential at zero temperature and critical temperature are given in Figures 2.9-2.11. The potential displayed in the contour plots is offset and normalised according to

$$\tilde{V}(\phi, S; T) = \frac{V_{1\text{ loop}}(\phi, S; T) - V_{1\text{ loop }(0\text{T})}(v, v_S)}{V_{1\text{ loop }(0\text{T})}(0,0) - V_{1\text{ loop }(0\text{T})}(v, v_S)}. \tag{2.66}$$

Thus the potential in the broken vacuum at zero temperature corresponds to zero in the

Benchmark	λ	λA_λ	k_3	v_S	$\tilde{v}_S$	$m_{\tilde{t}_2}$	$\Delta V_{1\text{ loop }(0\text{T})}$	T_c	ξ
I	0.577	641.1	-0.151	-110.1	-234.6	613.1	-1.15×10^8	142.5	1.01
II	0.569	130.4	0.280	-161.5	0.0	844.1	-6.99×10^7	116.0	0.49
III	0.626	265.2	-0.251	-146.7	-348.3	907.7	-6.79×10^6	47.1	5.20

Table 2.2: Some of the more important quantities for each benchmark scenarios. The full set of parameter values are provided in Appendix C. All masses are in units of GeV.

Benchmark	$\lvert\sin\alpha\rvert$	m_h	m_H	m_s	m_A	m_{A_s}	$m_{H^\pm}$
I	0.119	125.0	853.7	107.2	779.1	945.0	839.1
II	0.013	125.0	888.0	33.0	887.1	833.3	883.5
III	0.172	125.0	2586.8	89.3	2586.5	1212.0	2585.0

Table 2.3: One loop zero temperature Higgs mass spectrum in the benchmark scenarios. All masses are in units of GeV.

displayed potential, $\tilde{V}(v, v_S; 0) = 0$, and the origin in field space corresponds to unity, $\tilde{V}(0, 0; 0) = 1$. The broken (symmetric) extremum is marked on each potential as a red cross (plus).

The key observation is to see how much the broken vacuum has moved away from its zero temperature value at the critical temperature. Specifically, the singlet value in the broken vacuum does not change by much in benchmarks with a strong phase transition, whereas the singlet value of the broken vacuum changes significantly in benchmark II. To quantify the change of any field value in the broken vacuum, we define the fractional change to be

$$\delta(\Phi) = \frac{|\Phi_{\text{broken}}(T = 0) - \Phi_{\text{broken}}(T = T_c)|}{v}, \tag{2.67}$$

where Φ is to be recognised with one of our fields. A low fraction corresponds to the VEV at critical temperature remaining close to its zero temperature value, whereas a high fraction corresponds to the VEV at critical temperature being far from its zero temperature value. In Table 2.4 we display the values for each benchmark. This allows us to qualitatively link our hypothesis to each of the benchmarks. Namely, that the broken minimum should remain in a neighbourhood of its zero temperature value if we want a strong phase transition.

All of our benchmarks have small Higgs-singlet mixing in accordance with experimental constraints. The singlet state is always lighter than the SM-like Higgs and for benchmark II it is significantly lighter. For all benchmarks the Higgs-singlet coupling λ is close to the upper bound that prevents running into a Landau pole [77]. All other Higgs states are

Benchmark	$\delta(\phi)$	$\delta(S)$	Behaviour
I	0.42	0.030	Minimally strong phase transition, minimal tuning of $\lvert\Delta V_{1\text{ loop }(0\text{T})}\rvert$
II	0.77	0.90	Weak phase transition, irrespective of the tuning of $\lvert\Delta V_{1\text{ loop }(0\text{T})}\rvert$
III	6.0×10^{-5}	1.1×10^{-3}	Very strong phase transition, significant tuning of $\lvert\Delta V_{1\text{ loop }(0\text{T})}\rvert$

Table 2.4: Fractional change of the ϕ and S fields using eq. (2.67) and the behaviour of each benchmark.

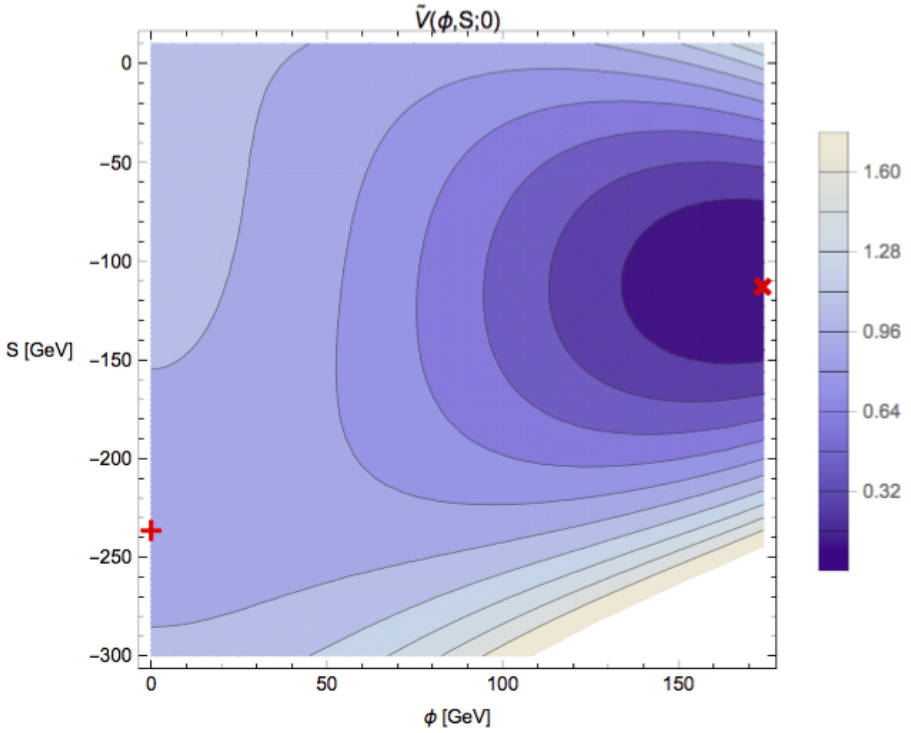

(a) Potential at zero temperature.

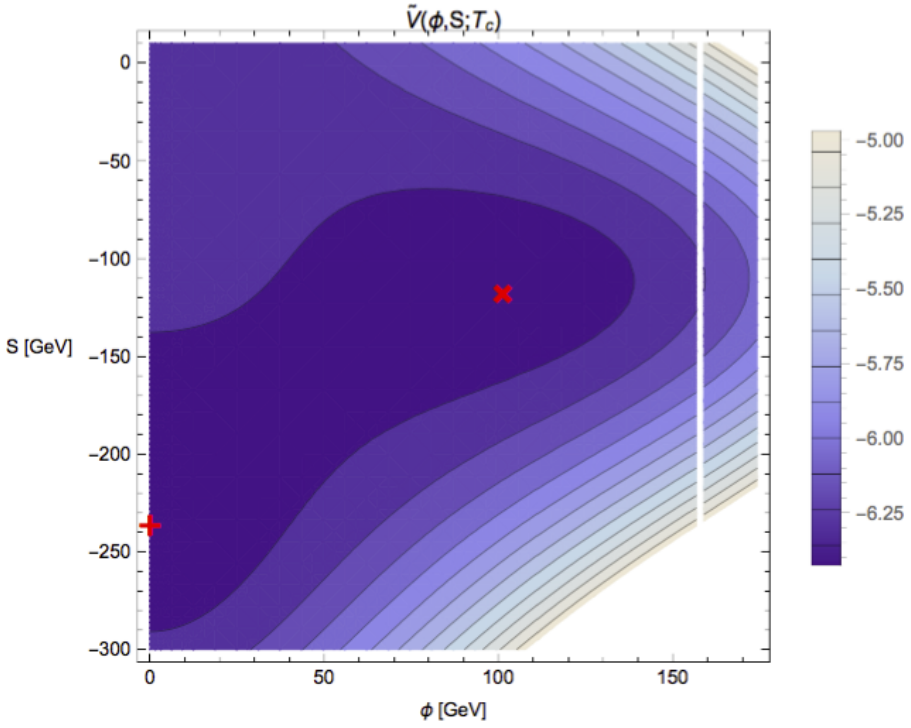

(b) Potential at critical temperature.

Figure 2.9: The above plots show the shape of the one loop effective potential in (ϕ, S) field space at (a) zero temperature and (b) critical temperature for benchmark I. The broken (symmetric) vacuum is marked by a red cross (plus). At zero temperature, the broken and symmetric vacua are located at (174.2, −110.1) and (0,−234.6), respectively. At the critical temperature, $T_c = 142.5$ GeV, the broken and symmetric vacua are located at (101.5, −115.4) and (0,−234.6), respectively. All fields are in units of GeV. The potential displayed is defined in eq. (2.66).

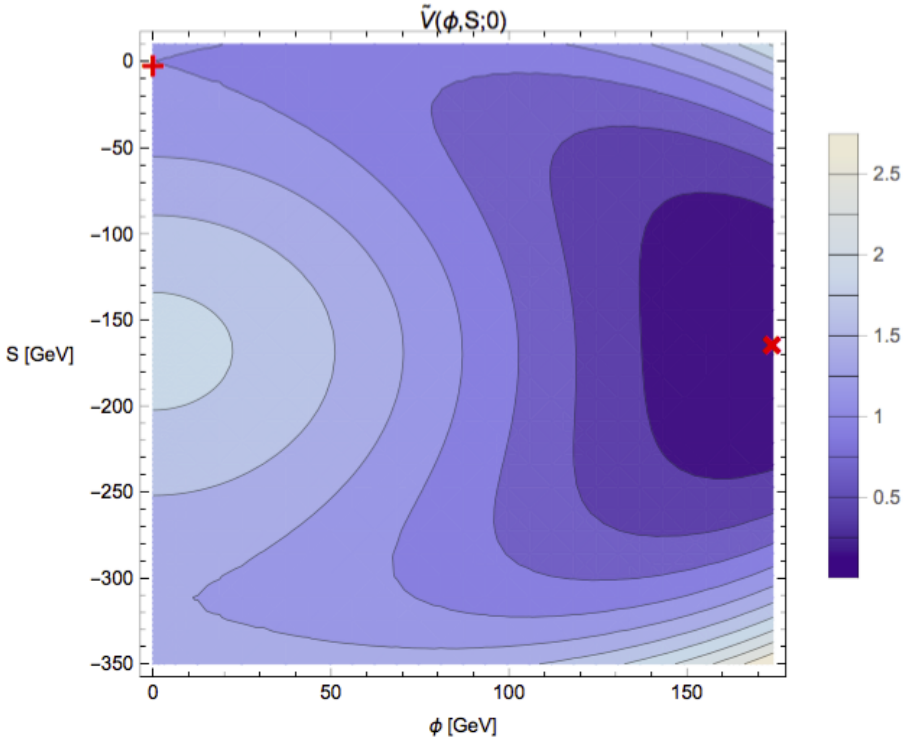

(a) Potential at zero temperature.

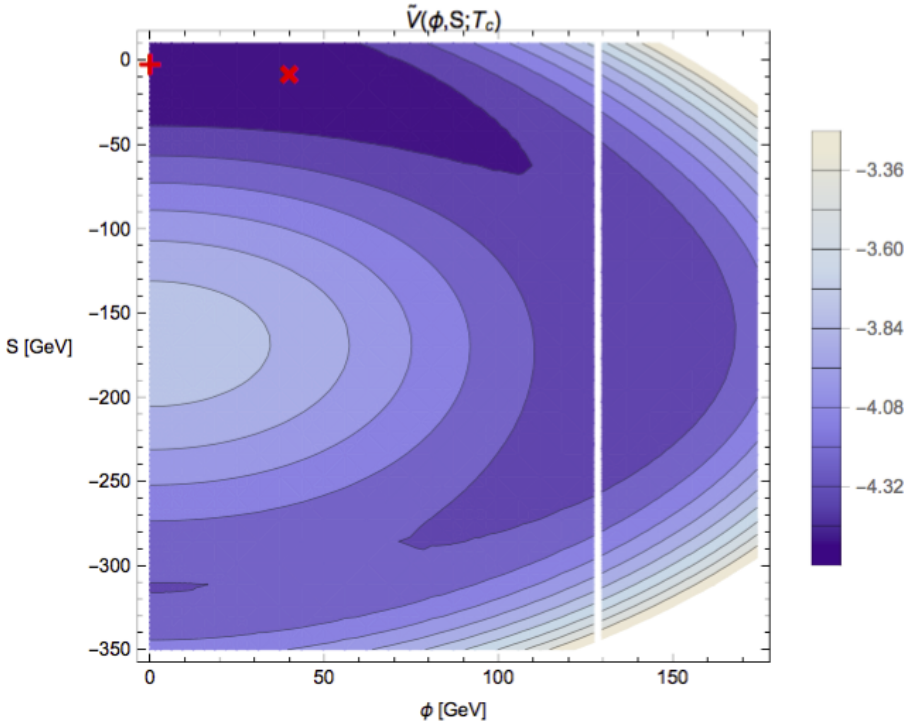

(b) Potential at critical temperature.

Figure 2.10: The above plots show the shape of the one loop effective potential in (ϕ, S) field space at (a) zero temperature and (b) critical temperature for benchmark II. The broken (symmetric) vacuum is marked by a red cross (plus). At zero temperature, the broken and symmetric vacua are located at (174.2, −161.5) and (0,0), respectively. At the critical temperature, $T_c = 116.0$ GeV, the broken and symmetric vacua are located at (40.0, −5.19) and (0,0), respectively. All fields are in units of GeV. The potential displayed is defined in eq. (2.66).

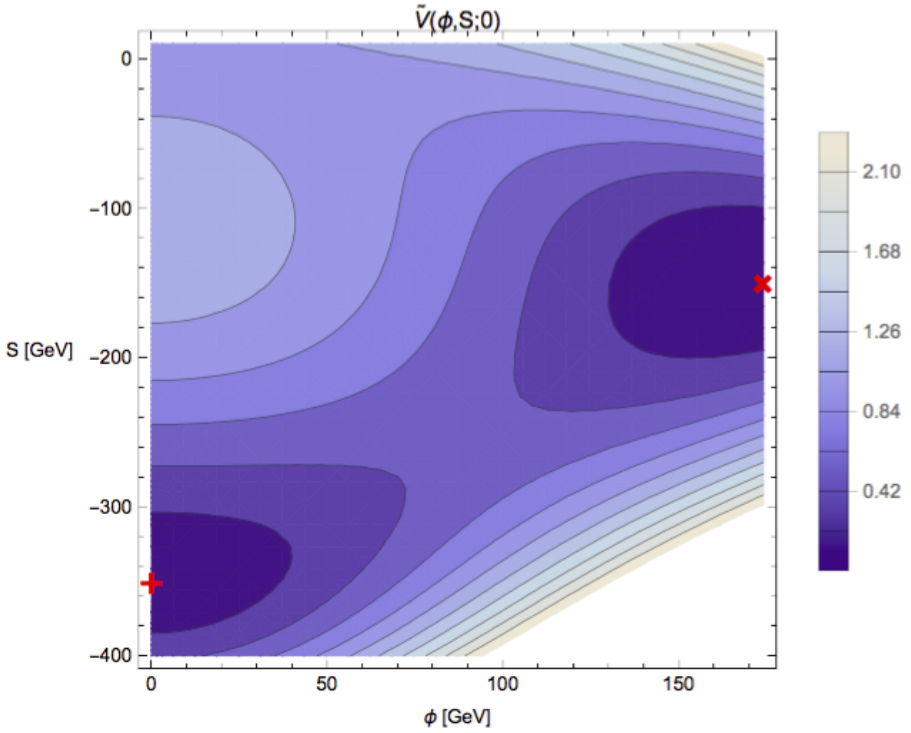

(a) Potential at zero temperature.

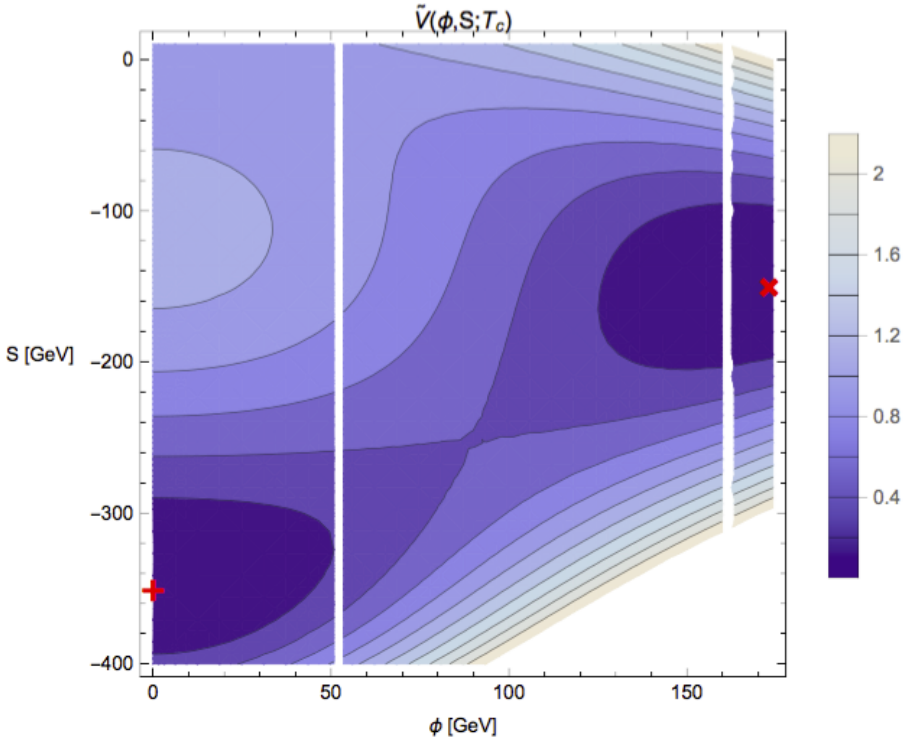

(b) Potential at critical temperature.

Figure 2.11: The above plots show the shape of the one loop effective potential in (ϕ, S) field space at (a) zero temperature and (b) critical temperature for benchmark III. The broken (symmetric) vacuum is marked by a red cross (plus). At zero temperature, the broken and symmetric vacua are located at (174.2, −146.7) and (0,−348.3), respectively. At the critical temperature, $T_c = 47.1$ GeV, the broken and symmetric vacua are located at (173.2, −146.9) and (0,−348.3), respectively. All fields are in units of GeV. The potential displayed is defined in eq. (2.66).

heavy and decouple from the phase transition.

Benchmark I has a very moderate tuning of $|\Delta V_{1\text{ loop }(0\text{T})}|$ and does not suffer from a sliding singlet instability, so we arrive at a phase transition with $\xi = 1.01$. This is just strong enough to avoid baryon number washout. In Figure 2.9, we see that the symmetric and broken extrema are well separated by a barrier which does not disappear as we approach the critical temperature, $T_c = 142.5$ GeV. We also note that the λA_λ cubic term is largest for this benchmark. Since the critical temperature is relatively high, the critical Higgs field v_c is noticeably different from its zero temperature value v. However, we notice that the singlet VEV hardly moves during the phase transition.

In benchmark III we significantly tune the vacuum energy difference to a small value, whilst keeping the singlet relatively heavy. This results in a very strong first order phase transition with $\xi = 5.20$ and a much reduced critical temperature of $T_c = 47.1$ GeV. In Figure 2.11 we see a greatly enhanced barrier compared to Figure 2.9. Both VEVs hardly move in this case. We expect the symmetric vacuum to be metastable in this case so the phase transition may not actually take place. This could be checked by computing the energy of the critical bubble which, however, goes beyond the scope of this chapter. Starting from this benchmark and reducing the tuning of the vacuum energy difference, we would expect to retain a strong phase transition but enter a regime where the phase transition actually takes place.

Benchmark II is very much different to the already discussed benchmarks, as is apparent in Figure 2.10, which contains a valley connecting the symmetric and broken extrema. In this case the singlet is rather light and the λA_λ cubic term has the lowest value compared to the others benchmarks. As discussed in the non-supersymmetric case, as the temperature is increased the Higgs mass squared matrix develops a negative eigenvalue and the broken vacuum slides toward the symmetric extremum. This is indicated by the big change in the singlet field (see Table 2.4). As a result the critical temperature, $T_c = 116.0$ GeV, is not as low as the vacuum energy difference suggests. This can be understood by Figure 2.4.

Overall, these benchmarks indicate that a strong first order phase transition can be enforced by having a not too light singlet state with small mixing to the Higgs and a moderately tuned vacuum energy difference.

2.4 The Minimal Standard Model with variable Higgs mass

From the investigation thus far, we observe two distinct scenarios. One scenario we call *non-sliding*, whereby parameter points have $v_c \to v$ as $T_c \to 0$ monotonically by a tuning of $|\Delta V_{1\text{ loop }(0\text{T})}| \to 0$. Universal behaviour for low T_c explains the well-defined branch in the first scenario, see eq. (2.59)-(2.60). Parameter points in this scenario satisfy our initial hypothesis in Section 2.2.

The other scenario we call *sliding*, where parameter points have $v_c \ll v$ as T_c decreases by a tuning of $|\Delta V_{1\text{ loop }(0\text{T})}| \to 0$. Note in the sliding case that T_c decreases monotonically as $|\Delta V_{1\text{ loop }(0\text{T})}| \to 0$ but does not necessarily go to zero. This is discussed in the section below and can be seen in Figure 2.14. In this scenario, Figure 2.2 revealed that many of the $\mathbb{Z}_2$xSM ($v_S = 0$) parameter points fall on another well-defined branch. This branch is exactly traced out by the $\mathbb{Z}_2$xSM ($v_S \neq 0$) parameter points. These parameter points comfortably reside in the sliding region and are thus interpreted as having experienced *significant sliding* behaviour. For singlet extended models, parameter points that experience significant sliding characteristically have $\langle S \rangle_{\text{broken}} \approx \langle S \rangle_{\text{symm}}$ at critical temperature, where $\langle S \rangle_{\text{broken}}$ is far away from its value at zero temperature. This typically occurs for parameter points whose broken vacuum destabilises at a temperature significantly lower than critical temperature, i.e. shortly after zero temperature.

2.4.1 The significant sliding branch

In this section we would like to convince the reader that the well-defined, significant sliding branch has the same phase transition properties as the Minimal SM when the Higgs mass is treated as a free parameter, therefore implying that this branch originates from the Minimal SM-like features of the potential.

The tree level potential in the SM can be found in eq. (2.1). Recall that $\phi = \text{Re}(\text{H}^0)$ is recognised as the Higgs field. Here we will relax the condition that the Higgs mass is $m_h = 125$ GeV. Instead we choose the value of 0 GeV $< m_h \leq 125$ GeV. The Higgs mass is then the free parameter used to tune the tree level contribution of the vacuum energy difference $\Delta V_{\text{tree}}^{[\text{SM}]}$, see eq. (2.27). Such a one field scalar potential is no longer physically realisable since the discovery of the Higgs boson. However it is still very useful for investigating various extensions of the SM. As we previously mentioned, the same phase transition properties (v_c, T_c, and ξ) are found for models that experience significant sliding behaviour. This is a direct result of the phase transition being solely driven by the SM content in the radiative piece of the effective potential.

Firstly, we repeat the analysis conducted in Section 2.3 using the Higgs mass as a free parameter. We will only include the top quark and electroweak gauge bosons in loop corrections, unless otherwise stated. This ensures that our approach is consistent with that in the Section 2.3. The numerically determined branch is shown by the faded red curve in Figure 2.12. The resulting relations between v_c, T_c, and $\Delta V_{1\text{ loop }(0\text{T})}$ are exactly the same as those found for singlet extended models that experience significant sliding behaviour, e.g. the lower branches in Figures 2.2 and 2.5.

There is a slight deviation between the non-supersymmetric branch and the GNMSSM branch displayed in Figure 2.6. This is because the supersymmetric model includes stops in the one loop effective potential. This is necessary to attain a 125 GeV Higgs mass. Note that we also include the stops into thermal radiative corrections. Within a high temperature expansion of the thermal effective potential, deviations between the branches can be explained by the presence of additional thermally-induced cubic terms. If we instead consider the low temperature expansion of the thermal effective potential, the deviation can be explained by the additional number of degrees of freedom in the plasma. Although we should keep in mind that the stops in our data set tend to have heavy explicit masses (from the softly broken supersymmetry), and so we would expect them to decouple from

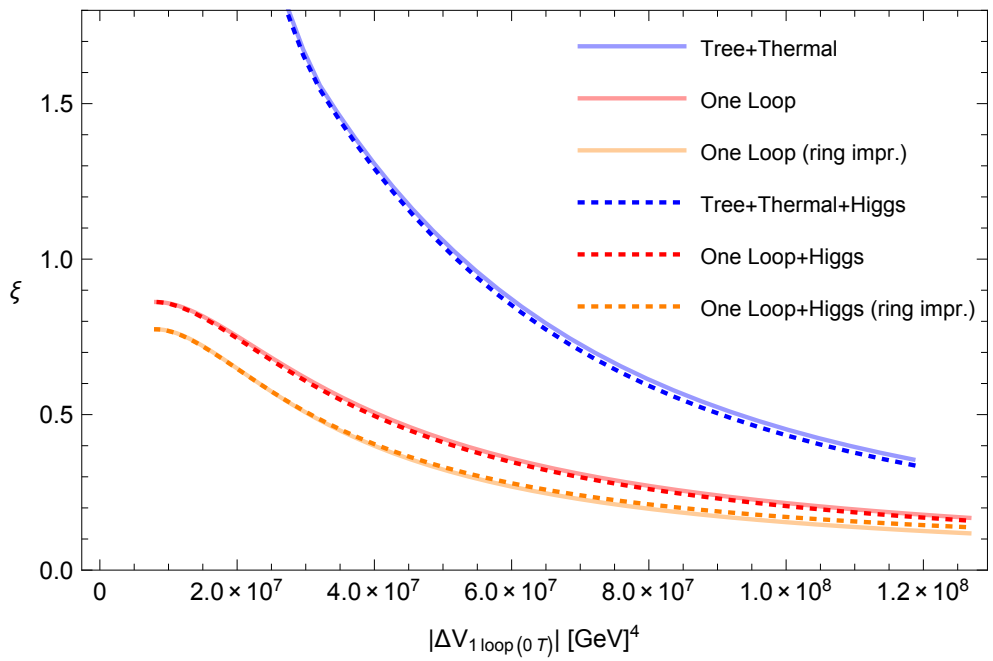

Figure 2.12: Plot of the strength of the phase transition at critical temperature ξ against the zero temperature vacuum energy difference $|\Delta V_{1\text{ loop }(0\text{T})}|$. We display the result with (dashed) and without (faded solid) the Higgs boson included as a $T = 0$ and thermal one loop correction. Similarly, the red and orange coloured curves represent the result for an effective potential with and without the inclusion of the ring term in eq. (2.70), respectively. We include set of blue curves that represent the result when the zero temperature one loop contributions are ignored.

the phase transition due to their terms being Boltzmann suppressed in the low temperature effective potential.

We have chosen to decrease $|\Delta V_{1\text{ loop }(0\text{T})}|$ by lowering the value of m_h, eq. (2.28). However, the smaller the value of m_h the more significant the radiative corrections' effect on the shape of the potential and the phase transition. Therefore we expect parameter points that lie on the lower branch and in the low $|\Delta V_{1\text{ loop }(0\text{T})}|$ region to be most sensitive to our treatment of the effective potential, e.g. higher loop order and resummation effects.

2.4.2 Dependence of results on the treatment of the effective potential

Here we will address some important questions regarding the treatment of the effective potential. We display the numerically determined branch for the potential treated in three unique setups in Figure 2.12. Each setup further excludes or includes the Higgs boson in zero temperature and thermal one loop corrections. We will describe each of the setups below in order of their significance on the shape of the strength ξ against $|\Delta V_{1\text{ loop }(0\text{T})}|$ curve. Note that each curve should be contrasted against the red faded curve in Figure 2.12, which is determined by the same setup as models in preceding sections of this chapter.

Tree + thermal only

The blue curve deviates the most from the red curve. The setup used to determine the blue curve ignores all zero temperature radiative corrections, but includes them in the thermal corrections. In other words there are no Coleman-Weinberg type terms in the scalar potential. We argue that this approach is risky; ignoring the zero temperature one loop contribution but taking only the thermal one loop contribution to the effective potential is a dangerous move.

Our reasoning as to why this approach is dangerous is the following. As the Higgs mass becomes smaller, radiative corrections to the potential have an increasingly significant effect on the properties and overall shape of the zero temperature potential. This can be seen from the fact that as $m_h \to 0$, the potential becomes not only locally flat in the broken vacuum but also globally flat. This is suggestive of the potential being sensitive to radiative corrections, with more sensitivity the closer we are to $|\Delta V_{1\text{ loop }(0\text{T})}| = 0$ in the Figure 2.12. For low $|\Delta V_{1\text{ loop }(0\text{T})}|$ the value of T_c is also low, so thermal terms in the effective potential are likely Boltzmann suppressed in the broken vacuum, see Section 2.3.3 for an explanation. Thermal effects therefore bring down the symmetric extremum toward

the broken vacuum in the zero temperature potential. The shape of the potential at critical temperature and hence the phase transition properties are likely determined by the shape of the potential at zero temperature. Therefore one ought to include one loop effects when m_h takes on small values.

This justifies our approach in the preceding work whereby we include at least the top quark and electroweak gauge bosons in the one loop correction. Hence the red curve in Figure 2.12 comes from a more reliable approach than the blue curve. It is nonetheless interesting that the "tree+thermal only" approach finds arbitrarily strong phase transitions, in accordance with the initial hypothesis in Section 2.2. The reason for this difference is explained below.

The importance of radiative effects

As the Higgs mass goes to zero, the critical temperature is lowered. This results in the tree level piece of the potential vanishing so that only the one loop piece of the potential remains. Therefore only the radiative piece of the potential can determine the strength of the phase transition at the lowest value of $|\Delta V_{1\text{ loop }(0\text{T})}|$. This effect can be seen in Figures 2.13 and 2.14.

Here we decrease the top quark mass in order to reduce the one loop contribution to the vacuum energy difference. Our results are consistent with FIG 3 in [69]. We do not change the electroweak gauge boson masses in order to keep the thermally-induced cubic terms the same. We also confirm that each result is independent of the renormalisation scale Q. This is achieved by setting Q as either (i) fixed to the observed top mass of 173.07 GeV or (ii) varying with the freely chosen top quark mass. It just so happens that for a top quark mass greater than $m_t \gtrsim 165$ GeV, a few GeV below the experimentally measured value, the strength of the phase transition does not exceed unity, i.e. $\xi \lesssim 1$.

Figure 2.14 is particularly insightful. For most curves, as the Higgs mass is taken toward zero the critical temperature does not go to zero but to a positive value. These curves have a top mass that corresponds to $\Delta V_{1\text{ loop }(0\text{T})} < \Delta V_{\text{tree}}$. Between the purple and black curves exists a curve which, as the Higgs mass goes to zero, goes to exactly $T_c \to 0$. This occurs for a top quark mass of

$$m_t = \left(\frac{g_W m_W^4 + g_Z m_Z^4}{g_t} \right)^{1/4} = 78.60 \text{ GeV}, \tag{2.68}$$

which coincides with the one loop zero temperature vacuum energy difference contribution in eq. (2.28) being exactly zero. A top quark mass lower than this value, corresponding to

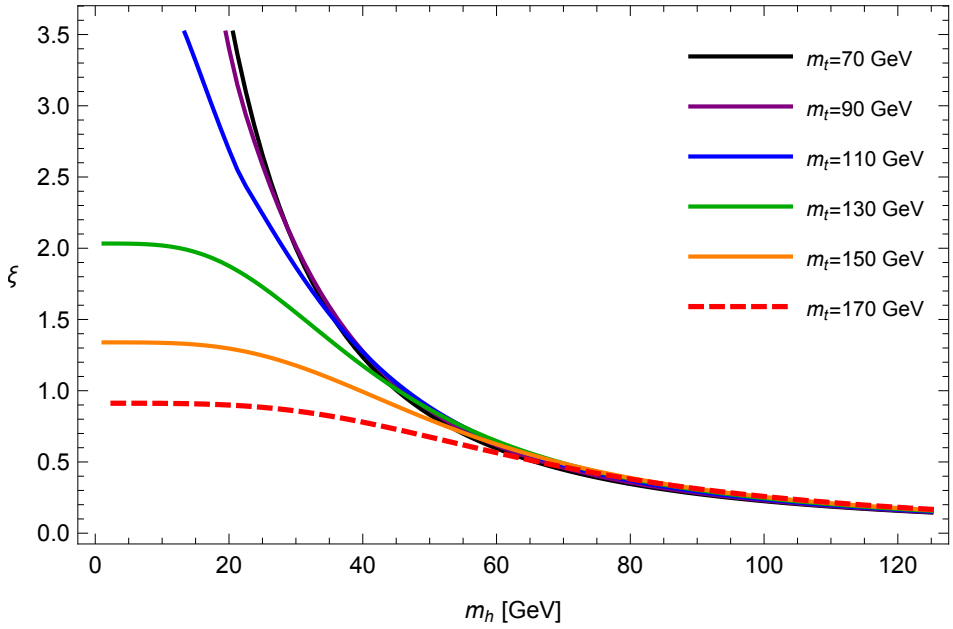

(a) The strength ξ at critical temperature against the Higgs mass m_h at zero temperature. This plot is directly comparable with FIG 3 in [69].

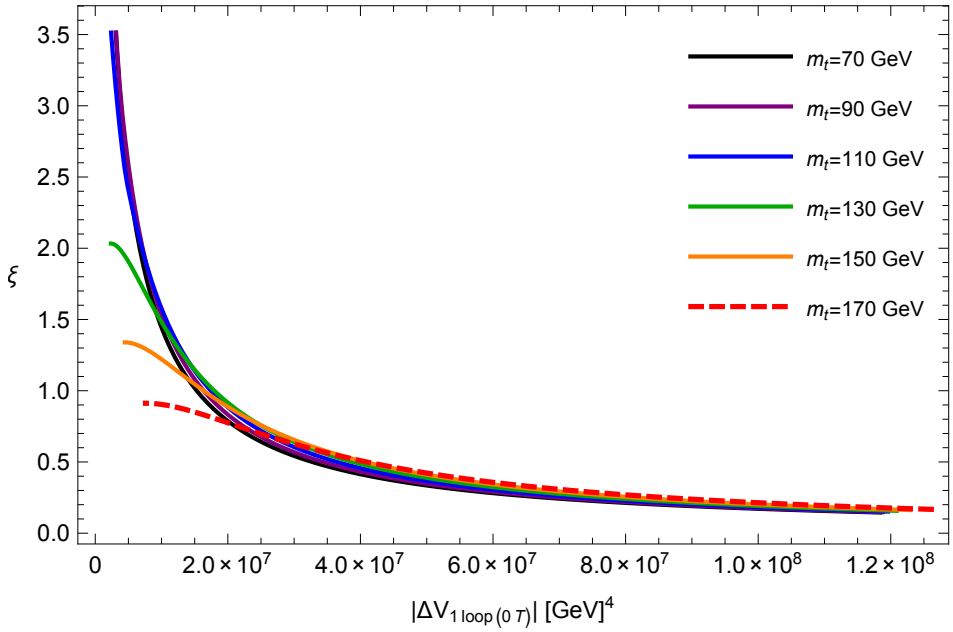

(b) The strength ξ at critical temperature against $|\Delta V_{1\ \mathrm{loop}\ (0\mathrm{T})}|$.

Figure 2.13: Plots to show how the Minimal SM branch changes with the top quark mass. The top quark mass is given by the legend. We use an effective potential with the top quark and electroweak gauge bosons and no Higgs boson in the radiative corrections. The original curve (the red faded curve in Figure 2.12) is roughly the same as the red dashed branch in the above figure.

$\Delta V_{1\ \mathrm{loop}\ (0\mathrm{T})} > \Delta V_{\mathrm{tree}}$, would have $T_c \to 0$ with $m_h > 0$ as $\Delta V_{1\ \mathrm{loop}\ (0\mathrm{T})} \to 0$. We suspect that $\Delta V_{1\ \mathrm{loop}\ (0\mathrm{T})} > \Delta V_{\mathrm{tree}}$ is a condition whereby one will guarantee an arbitrarily strong phase transition as $\Delta V_{1\ \mathrm{loop}\ (0\mathrm{T})} \to 0$. Otherwise, the heavy top quark mass and its large number of degrees of freedom will prevent $T_c \to 0$. Hence the initial hypothesis

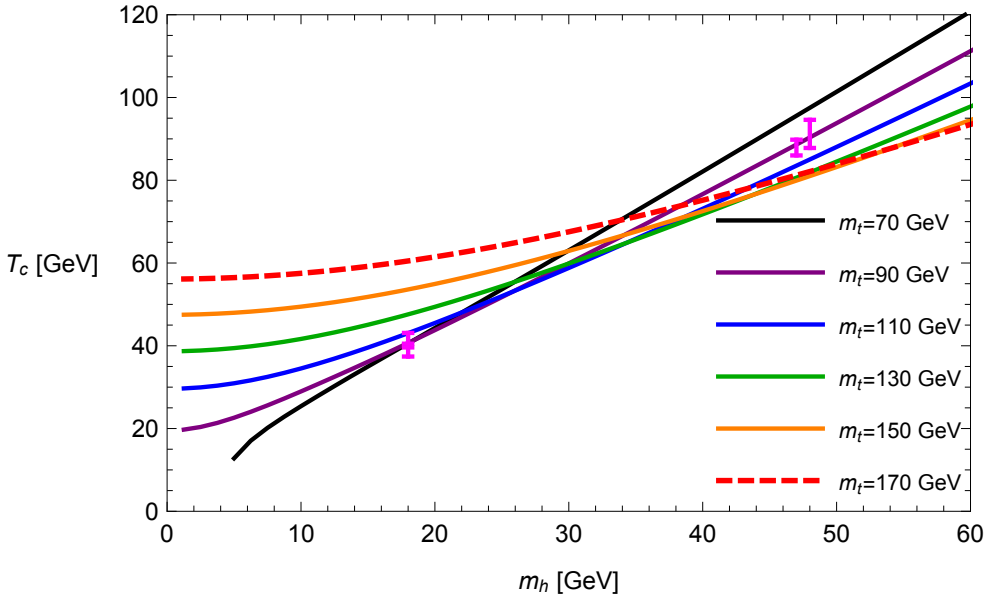

Figure 2.14: Plot of the critical temperature against the Higgs mass in the Minimal SM with variable Higgs mass. Each curve is found numerically for a chosen top quark mass. The top quark mass is given by the legend. We use an effective potential with the top quark and electroweak gauge bosons and no Higgs boson in the radiative corrections. For too high a top mass, we find $T_c > 0$ as $m_h \to 0$. Therefore we cannot get an arbitrarily strong phase transition in taking $\Delta V_{1\text{ loop }(0\text{T})} \to 0$. The magenta error bars display the lattice result from ref. [2].

in Section 2.2 fails. With SM particle content, the condition that $\Delta V_{1\text{ loop }(0\text{T})} > \Delta V_{\text{tree}}$ can only be realised by including sufficiently many or heavy bosons into $T = 0$ radiative corrections to counter the top quark's effect.

As an alternative to changing the top quark mass, we can add bosonic degrees of freedom to change the radiative piece, $\Delta V_{1\text{ loop }(0\text{T})} - \Delta V_{\text{tree}}$. This is more desirable for BSM studies. Let us assume the existence of a new boson coupled to the Higgs, with g_b degrees of freedom and a field-dependent mass of the form $m_b(\phi) = \frac{m_b}{v}\phi$. A further constraint is that the broken electroweak vacuum is the true vacuum at zero temperature, $0 > \Delta V_{1\text{ loop }(0\text{T})}$. Therefore, for $0 > \Delta V_{1\text{ loop }(0\text{T})} > \Delta V_{\text{tree}}$, the pole mass of the new boson must be

$$318.6\text{ GeV} < (g_b)^{1/4} m_b < 632.5\text{ GeV}. \tag{2.69}$$

An example of such a potential is the SM with an additional Coleman-Weinberg scalar, described in Section 2.1.1, and can be realised through a two Higgs doublet model [52, 83–86]. In fact, Figure 5.10(a) in ref. [84] shows that one can obtain an arbitrarily strong phase transition by taking the vacuum energy difference to $\Delta V_{1\text{ loop }(0\text{T})} \to 0$. They found $\Delta V_{1\text{ loop }(0\text{T})} \to 0$ occurs when $m_H \to 480$ GeV, where m_H is the heavy neutral Higgs boson. For our previous investigation, we took $g_b = 1$ and found $m_b > 430.2$ GeV for a strong phase transition $\xi \gtrsim 1$, see Table 2.1. This satisfies the range in eq. (2.69) in which

we expect the phase transition to be arbitrarily strong because $T_c \to 0$ as $\Delta V_{1\text{ loop (0T)}} \to 0$. This is consistent with the result in Figure 2.1. We also remark that either reducing the top mass or including an additional Higgs-coupled scalar(s) improves the vacuum stability of the potential.

A recent study also revealed how to obtain a strong phase transition by varying the top Yukawa coupling between the broken and symmetric extrema [87]. In ref. [87] the phase transition is strengthened by thermal effects. This is a different mechanism to what we describe in this section which regards the $T = 0$ vacuum energy radiative correction.

According to the lattice results in ref. [2] a weak first order phase transition is found for the Minimal SM. In comparing with the branches in Figure 2.12 the red curve (one loop) is closer to the lattice result than the blue curve (tree+thermal only). A lattice determination of this branch is desirable, but beyond the scope of this thesis. Rather than abandoning perturbation theory we can further validate which approach is more accurate by resumming part of the thermal effective potential.

Including one loop ring-improvement terms (resummation)

For the resummation, we follow the procedure in ref. [68] up to one loop order. This amounts to including a term of the form [68]

$$\Delta V_{\text{ring}} = -g_{i(L)} \frac{T}{12\pi} \left[\mathcal{M}_i^3(\phi, T) - m_i^3(\phi) \right] \tag{2.70}$$

into the bosonic contributions to the high temperature expansion part of the effective thermal potential. This gives what is known as the ring-improved effective potential. Note that only the scalars and longitudinal gauge boson modes appear in the ring term, where their degrees of freedom are denoted by $g_{i(L)}$ in the above. Here $\mathcal{M}_i(\phi, T)$ and $m_i(\phi)$ are the field-dependent thermal mass and field-dependent mass of the i^{th} boson, respectively. The thermal mass (squared) is of the form

$$\mathcal{M}_i^2(\phi, T) = m_i^2(\phi) + \Pi_i(\phi, T), \tag{2.71}$$

where $\Pi_i(\phi, T)$ is a Debye mass term. To leading order $\Pi_i(\phi, T) \propto T^2$. The field-dependent masses are given by

$$m_W^2(\phi) = \frac{1}{2} g_2^2 \phi^2 = \frac{m_W^2}{v^2} \phi^2, \tag{2.72}$$

$$m_Z^2(\phi) = \frac{1}{2} (g_2^2 + g_1^2) \phi^2 = \frac{m_Z^2}{v^2} \phi^2, \tag{2.73}$$

$$m_t^2(\phi) = y_t^2\phi^2 = \frac{m_t^2}{v^2}\phi^2, \tag{2.74}$$

$$m_h^2(\phi) = \frac{1}{2}\frac{\partial^2 V_{\text{tree}}^{[\text{SM}]}(\phi)}{\partial\phi^2} = \frac{m_h^2}{2v^2}\left(-v^2 + 3\phi^2\right). \tag{2.75}$$

The thermal (squared) masses are given by

$$\mathcal{M}_W^2(\phi, T) = \frac{m_W^2}{v^2}\left(\phi^2 + \frac{11}{3}T^2\right), \tag{2.76}$$

$$\begin{pmatrix} \mathcal{M}_Z^2(\phi,T) & 0 \\ 0 & \mathcal{M}_\gamma^2(\phi,T) \end{pmatrix} = \text{diag}\begin{pmatrix} \frac{m_W^2}{v^2}\left(\phi^2 + \frac{11}{3}T^2\right) & -m_Z\sqrt{m_Z^2 - m_W^2}\frac{\phi^2}{v^2} \\ -m_Z\sqrt{m_Z^2 - m_W^2}\frac{\phi^2}{v^2} & \frac{(m_Z^2 - m_W^2)}{v^2}\left(\phi^2 + \frac{11}{3}T^2\right) \end{pmatrix}, \tag{2.77}$$

$$\mathcal{M}_h^2(\phi, T) = \frac{m_h^2}{2v^2}\left(-v^2 + 3\phi^2 + \frac{1}{12}T^2\right) + \frac{(m_t^2 + 2m_W^2 + 2m_Z^2)}{8v^2}T^2. \tag{2.78}$$

The resummation has a noticeable impact of decreasing the strength of the phase transition, see Figure 2.12. This is more consistent with the lattice result [2]. The strength decreases by 10% where the Higgs mass is very small and 30% for $m_h = 125$ GeV. If we include the Higgs into the radiative corrections, the resummation decreases the strength by 10% for any value of the Higgs mass.

Including the Higgs into one loop radiative corrections

Having established that the faded red curve in Figure 2.12 is reliable under our treatment of the effective potential so far, we turn to the final question. Would the shape of the branch change if we include the Higgs in the radiative corrections?

As before, we numerically determine the branch for each set up but now with the Higgs included. To be more specific, we always include the Higgs thermal corrections. Only in the case of the "tree + thermal only" setup do we not include the Higgs in the $T = 0$ radiative corrections, otherwise we do. Similarly, we include a ring term for the Higgs, see eq. (2.70), for the ring-improved one loop potential set up. Comparing the same-coloured dashed and faded curves in Figure 2.12, we can see that including the Higgs has a very small effect on the shape of the branch. The effect is small because the Higgs boson only has one degree of freedom, $g_h = 1$, which is negligible compared to the top quark's and electroweak gauge bosons' number of degrees of freedom.

We notice that the Higgs correction has slightly more impact for larger $|\Delta V_{1\text{ loop (0T)}}|$ on a given curve. Comparing branches for various properties against m_h, we observe that this effect primarily results from a decrease in the critical temperature, as shown in

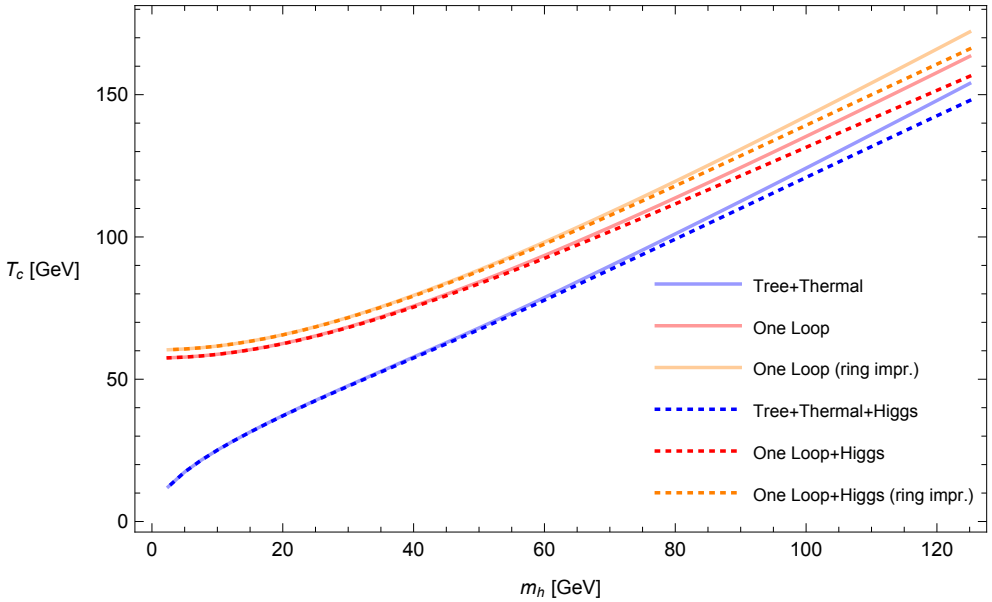

Figure 2.15: Plot of the critical temperature of the phase transition T_c against the Higgs mass m_h. Both axes are in units of GeV. See Figure 2.12 or text for a description of the curves.

Figure 2.15. This decrease becomes less significant as $m_h \to 0$. This can be understood by calculating the Higgs one loop contribution to the vacuum energy difference,

$$\Delta V^{[\mathrm{SM}]}_{1\text{ loop }(0\mathrm{T})\,+\,\mathrm{Higgs}} = \Delta V^{[\mathrm{SM}]}_{1\text{ loop }(0\mathrm{T})} + \frac{1}{2(16\pi)^2} g_h m_h^4 \left(15 + \log(4) - i\,2\pi\right). \tag{2.79}$$

The imaginary piece above derives from the field-dependent Higgs mass squared being negative at the origin, $m_h^2(\phi = 0) = -\frac{1}{2}m_h^2$, see eq. (2.75). This negative term appears in the argument of a log term. We ignore this imaginary piece for the same reason that calculations are performed by taking the real part of the potential. Including the one loop correction for a Higgs of mass 125 GeV decreases the vacuum energy by 6.2% of its tree level value. A more accurate value of the one loop vacuum energy difference for the SM is therefore $\Delta V(0) = -1.259 \times 10^8$ GeV^4, compared to eq. (2.28). A more meaningful value is how much the Higgs contributes to the *radiative* piece of the vacuum energy difference. For $m_h \leq 125$ GeV, the Higgs contributes a less than 10% decrease to the radiative piece. This contribution decreases with m_h, until the vacuum energy is exactly that from the top quark and electroweak gauge bosons.

To summarise, a heavier Higgs has a larger effect on the shape of the branch because it changes the depth of the radiative vacuum energy more. In line with our initial hypothesis, this results in a decrease in the critical temperature compared to the potential without the Higgs included. However, this effect reduces with the Higgs mass until the effective thermal potential is that generated from the top quark and electroweak gauge bosons.

Overall the Higgs radiative contribution has a very small effect on the shape of the branch in the Minimal SM with a variable Higgs mass. We expect it may have a more significant effect in BSM extensions, where the Higgs mass is 125 GeV, so the 10% decrease of the radiative contribution to the vacuum energy persists for all $|\Delta V_{1\text{ loop }(0\text{T})}|$.

This analysis reveals that the shape of the Minimal SM branch is defined by a combination of the existence of the thermal cubic terms from the electroweak gauge bosons and the value of the top quark mass. According to Figure 2.13, the branch is rather sensitive to the top quark mass for low $|\Delta V_{1\text{ loop }(0\text{T})}|$. A significant enough decrease in the top mass allows for a potential with $\Delta V_{1\text{ loop }(0\text{T})} > \Delta V_{\text{tree}}$, instead of $\Delta V_{1\text{ loop }(0\text{T})} < \Delta V_{\text{tree}}$. This lets us tune for an arbitrarily strong phase transition through $T_c \to 0$, instead of $T_c \to$ constant, as $|\Delta V_{1\text{ loop }(0\text{T})}| \to 0$.

2.5 Concluding remarks

In this work, we have investigated in detail the one loop vacuum energy difference at zero temperature, $\Delta V_{1\text{ loop }(0\text{T})}$, and its implications on the strength of the electroweak phase transition, $\xi = \sqrt{2}\, v_c/T_c$. The study was conducted using three single field modifications to the SM, one non-supersymmetric singlet extension to the SM, and a supersymmetric singlet extension (the GNMSSM).

For the single field models investigated, we find that a decrease in $|\Delta V_{1\text{ loop }(0\text{T})}|$ also decreases the critical temperature. In turn the critical field value remains close to its zero temperature value. This leads to a strong ξ-$\Delta V_{1\text{ loop }(0\text{T})}$ correlation with universal behaviour observed at very low $|\Delta V_{1\text{ loop }(0\text{T})}|$, as can be seen in Figure 2.1. This universal behaviour is found in Section 2.3.3 to be fixed by the number of relevant degrees of freedom in the plasma. Parameter points with a strong phase transition are guaranteed with only a moderate tuning of the vacuum energy difference, see eq. (2.61), relative to the SM value in eq. (2.28).

For singlet extended models, we find a similar ξ-$\Delta V_{1\text{ loop }(0\text{T})}$ correlation so long as the fields in the broken vacuum do not slide under thermal effects. This sliding behaviour is most obvious in Section 2.3.3 when we look at the non-supersymmetric model with a $\mathbb{Z}_2$ symmetry imposed on the singlet, called the $\mathbb{Z}_2$xSM. We find that a spontaneous breaking of the $\mathbb{Z}_2$ before the critical temperature disfavours a strong phase transition. Such parameter points fall onto an undesirable region in ξ-$\Delta V_{1\text{ loop }(0\text{T})}$ space. With the exception of the $\mathbb{Z}_2$xSM unbroken at zero temperature, parameter points on this undesirable region almost completely disappear after imposing phenomenological constraints. This can be

seen in Figures 2.2, 2.5, 2.6, and 2.7. The reason so many points are removed is because the phenomenological constraints disallow light singlet states with large Higgs-singlet mixing, see Figure 2.7. In other words, phenomenological constraints work in favour of a strong ξ-$\Delta V_{1\text{ loop }(0\text{T})}$ correlation. This also suggests that to have Higgs-singlet mixing at zero temperature as well as a very strong phase transition, the potential must contain explicit $\mathbb{Z}_2$ symmetry breaking terms.

For the non-supersymmetric singlet extended model with the $\mathbb{Z}_2$ explicitly broken at zero temperature, phenomenological constraints remove the majority of parameter points in our data set. Nonetheless, the surviving points follow the usual ξ-$\Delta V_{1\text{ loop }(0\text{T})}$ correlation and a strong phase transition is guaranteed if $|\Delta V_{1\text{ loop }(0\text{T})}| < 1.03 \times 10^8$ GeV^4.

For the GNMSSM, similar observations to those in the non-supersymmetric singlet extension are made. Three benchmark scenarios are analysed in detail in Section 2.3.4. Once phenomenological constraints are applied, a strong phase transition is guaranteed if $|\Delta V_{1\text{ loop }(0\text{T})}| < 6.98 \times 10^7$ GeV^4. However, this is at the cost of excluding a significant portion of the parameter space with a strong phase transition. Instead a far more useful bound is provided in eq. (2.64). From Figure 2.8 we can see that this bound captures far more of the parameter space with a strong phase transition.

The treatment of the effective potential in this work has allowed us to glimpse at the distinction between tree and $T = 0$ radiative effects on the phase transition. This is understood through our investigation into the Minimal SM with variable Higgs mass. The ξ-$\Delta V_{1\text{ loop }(0\text{T})}$ curve found for this model closely resembles the significant sliding branch of singlet extended models. This observation carries the notion that the sliding of the broken vacuum reduces the tree level barrier. Significant sliding is therefore the extreme case whereby no tree level barrier remains at critical temperature. The phase transition is then determined solely by the radiative piece of the potential.

To summarise our investigation in this chapter, we highlight the take away message in the below box:

Hypothesis

$$\text{As } \Delta V_{1\text{ loop }(0\text{T})} \to 0, \begin{cases} T_c \to 0 \text{ so } \xi \to \infty, & \text{if sliding does not occur,} \\ T_c > 0 \text{ so } \xi \to \text{finite}, & \text{if sliding occurs,} \\ T_c \to 0 \text{ so } \xi \to \infty, & \text{if } \Delta V_{1\text{ loop }(0\text{T})} > \Delta V_{\text{tree}}. \end{cases}$$

We stress that this work does not address the surface tension, tunnelling rate, or the latent heat of the phase transition as measures of the strength of the phase transition. These quantities will indeed depend on the actual height of the barrier, so that we do not necessarily expect a universal behaviour correlated to the vacuum energy. Such investigations will be carried out throughout the rest of this thesis.

We hope that our results make phenomenological studies with parameters exhibiting a strong phase transition far easier to address. This can be useful for model builders that want a strong phase transition, without the need for any finite temperature calculations.

Chapter 3

Phase transitions: a technical interlude

> "Imagine two adjacent hills in a grassy field. One hill is higher than the other. Where on the higher hill would you release a ball in order for the ball to come to rest exactly on top of the lower hill?"

A two field scalar potential is a smooth surface with a set of local extrema and ridges/valleys between them. The potential looks like a series of hills of various sizes in a field of very well cut grass, hence the above statement. Such potentials are found in any extension of the SM by an additional scalar sector.

For a dedicated investigation of the electroweak phase transition, one must determine what is known as the bounce solution. This can be a very involved task for models with a scalar potential described by two or more fields. Finding the bounce solution is analogous to correctly answering the question immediately below the heading of this chapter. The keen experimentalist may well have the urge to find the starting point of the ball by trial and error. This is an impossible task; the condition of the ball coming to a stop at the exact peak of the hill requires an infinite precision in the starting location. However, the ball will pass close to the peak at a minimal speed for some starting points. One would hope that such paths the ball takes are not dissimilar.

Before jumping into the deep end with a two field potential, it is worth reviewing a far simpler case first: that of a single field potential. In this short chapter we will review the bounce solution and the decay of the false vacuum [30, 88–92]. Here we describe the mathematical formalism of the bounce solution and its connection with the properties of the phase transition.

3.1 The bounce solution

To find the bubble configuration for a scalar potential with n fields, one must solve the equations of motion [92]

$$\frac{d^2\phi_i(\rho)}{d\rho^2} + \frac{\alpha-1}{\rho}\frac{d\phi_i(\rho)}{d\rho} = \frac{dV(\phi_1,\phi_2,...\phi_n)}{d\phi_i} \text{ for } i = 1,2,...n, \tag{3.1}$$

where α carries the notion of a damping factor and $\phi_i(\rho)$ is the i^{th} field as a function of a radial coordinate ρ. The radial coordinate is the only argument of the fields because of an assumed $O(\alpha)$ spherical spacetime symmetry. Alongside our hills in a field analogy of the scalar potential, the α parameter can be seen as representative of the frictional effects acting on the ball, i.e. air resistance or not so well cut grass. In thermal field theory, the time direction carries the notion of inverse temperature, so $\alpha = 3$ for thermally induced vacuum-to-vacuum transitions. We do not consider the possibility of relaxing this symmetry since it will make the problem far more difficult.

There are many solutions to eq. (3.1). Conceptually these solutions are trajectories that a ball would follow on the inverted potential, in accordance with the classical laws of Newtonian mechanics. However, we are only interested in those that describe the transition from false vacuum to true vacuum. This type of solution is subject to the boundary conditions

$$\frac{d\phi_i(0)}{d\rho} = 0 \text{ and } \phi_i(\infty) = (\phi_i)_{\text{false}} \tag{3.2}$$

and is called a bounce solution. Conceptually, the bounce solution is the trajectory taken by a classical particle released from rest somewhere close to the true vacuum and coming to rest at exactly the false vacuum after an infinite amount of time on the surface of the inverted potential. Attempting to find the bounce solution for a potential with two or more fields can be difficult, especially when the potential lacks (geometrical) symmetry.

For a single field potential, finding the bounce solution by numerical means is trivial. Depending on the initial field value, the trajectory will either undershoot or overshoot the false vacuum. Undershooting refers to the solution not reaching the false VEV and then oscillating about the minimum of the inverted potential. Overshooting refers to the solution reaching the false VEV and then blowing up due to the inverted potential being bound from above. An under/overshooting iterative procedure is used to determine the bounce solution. There even exists a special single field potential whereby the bounce solution can be found analytically. This is the subject for the remainder of this chapter.

The reader familiar with the work in refs. [30, 88–91] can skip to Chapter 4.

3.2 Quantum phase transitions

Any model described by quantum field theory (at zero temperature) has a scalar potential that is, in general, determined by three types of quantities. These quantities are the scalar fields (space-time dependent objects), the masses of the relevant particles in the theory (dimensionful objects), and couplings of interactions (dimensionless objects). Each quantity in the potential further depends on the renormalisation scale. So for a fixed renormalisation scale, all quantities are fixed. With masses and couplings fixed by observations, the (zero temperature) potential only depends explicitly on the fields.

Taking the ϕ^4 theory tree level potential,

$$V(\phi) = \frac{m_h^2}{4v^2}\left(\phi^2 - v^2\right)^2, \tag{3.3}$$

we will review phase transitions in parallel with [30]. This is a single field potential with exactly degenerate minima and can be used to determine the bounce solution analytically. For the case of one spacetime coordinate we have $\alpha = 1$. This is referred to as the case of no damping since $\alpha = 1$ kills the first order derivative in eq. (3.1). One can derive the solution to the equation of motion, with eq. (3.2) boundary conditions, to be

$$\phi(\rho) = v \tanh\left[\frac{\rho}{L_w}\right]. \tag{3.4}$$

where $L_w = \sqrt{2}/m_h$ is the wall thickness. This is called the *thin wall* solution. This solution starts at $\phi(\rho \to -\infty) = -v$ and ends at $\phi(\rho \to +\infty) = v$. Using the solution in eq. (3.4), the kinetic energy is given by

$$K(\rho) \equiv \frac{1}{2}\left[\phi'(\rho)\right]^2 = V_0 \,\mathrm{sech}^4\left[\frac{\rho}{L_w}\right], \tag{3.5}$$

where $V_0 = \frac{1}{4}m_h^2 v^2$ is the barrier height. This is consistent with the principle of conservation of energy: the maximum kinetic energy occurs for the minimum potential energy in the inverted potential. The one-dimensional action, known as the surface tension, is

$$S_1 = \int_{-\infty}^{+\infty} d\rho \left[K(\rho) + V(\rho)\right] = \frac{4\sqrt{2}}{3}\frac{V_0}{m_h} = \frac{\sqrt{2}}{3} m_h v^2. \tag{3.6}$$

Given m_h, the surface tension is an effective measure of the barrier height. By definition it is evaluated for a potential (at a temperature) when the relevant vacua are degenerate, so it is always calculable in the thin wall approximation.

To calculate the action in four-dimensional space-time, a spherically symmetric space-time is assumed for simplicity. The thin wall approximation may then be considered as the solution in the radial direction $\rho \geq 0$. The solution is suggested in [30] to be

$$\phi(\rho) = \begin{cases} -v & \text{for } \rho \ll R, \\ v \tanh\left[\dfrac{\rho - R}{L_w}\right] & \text{for } \rho \approx R, \\ v & \text{for } \rho \gg R, \end{cases} \tag{3.7}$$

where R is the critical radius of the bubble. Note there is a shift of the radial coordinate ρ to the positive domain $[0, +\infty]$. The four-dimensional Euclidean action, in the thin wall approximation, is given by

$$S_4 = 2\pi^2 \int_0^{+\infty} d\rho \rho^3 \left[K(\rho) + V(\rho)\right] \approx 2\pi^2 R^3 S_1. \tag{3.8}$$

Once we consider a model in thermal field theory, the potential changes shape depending on the temperature of the surrounding plasma. The critical temperature T_c is defined at when the two relevant vacua are degenerate. The start of the phase transition (nucleation temperature T_n) cannot happen at T_c but occurs at a lower temperature. The thin wall approximation is most reliable when T_n is very close to the critical temperature. We introduce a term to the potential that breaks the vacuum degeneracy to see how the action S_4 changes, but not by too much as to invalidate the solution in eq. (3.4). The term originally added to eq. (3.3) to break the degeneracy is linear in the field,

$$V_{\text{non-deg}}(\phi) = \frac{|\Delta V(0)|}{2v}(\phi + v). \tag{3.9}$$

This modifies the four-dimensional Euclidean action of eq. (3.8) to give

$$S_4 \approx 2\pi^2 R^3 S_1 - \frac{1}{2}\pi^2 R^4 |\Delta V(0)|. \tag{3.10}$$

Note that $\Delta V(0) \equiv V(\phi_i, T = 0)|_{\text{true}} - V(\phi_i, T = 0)|_{\text{false}}$ is the vacuum energy difference at zero temperature, where the true vacuum is at $\phi = v$. Minimising the action in eq. (3.10) with respect to R, we find that the critical radius is given by $R \approx 3S_1/|\Delta V(0)|$. The four-dimensional Euclidean action is written compactly as

$$S_4 \approx \frac{27\pi^2 S_1^4}{2|\Delta V(0)|^3}. \tag{3.11}$$

Physically, this action describes a purely quantum mechanical vacuum-to-vacuum transition, i.e. a *quantum phase transition*. Its corresponding decay rate is given by [30, 88]

$$\left(\frac{\Gamma}{V}\right)_{\text{quantum}} = A\exp\left[-S_4\right], \text{ where } A \sim \mathcal{O}(1). \tag{3.12}$$

3.3 Thermal vacuum transitions

Since we are interested in the electroweak phase transition what we really want is the three-dimensional Euclidean action, where the time coordinate carries the notion of inverse temperature [89–91]. This is achieved by a Wick rotation of the time coordinate, known in thermal field theory as the imaginary (Matsubara) time formalism. Schematically this means our four-dimensional Euclidean action may be written as

$$S_4 = \int_0^{1/T} d\beta \int_{-\infty}^{\infty} d^3x\mathcal{L}(T) = \frac{1}{T}\int_{-\infty}^{\infty} d^3x\mathcal{L}(T) = \frac{S_3(T)}{T}, \tag{3.13}$$

where the time direction β is periodic in $1/T$. The formal treatment of *turning on temperature* comes at the level of connecting a thermal ensemble to the partition function

$$Z = \text{Tr}\left[\exp(-\beta\hat{H})\right] = \sum_n \langle n|\exp(-\beta\hat{H})|n\rangle. \tag{3.14}$$

where $\hat{H}$ is the Hamiltonian. As an example, this modifies all two-point correlation functions (propagators) of the theory

$$\langle\phi_1\phi_2\rangle = \text{Tr}\left[\exp(-\beta\hat{H})\phi_1\phi_2\right] \tag{3.15}$$

and adds a temperature-dependent term to the propagator. The temperature-dependence reduces the mass of the propagating particle as the temperature is increased.

Returning to phase transition analytics, we may recycle most of the expressions found in the zero temperature case where the thin wall approximation ought to be valid. Note that vacuum degeneracy now means $\Delta V(T) \to 0$. Thin wall is expected to be valid at temperatures close to the critical temperature. The three-dimensional action is given by

$$S_3(T) \approx 4\pi R^2 S_1 - \frac{4}{3}\pi R^3|\Delta V(T)|, \tag{3.16}$$

where the critical radius is given by $R \approx 2S_1/|\Delta V(T)|$. Hence the thin wall approximation

is more valid as this radius blows up. Written compactly, the three-dimensional action is

$$S_3(T) \approx \frac{16\pi S_1^3}{3|\Delta V(T)|^2}. \tag{3.17}$$

For the electroweak phase transition, we will be interested in various properties at nucleation temperature T_n. Note that the temperature-dependence of both S_3 and R come through the free energy density difference at temperature, $\Delta V(T)$.

Therefore at nucleation temperature the relations eq. (3.16)-(3.17) are only reliable if $T_n \approx T_c$, where the thin wall approximation is valid. The contrasting case is that of a phase transition with significant supercooling $T_n \ll T_c$, whereby $|\Delta V(T_n)|^{3/4}$ is not small compared with S_1. In such a case, we must rely on a numerical computation for $S_3(T_n)$. The thermal decay rate is given by [89–91]

$$\left(\frac{\Gamma}{V}\right)_{\text{thermal}} = AT^4 \left(\frac{S_3(T)}{2\pi T}\right)^{3/2} \exp\left[-\frac{S_3(T)}{T}\right], \text{ where } A \sim \mathcal{O}(1). \tag{3.18}$$

The probability of nucleating a bubble through thermal effects is zero at $T = 0$ and $T = T_c$. Both are caused by the exponent in eq. (3.18) becoming largely negative. At zero temperature, $S_3(T)$ is finite and $T \to 0$ trivially blows up the exponent. At critical temperature $S_3(T_c) \to \infty$ as the critical radius tends to infinity in order to compensate for $|\Delta V(T_c)| \to 0$, refer to eq. (3.16).

3.4 Concluding remarks

In reality, both the quantum and thermal phase transitions are "switched on" and therefore the decay rates superimpose to provide a total decay rate for the false to true vacuum transition. However, we will ignore the quantum phase transition (zero temperature) contribution to the decay rate. Although it would positively contribute to the decay rate, it is often negligible compared to the thermal decay rate at electroweak scale temperatures.

Note that for the work in the next chapter, the start of the phase transition is often far from the critical temperature. This means that the thin wall approximation will not likely hold and, hence, neither will most expressions in this chapter. Nonetheless, we can calculate the phase transition properties by numerical means using the concepts covered in this chapter.

Chapter 4

Singlet extended SM: the unbroken $\mathbb{Z}_2$xSM

"Everything should be made as simple as possible but not simpler."

- *Albert Einstein*

A useful guiding principle in theoretical physics is to explore interesting phenomena using models with as few free parameters as possible. In this chapter we will explore one such model. The model we choose is a real singlet extension of the Standard Model (SM). A minimal number of free parameters is found if we impose a $\mathbb{Z}_2$ symmetry on the real singlet S field and set $\langle S \rangle = 0$ in the broken vacuum. We occasionally refer to this as the unbroken $\mathbb{Z}_2$xSM. This model therefore has a simple two field scalar potential. A simple two field potential is a desirable (to use an appropriate word) *step* in understanding the cosmological history of the universe [93].

Previous literature has explored the realm of singlet-extended potentials with a $\mathbb{Z}_2$ symmetry to either:

(i) understand the vacuum structure and model configurations,

(ii) determine the nature of the electroweak phase transition,

(iii) test parameter points against collider/dark matter constraints,

(iv) address the viability of electroweak baryogenesis,

(v) investigate the production of gravitational waves at the electroweak scale,

or amalgamations of the above points [24, 27, 73, 93–101]. The following work fits into the (i) and (ii) categories, with a brief section on (v). Although our primary focus is on

the nature of the phase transition for a specific parameter subspace for this model. This parameter subspace is the physically allowed region in which bubbles' walls are expected to be runaway, or very fast detonations, at the start of the phase transition [31]. Our work (literally) draws out this region of the parameter space which promises the strongest and most supercooled electroweak phase transitions. Towards the end of the study we investigate some implications that the phase transition properties have on acoustically-generated gravitational wave production [33, 102].

In Section 4.1 we describe the tree level and one loop (including thermal evolution) vacuum structure in detail. Here we explore the vacuum structure of the potential using an analytic approach. Our analysis is complimentary to that in ref. [99]. This includes low/high temperature analytic expressions to the thermal evolution of the Higgs field in the broken vacuum. We discuss the parameter region of interest that will be explored in Section 4.2. We comment on the symmetry breaking pattern necessary to realise this desirable scenario for studying very strong electroweak phase transitions. Any reader interested in only the numerical results can skip to Section 4.2.

In Section 4.3 we outline the region in which the phase transition is expected to proceed by bubbles with runaway walls. This is the region of maximal supercooling for the non-sliding parameter space. Three physical scenarios at the start of the phase transition describe the edges around this region. These edges are associated to when (1) the bubble wall velocity is expect to runaway, (2) roughly one bubble is nucleated per Hubble volume, and (3) the symmetric vacuum destabilises. Finally, we calculate an effective friction parameter and the expected relic density from acoustically-generated gravitational waves, produced during the electroweak phase transition. We conclude in Section 4.7.

4.1 The unbroken $\mathbb{Z}_2$xSM: analytics

Our choice of model is motivated by its simple structure and richness in studying the electroweak phase transition. This model may be realisable in many UV completions of the Standard Model (SM), including composite Higgs and supersymmetric singlet extensions such as the GNMSSM. It was found in [1, 27, 96, 99, 103] that the unbroken $\mathbb{Z}_2$xSM can easily be tuned to have an arbitrarily strong phase transition, as measured by $\sqrt{2}\langle\phi\rangle/T$ at critical temperature. The phase transition becomes strong by lowering the symmetric extremum of the zero temperature potential towards the broken vacuum by an additional field direction. This tuning of the zero temperature potential is the most obvious mechanism for reducing the critical temperature of the phase transition [1, 95, 96, 104].

4.1.1 At tree level

The tree level potential is given by

$$V_{\text{tree}}(\phi, S) = \frac{1}{2}m_h^2\phi^2\left(\frac{\phi^2}{2v^2} - 1\right) + \frac{a_2}{2}\phi^2 S^2 + \frac{1}{2}\tilde{m}_s^2 S^2\left(\frac{S^2}{2\tilde{v}_S^2} - 1\right), \tag{4.1}$$

where $\phi = \text{Re}(H^0)$ and H^0 is the neutral component of the SM Higgs doublet. This is the simplest singlet extension of the Standard Model (SM). The singlet sector consists of a real singlet with a $\mathbb{Z}_2$ symmetry imposed on it. We only consider potentials with the broken vacuum at $(\phi, S) = (v, 0)$ and the symmetric extremum at $(\phi, S) = (0, \tilde{v}_S)$ at zero temperature. We use the convention that $v = 174.2$ GeV.

The field dependent Higgs/singlet mass is

$$\mathcal{M}_{h,s}^2(\phi, S) = \frac{1}{2}\left[m_\phi^2(\phi, S) + m_S^2(\phi, S)\right] \pm \sqrt{\frac{1}{4}\left[m_\phi^2(\phi, S) - m_S^2(\phi, S)\right]^2 + (a_2\phi S)^2}, \tag{4.2}$$

where the field dependent masses in the ϕ and S field directions are given by

$$m_\phi^2(\phi, S) = \frac{m_h^2}{2}\left(3\frac{\phi^2}{v^2} - 1\right) + \frac{a_2}{2}S^2 \quad \text{and} \quad m_S^2(\phi, S) = \frac{\tilde{m}_s^2}{2}\left(3\frac{S^2}{\tilde{v}_S^2} - 1\right) + \frac{a_2}{2}\phi^2, \tag{4.3}$$

respectively. In both the broken and (possibly) symmetric vacua the Higgs and singlet do not mix at zero temperature. Throughout this chapter we define the following zero

temperature masses:

	Broken vacuum	**Symmetric extremum**
Higgs	$m_h^2 \equiv \mathcal{M}_h^2(v,0) = m_\phi^2(v,0)$	$\tilde{m}_h^2 \equiv \mathcal{M}_h^2(0,\tilde{v}_S) = m_\phi^2(0,\tilde{v}_S)$
Singlet	$m_s^2 \equiv \mathcal{M}_s^2(v,0) = m_S^2(v,0)$	$\tilde{m}_s^2 \equiv \mathcal{M}_s^2(0,\tilde{v}_S) = m_S^2(0,\tilde{v}_S)$

(4.4)

We insist on the following zero temperature vacuum structure for this study:

(1) The broken electroweak vacuum is a local minimum.

This requires $m_h^2 > 0$ and $m_s^2 = \frac{1}{2}(a_2 v^2 - \tilde{m}_s^2) > 0$. Therefore

$$\tilde{m}_s^2 < a_2 v^2. \tag{4.5}$$

(2) The broken vacuum is the deepest vacuum.

By condition **(1)**, the broken vacuum is one of two possible local minima. The other possible vacuum is the symmetric extremum located at $\phi = 0$ and $S = \tilde{v}_S$. For the broken vacuum to be lower than the symmetric extremum $V_{\text{tree}}(v,0) < V_{\text{tree}}(0,\tilde{v}_S)$, or

$$|\tilde{m}_s \tilde{v}_S| < |m_h v|. \tag{4.6}$$

(3) The depth of the potential is less than that in the SM.

The potential in the $S = 0$ direction is fixed by the SM. The potential difference between the broken and symmetric extrema can only be reduced by bring down the symmetric extremum. Without radiative corrections, this can only be realised if $m_S^2(0,0) < 0$ so that $\tilde{v}_S \neq 0$.

(4) Potential bounded from below in all field space.

By condition **(3)**, the potential along the singlet direction (along $\phi = 0$) initially decreases upon increasing S field values. We must ensure that the potential turns over so that it increases upon increasing values of S. This requires $\tilde{m}_s^2 > 0$. Given condition **(1)** this also means $a_2 > 0$.

(5) Symmetric extremum: saddle point or local minimum?

Finally, we evaluate the curvature of the potential in the symmetric extremum, $\tilde{m}_h^2 = \frac{1}{2}(a_2 \tilde{v}_S^2 - m_h^2)$. Given condition **(4)**, the sign of $\tilde{m}_h^2$ determines the nature of the

symmetric extremum at zero temperature:

$$\textbf{Saddle point: } \tilde{m}_h^2 \leq 0 \Rightarrow a_2 \tilde{v}_S^2 \leq m_h^2, \tag{4.7}$$

$$\textbf{Local minimum (vacuum): } \tilde{m}_h^2 > 0 \Rightarrow a_2 \tilde{v}_S^2 > m_h^2. \tag{4.8}$$

The Higgs and singlet only communicate to each other through the mixing term of the form $\phi^2 S^2$. The coupling can be rewritten as $a_2 = (2m_s^2 + \tilde{m}_s^2)/v^2$. Therefore this mixing is simply a comparison of the singlet mass scales. The study in [100] remarks on the reliability of the perturbative approach to this model, to which they find a value of $a_2 \gtrsim 10$ is questionable. We therefore regard $a_2 = 10$ as the upper bound for a reliable perturbative analysis. From condition **(4)** above, negative values of a_2 are forbidden. This is essential because it would result in $m_s^2 < 0$ and the broken vacuum would have $\langle S \rangle \neq 0$. Although this is not forbidden, the resulting phase transition strength tends to be significantly weaker, see Figure 2.2.

With regards to collider constraints, the $h \to ss$ channel opens up if $m_s \leq m_h/2$. This results in a significant broadening of the Higgs decay width [98]. We choose to ignore this bound throughout this work. This is because we are more interested in exploring how the singlet mass effects the phase transition properties. Nonetheless, it turns out $m_s < m_h/2$ only occurs for $a_2 = 1$ if the phase transition is very strong. This can be seen in our numerical results, see Figure 4.12(a). Imposing perturbative unitarity of the singlet results in $\tilde{m}_s^2 \lesssim 4\tilde{v}_S^2$ [76]. For our parameter points in Section 4.4 this means all points with $a_2 = 10$ violate unitarity, whereas all points with $a_2 = 1$ satisfy the unitarity constraint. The ρ parameter, which arises from corrections to the W boson mass, does not constrain this model. This is because the Higgs and singlet strictly do not mix in the broken vacuum for this model. Constraints from the ρ parameter are expected to appear at two loop level.

If $\tilde{m}_h^2 > 0$ there exists one extra local extremum in the potential. This is because of the geometry of the potential: if the symmetric extremum is a local minimum there must be a maximum in the minimised path (see Section 4.3.1) since both the broken and symmetric extrema are both minima. To be along the minimised path, the peak of the potential barrier must have both a minimum and maximum direction. This non-trivial extremum is therefore a saddle point. Minimising the potential in the ϕ and S directions,

we find the extra local extremum at

$$\phi = C\frac{\tilde{m}_h}{m_h}v \quad \text{and} \quad S = C\frac{m_s}{\tilde{m}_s}\tilde{v}_S, \tag{4.9}$$

where C is a constant given by

$$C = \sqrt{2}\left[\left(a_2\frac{v}{m_h}\frac{\tilde{v}_S}{\tilde{m}_s}\right)^2 - 1\right]^{-1/2}. \tag{4.10}$$

The combination of conditions **(2)** and $\tilde{m}_h^2 > 0$ imply that $C^2 > 0$.

4.1.2 At one loop zero temperature

We will only consider one loop contributions to the potential that come from the top quark and electroweak gauge bosons. By not including the Higgs and singlet in the one loop corrections, only the purely ϕ dependent terms of the potential are modified upon loop corrections. At zero temperature, loop effects are included using Coleman-Weinberg type terms [105] to give the effective one loop potential

$$V_{1\text{ loop}}(\phi, S) = V_{\text{tree}}(\phi, S) + V_{\text{ct}}(\phi) + \Delta V_{1\text{ loop}}(\phi), \tag{4.11}$$

where we adopt counter terms in the form

$$V_{\text{ct}}(\phi) = \frac{1}{2}\delta_m\phi^2 + \frac{1}{4}\delta_\lambda\phi^4. \tag{4.12}$$

The one loop Coleman-Weinberg type effective potential in $\overline{DR}$ scheme is given by

$$\Delta V_{1\text{ loop}}(\phi) = \frac{1}{64\pi^2}\frac{\phi^4}{v^4}\sum_i g_i(-1)^{2s_i}m_i^4\left\{\log\left[\frac{m_i^2\phi^2}{Q^2v^2}\right] - \frac{3}{2}\right\}, \tag{4.13}$$

where g_i, s_i, and m_i are the number of degrees of freedom, spin, and pole mass of i^{th} particle, respectively. The symbol Q is the renormalisation scale. Unless otherwise stated we choose $Q = m_t$. We choose our renormalisation conditions such that the Higgs mass m_h and vacuum expectation value v in the broken vacuum are unchanged upon radiative corrections. The counter terms are found to be $\delta_m = -\zeta_m/v^2$ and $\delta_\lambda = \zeta_\lambda/v^4$, where

$$\zeta_m = \frac{1}{(4\pi)^2}(g_t m_t^4 - g_W m_W^4 - g_Z m_Z^4) \tag{4.14}$$

and

$$\zeta_\lambda = \frac{1}{(4\pi)^2}\left(g_t m_t^4 \log\left[\frac{m_t^2}{Q^2}\right] - g_W m_W^4 \log\left[\frac{m_W^2}{Q^2}\right] - g_Z m_Z^4 \log\left[\frac{m_Z^2}{Q^2}\right]\right). \tag{4.15}$$

This results in a potential of the form

$$\begin{aligned} V_{1\text{ loop}}(\phi, S) = \; & -\frac{1}{2}\left[m_h^2 v^2 + \zeta_m\right]\frac{\phi^2}{v^2} + \frac{1}{4}\left[m_h^2 v^2 + \zeta_m\left(\frac{3}{2} - \log\left[\frac{\phi^2}{v^2}\right]\right)\right]\frac{\phi^4}{v^4} \\ & + \frac{a_2}{2}\phi^2 S^2 + \frac{1}{2}\tilde{m}_s^2 S^2\left(\frac{S^2}{2\tilde{v}_S^2} - 1\right). \end{aligned} \tag{4.16}$$

Compared to the tree level potential, an additional term of the form $\phi^4 \log[\phi^2/v^2]$ appears and ζ_m is the only loop level parameter in the potential. Since ζ_λ does not appear, the potential is independent of the renormalisation scale Q. Only $m_\phi^2(\phi, S)$ is modified upon one loop corrections. The first expression in eq. (4.3) changes to

$$m_\phi^2(\phi, S) = \frac{m_h^2}{2}\left(3\frac{\phi^2}{v^2} - 1\right) + \frac{a_2}{2}S^2 - \frac{\zeta_m}{2v^4}\left[v^2 + \phi^2\left(-1 + 3\log\left[\frac{\phi^2}{v^2}\right]\right)\right]. \tag{4.17}$$

The vacuum structure conditions are modified as follows:

(1) The broken electroweak vacuum is a local minimum.

Unchanged.

(2) The broken vacuum is the deepest vacuum.

Requires $V_{1\text{ loop}}(v, 0) < V_{1\text{ loop}}(0, \tilde{v}_S)$. Only the potential in the broken vacuum is modified, $V_{1\text{ loop}}(v, 0) = V_{\text{tree}}(v, 0) - \zeta_m/8$. Therefore

$$|\tilde{m}_s \tilde{v}_S| < |m_h v|\sqrt{1 + \frac{\zeta_m}{2m_h^2 v^2}}. \tag{4.18}$$

(3) The depth of the potential is less than that in the SM.

Unchanged.

(4) Potential bounded from below in all field space.

Due to the presence of the log term in the potential, the quartic coupling turns negative for too large a value of ϕ. This drives the potential along $S = 0$ downwards for $|\phi| > |\phi_{\text{instab}}|$. The value of ϕ_{instab} is the ϕ solution to

$$\left[1 - \left(1 + \frac{m_h^2 v^2}{\zeta_m}\right)^{-1} \log\left(\frac{\phi}{v}\right)^2\right]\left(\frac{\phi}{v}\right)^2 = 1. \tag{4.19}$$

Given that ζ_m and m_h are fixed by experimentally measured values, we numerically determine that $\phi_{\text{instab}} = 1.084 \times 10^4$ GeV. It is interesting to note that as $m_h \to 0$, the field value at which the potential turns over is $\phi_{\text{instab}} \to v$. In the limit $\phi_{\text{instab}} \gg v$, the expression in eq. (4.19) is approximated by the term in the square brackets being equal to zero. We can then analytically express the field value as

$$\phi_{\text{instab}} \approx v \exp\left[\frac{1}{2}\left(1 + \frac{m_h^2 v^2}{\zeta_m}\right)\right] = 1.085 \times 10^4 \text{ GeV}. \tag{4.20}$$

Compared to the numerically determined value, there is a 0.1% difference. The potential difference (barrier height) between the broken vacuum and this field value is $V_{1\text{ loop}}(\phi_{\text{instab}}, 0) - V_{1\text{ loop}}(v, 0) = 1.218 \times 10^{14}$ GeV^4.

(5) Symmetric extremum: saddle point or local minimum?

The change in the field dependent mass in the ϕ direction modifies this condition to:

$$\textbf{Saddle point: } \tilde{m}_h^2 \leq 0 \Rightarrow a_2 \tilde{v}_S^2 \leq m_h^2 + \frac{\zeta_m}{v^2}, \tag{4.21}$$

$$\textbf{Local minimum: } \tilde{m}_h^2 > 0 \Rightarrow a_2 \tilde{v}_S^2 > m_h^2 + \frac{\zeta_m}{v^2}. \tag{4.22}$$

Finding one loop corrections to eqs. (4.9) and (4.10) exactly is impossible because the presence of the log term in the potential. We do not attempt to find any further zero temperature results by analytic means.

4.1.3 At thermal one loop (high temperature approximation)

At non-zero temperatures, $T \neq 0$, one loop thermal effects are included using a high and low temperature approximation [106, 107], where relevant, in combination with an interpolation between the two approximations to provide the effective one loop thermal potential $V_T(\phi, S)$ [70]. See eqs. (2.23) and (2.24) for the piecewise analytic expressions for a given particle. We include thermal radiative corrections from the top quark and electroweak gauge bosons via a high temperature expansion,

$$\Delta V_{\text{HT}}(\phi; T) = \text{constant} \times T^4 + \frac{1}{2}\left[DT^2\right]\frac{\phi^2}{v^2} - \frac{1}{3}\left[ET\right]\frac{\phi^3}{v^3} + \frac{1}{4}\left\{\zeta_T(T) + \zeta_m \log\left[\frac{\phi^2}{v^2}\right]\right\}\frac{\phi^4}{v^4}, \tag{4.23}$$

where

$$D = \frac{1}{24}(g_t m_t^2 + 2g_W m_W^2 + 2g_Z m_Z^2), \qquad E = \frac{1}{4\pi}(g_W m_W^3 + g_Z m_Z^3), \quad \text{and} \tag{4.24}$$

$$\zeta_T(T) = \frac{1}{(4\pi)^2}\left(g_t m_t^4 \log\left[\frac{m_t^2}{c_F T^2}\right] - g_W m_W^4 \log\left[\frac{m_W^2}{c_B T^2}\right] - g_Z m_Z^4 \log\left[\frac{m_Z^2}{c_B T^2}\right]\right). \quad (4.25)$$

The finite temperature parameters are given by $c_F = \exp(5.41)$ and $c_B = \exp(2.64)$. The addition of the above thermal piece to the potential in eq. (4.16) results in

$$\begin{aligned} V_{\rm HT}(\phi, S; T) = \;& V_{1\text{ loop}}(\phi, S) + \Delta V_{\rm HT}(\phi; T) \\ =\;& \text{constant} \times T^4 + \frac{1}{2}\left[DT^2 - (m_h^2 v^2 + \zeta_m)\right]\frac{\phi^2}{v^2} - \frac{1}{3}\left[ET\right]\frac{\phi^3}{v^3} \\ & + \frac{1}{4}\left[m_h^2 v^2 + \frac{3}{2}\zeta_m + \zeta_T(T)\right]\frac{\phi^4}{v^4} + \frac{a_2}{2}\phi^2 S^2 + \frac{1}{2}\tilde{m}_s^2 S^2\left(\frac{S^2}{2\tilde{v}_S^2} - 1\right). \end{aligned} \quad (4.26)$$

Note that the log terms in the zero temperature and thermal corrections cancel exactly. The effective thermal quartic coupling is $\lambda_T = \lambda_T(T)$, such that $V_{\rm HT}(\phi, S; T) \supset \frac{1}{4}\lambda_T \phi^4$. To explicitly see the temperature-dependence of $\lambda_T(T)$ we split the function $\lambda_T(T)$ into two parts, $\lambda_T(T) = \lambda_Q + \Delta\lambda_T(T)$. Recalling the definition of ζ_λ in eq. (4.15) we find $\lambda_Q \equiv \lambda_T(Q) = [m_h^2 v^2 + \frac{3}{2}\zeta_m + \zeta_\lambda - \zeta_c]/v^4$ and $\Delta\lambda_T(T) = [2\zeta_m \log(Q/T)]/v^4$, where

$$\zeta_c = \frac{1}{(4\pi)^2}\left(g_t m_t^4 \log c_F - \left(g_W m_W^4 + g_Z m_Z^4\right)\log c_B\right). \quad (4.27)$$

Therefore the effective thermal quartic coupling goes as

$$\lambda_T(T) = \lambda_Q + 2\frac{\zeta_m}{v^4}\log\left[\frac{Q}{T}\right]. \quad (4.28)$$

Field thermal evolution without sliding behaviour

Let us assume the broken electroweak vacuum remains at $S = 0$ between zero temperature and the critical temperature T_c of the electroweak phase transition[1]. Minimising the potential in the ϕ direction, we find

$$\partial_\phi V_{\rm HT} = 0 \text{ occurs for } \begin{cases} \phi = 0 \\ \phi(T) = \dfrac{1}{\sqrt{\lambda_T}}\left[\dfrac{1}{2}\varepsilon_T T \pm \sqrt{\dfrac{1}{4}\varepsilon_T^2 T^2 + M_h^2(T)}\right], \end{cases} \quad (4.29)$$

where we have defined

$$\varepsilon_T = \frac{1}{\sqrt{\lambda_T}}\frac{E}{v^3} \qquad \text{and} \qquad M_h^2(T) = \frac{m_h^2 v^2 + \zeta_m - DT^2}{v^2}. \quad (4.30)$$

[1]Sliding behaviour is defined by the scenario in which the broken vacuum exists at $S \neq 0$ at critical temperature. This may similarly be described by the destabilisation of the broken vacuum in the S direction as the temperature is increased *before* reaching critical temperature.

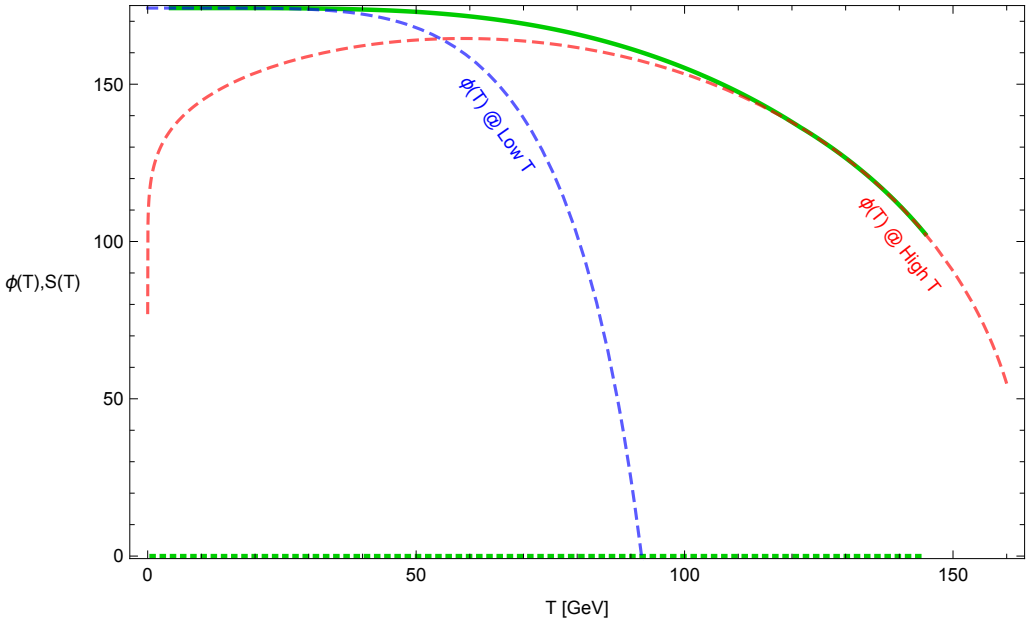

Figure 4.1: The thermal evolution of the Higgs $\phi(T)$ and singlet $S(T)$ fields in the broken vacuum between $0 < T < T_c$ for a non-sliding parameter point with $\xi_c \equiv \sqrt{2}\, v_c/T_c = 1$ and any value of a_2 (green curves). An increase in the strength ξ_c decreases the critical temperature T_c with a one-to-one mapping. Therefore the choice of strength ξ_c only determines the endpoint in T of the green trajectories. For example, had we chosen $\xi_c > 1$ we would follow the same green trajectories but the endpoint (the critical temperature) would be lower. Therefore, any parameter points in the non-sliding region with the same strength ξ_c will have the same $\phi(T)$ trajectory. At zero temperature $\phi(0) = v$ and $S(0) = 0$ as shown by the solid and dotted green curves, respectively. The red and blue dashed curves are the high and low temperature approximation solutions for $\phi(T)$ respectively, see eq. (4.29) and eq. (4.40).

The minimised potential in the S direction gives the same result as in eq. (4.46), since no couplings to the singlet have any temperature dependence in our setup. The thermal evolution of the field dependent Higgs mass along the $S = 0$ direction is given by

$$\mathcal{M}^2_{h(T)}(\phi, S = 0; T) = -\frac{1}{2} M_h^2(T) - \sqrt{\lambda_T}\epsilon_T T\phi + \frac{3}{2}\lambda_T \phi^2. \tag{4.31}$$

The second quantity in eq. (4.30) is thus directly related to the Higgs mass evaluated at the origin. Noting eq. (4.28), the non-trivial solution in eq. (4.29) can be explicitly written in terms of the temperature.

In Figure 4.1, we display the $\phi(T)$ solution in eq. (4.29) with a positive sign before the square root by the red dashed curve. This solution coincides with the numerically determined parameter points from Section 4.4 that have a high critical temperature. The high temperature expansion breaks down for low temperatures. The numerically determined trajectory and the high temperature solution for $\phi(T)$ differ by more than 10% for temperatures $T \lesssim 50$ GeV.

Finally, we plug the solution for $\phi(T)$ into the potential to calculate the free energy

density in the high temperature approximation. This results in

$$\begin{aligned}\Delta V_{\rm HT}(T) &= V_{\rm HT}(\phi(T),0;T) - V_{\rm HT}(0,0;T) - V_{1\ \rm loop}(0,\tilde{v}_S) \\ &= \frac{1}{4}\tilde{m}_s^2\tilde{v}_S^2 - \frac{1}{16\lambda_T}\left\{M_h^2(T) + \frac{1}{6}\varepsilon_T T\left(\varepsilon_T T + \sqrt{4M_h^2(T)+\varepsilon_T^2 T^2}\right)\right\} \\ &\quad \times \left(\varepsilon_T T + \sqrt{4M_h^2(T)+\varepsilon_T^2 T^2}\right)^2 .\end{aligned} \tag{4.32}$$

Field thermal evolution with sliding behaviour

Here we lift the assumption that the broken vacuum remains at $S = 0$ for $T \leq T_c$. Instead we solve the non-trivial solutions to the minimum condition simultaneously, i.e. $\phi(T) \neq 0$ and $S(T) \neq 0$. It turns out the thermal evolution of the $\phi(T)$ field is identical to eq. (4.29), but with the following substitutions:

$$M_h^2(T) \to M_h^2(T) - a_2\tilde{v}_S^2 \qquad \text{and} \qquad \lambda_T(T) \to \lambda_T(T) - \left(\frac{a_2\tilde{v}_S}{\tilde{m}_s}\right)^2 . \tag{4.33}$$

The former substitution effectively replaces the zero temperature Higgs mass m_h in eq. (4.30) with the Higgs mass in the symmetric extremum $\tilde{m}_h$. Thus the $\phi(T)$ and $S(T)$ trajector-

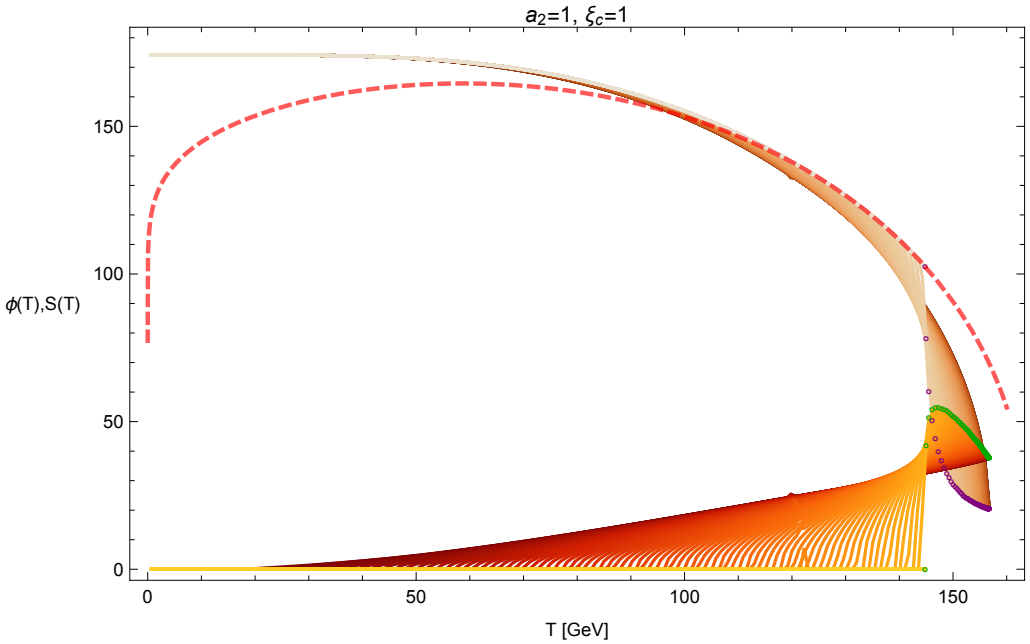

Figure 4.2: The thermal evolution of the Higgs $\phi(T)$ and singlet $S(T)$ fields in the broken vacuum between $0 < T < T_c$ (orange curves). Each orange curve represents the trajectory found for a parameter point with a unique singlet mass m_s. All parameter points have fixed strength $\xi_c = 1$ and coupling $a_2 = 1$. Darker orange trajectories correspond to lighter singlet masses, hence experience more sliding. The red dashed curve is the same high temperature solution as displayed in Figure 4.1 and coincides with the trajectory for non-sliding parameter points. The purple dashed curve is the solution for $\phi(T)$ (now describing a sliding parameter point) in eq. (4.29) but with the substitutions in eq. (4.33).

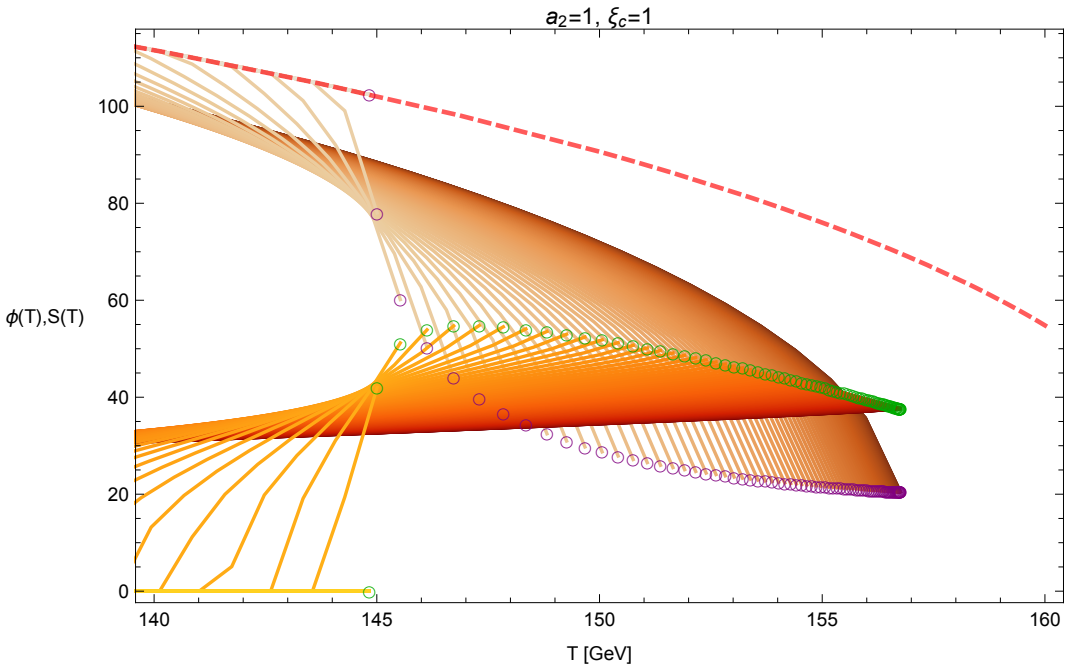

Figure 4.3: Same as Figure 4.2 but zoomed into the trajectories on the right hand side. All trajectories, except the one with lowest critical temperature, experience sliding behaviour and are highly non-trivial to calculate. Trajectories coming in at $T \sim 140$ GeV from above (below) are the Higgs $\phi(T)$ trajectories (singlet $S(T)$ trajectories). We mark out the field values at critical temperature by the purple and dark green circles for the Higgs and singlet trajectories, respectively. Refer to previous caption for further details.

ies in eq. (4.29) are no longer fixed by SM parameters. Instead they depend on a_2, m_s, and $\tilde{v}_S$. That m_h is replaced with $\tilde{m}_h$ may explain why parameter points that experience significant sliding share similar phase transition properties to the Minimal SM with free Higgs mass, as explored in Section 2.4. The only expected deviation between their phase transition properties arise from the additional singlet degrees of freedom.

We plot numerically determined solutions for $\phi(T)$ and $S(T)$ for parameter points that exhibit sliding behaviour in Figure 4.2. These solutions are found for parameter points with a fixed strength $\xi_c \equiv \sqrt{2}\, v_c/T_c = 1$ and coupling $a_2 = 1$, but variable singlet mass m_s. For each parameter point we vary the singlet mass linearly from 0 GeV $< m_s < v/\sqrt{2} =$ 123.2 GeV in increments of 1.22 GeV.

In Figure 4.2 we zoom in on the high temperature region of the trajectories, where the high temperature behaviour of sliding trajectories is clearer. We mark out the field values at critical temperature by the purple and dark green circles. The sudden jump between non-sliding to sliding endpoints shows that, without an extreme fine-tuning of the singlet mass, most sliding parameter points have a significantly weakened phase transition. This is where our notion of sliding behaviour being rapid in the $\mathbb{Z}_2$xSM comes from.

4.1.4 At thermal one loop (low temperature approximation)

We derive the expected solution for $\phi(T)$ using a low temperature expansion of the thermal effective potential. Our derivation relies on a Taylor expansion about $\phi = v$ in *both* the zero temperature potential, see eq. (4.16), and the thermal part of the potential in the low temperature approximation,

$$\Delta V_{\rm LT}(\phi;T) = -T^4 \sum_i \left\{ g_i \left(\frac{m_i\phi}{2\pi T v}\right)^{3/2} \exp\left[-\frac{m_i\phi}{Tv}\right] \left(1 + \frac{15}{8}\frac{Tv}{m_i\phi}\right)\right\}. \tag{4.34}$$

The Taylor expansion of the zero temperature potential is necessary to write the potential in a polynomial form. This is in contrast to the high temperature expansion case, which has an exact cancellation of the log terms in the zero and high temperature pieces of the potential. After the Taylor expansion, we schematically write the potential in the form

$$V_{\rm LT}(\phi;T) \approx B_0 - B_1\left(\frac{\phi}{v}\right) + \frac{1}{2}B_2\left(\frac{\phi}{v}\right)^2. \tag{4.35}$$

The coefficients are determined to be

$$B_0 = \frac{3}{4}m_h^2 v^2 - \frac{\zeta_m}{8} - \frac{1}{2}\sum_i \mathcal{V}_i \left(1 + \frac{31}{8}\frac{T}{m_i} + \frac{19}{2}\frac{T^2}{m_i^2} + \frac{45}{4}\frac{T^3}{m_i^3}\right), \tag{4.36}$$

$$B_1 = 2m_h^2 v^2 - \sum_i \mathcal{V}_i \left(1 + \frac{23}{8}\frac{T}{m_i} + \frac{45}{8}\frac{T^2}{m_i^2} + \frac{45}{8}\frac{T^3}{m_i^3}\right), \text{ and} \tag{4.37}$$

$$B_2 = 2m_h^2 v^2 - \sum_i \mathcal{V}_i \left(1 + \frac{15}{8}\frac{T}{m_i} + \frac{15}{4}\frac{T^2}{m_i^2} + \frac{15}{4}\frac{T^3}{m_i^3}\right). \tag{4.38}$$

To shorten the B_n expressions, we have identified a repeating term and denoted it by

$$\mathcal{V}_i = \frac{1}{(2\pi)^{3/2}} g_i m_i^4 \sqrt{\frac{T}{m_i}} \exp\left[-\frac{m_i}{T}\right]. \tag{4.39}$$

Minimising the expression in eq. (4.35), we find

$$\frac{\phi(T)}{v} = \frac{B_1}{B_2} = \frac{2m_h^2 v^2 - \sum_i \mathcal{V}_i \left(1 + \frac{23}{8}\frac{T}{m_i} + \frac{45}{8}\frac{T^2}{m_i^2} + \frac{45}{8}\frac{T^3}{m_i^3}\right)}{2m_h^2 v^2 - \sum_i \mathcal{V}_i \left(1 + \frac{15}{8}\frac{T}{m_i} + \frac{15}{4}\frac{T^2}{m_i^2} + \frac{15}{4}\frac{T^3}{m_i^3}\right)}. \tag{4.40}$$

This solution is represented by the blue dashed curve in Figure 4.1. Given eq. (4.40), we approximate the thermal evolution of the vacuum energy difference to be

$$\begin{aligned}\Delta V_{\rm LT}(T) &= V_{\rm LT}(\phi(T),0;T) - V_{\rm HT}(0,0;T) - V_{1\ \rm loop}(0,\tilde{v}_S) \\ &= B_0 - \frac{B_1^2}{2B_2} - V_{\rm HT}(0,0;T) + \frac{1}{4}\tilde{m}_s^2\tilde{v}_S^2 \\ &= \Delta V(0) + m_h^2 v^2 + \frac{\pi^2}{90}\left(\frac{7}{8}g_t + g_W + g_Z\right)T^4 \\ &\quad -\frac{1}{2}\left\{\sum_i \mathcal{V}_i\left(1 + \frac{31}{8}\frac{T}{m_i} + \frac{19}{2}\frac{T^2}{m_i^2} + \frac{45}{4}\frac{T^3}{m_i^3}\right) + \frac{B_1^2}{B_2}\right\}.\end{aligned} \tag{4.41}$$

As a consistency check, in the limit $T \to 0$ the term in the curly brackets goes to $2m_h^2v^2$, hence $\Delta V_{\rm LT}(T) \to \Delta V(0)$.

4.2 The strongest of phase transitions

We will denote the one loop zero temperature potential by $V(\phi, S)$ throughout the rest of this work, unless otherwise stated. An important remark about our setup is that the symmetric extremum does not move throughout the phase transition. This is because we ignore the Higgs and singlet loop contributions to the effective potential.

We choose this approach for two reasons. Firstly, we can directly compare the analytic predictions in Section 4.1 with our numerical results. Our analytic results only include the top quark and electroweak gauge bosons in one loop corrections, under the assumption that they have the most influence on the phase transition properties. Secondly, it allows for the singlet vacuum expectation value to be trivially written in terms of the zero temperature vacuum energy difference as

$$\tilde{v}_S = \frac{2}{\tilde{m}_s}\sqrt{|\Delta V(0)_{\rm SM}| - |\Delta V(0)|}. \tag{4.42}$$

Here $\Delta V(0)_{\rm SM} = -1.267 \times 10^8$ GeV^4 is the one loop zero temperature vacuum energy difference for the SM. We therefore have three free parameters at zero temperature: $\Delta V(0)$, m_s, and a_2. The quantity $\Delta V(0) \equiv V(v,0) - V(0,\tilde{v}_s)$ is useful for investigating properties of the electroweak phase transition [1, 104]. It has a strong correlation to the critical temperature, hence the strength of the phase transition. There even exists a one-to-one mapping for a certain region of this model's parameter space; we call this subspace the non-sliding region and it is described below.

4.2.1 The non-sliding parameter region

Unique to this two field model, in fixing $\Delta V(0)$ we simultaneously fix the strength of the phase transition $\xi_c \equiv \sqrt{2}\, v_c/T_c$ and the critical temperature T_c. The value of ϕ in the broken vacuum at critical temperature, v_c, and the critical temperature can be determined numerically. Recalling our chosen upper limit to a_2 from Section 4.1.1, we have the freedom to scan over $0 < a_2 \leq 10$. The singlet mass is bounded by

$$\frac{a_2}{2}\left(v^2 - v_c^2\right) < m_s^2 < \frac{a_2}{2}v^2. \tag{4.43}$$

The lower bound in eq. (4.43) prevents sliding behaviour occurring below critical temperature. Sliding behaviour describes the scenario in which the broken vacuum is destabilised along the S direction as the potential evolves from zero to critical temperature. This scenario disfavours obtaining a strong phase transition, $\xi_c \gtrsim 1$, through a tuning of $\Delta V(0)$. This does not rule out the possibility of a strong phase transition through other mechanisms[2], but it effectively does in our setup. The upper bound in eq. (4.43) ensures that $\tilde{v}_s \neq 0$ which allows us to set a value of $|\Delta V(0)|$ that is lower than the SM value.

The upper bound for the singlet mass is $\sqrt{\frac{a_2}{2}}v$ GeV. So a coupling of $a_2 \lesssim 1$ requires a singlet mass of $m_s \lesssim 123$ GeV, whereas a coupling of $a_2 \lesssim 10$ means that $m_s \lesssim 390$ GeV. In combination with the observation that $v_c \to v$ monotonically as the phase transition gets stronger, a_2 effectively sets the mass scale of the singlet for weaker phase transitions. In other words, given a_2, the weaker the phase transition the narrower the range of possible values for m_s. This effect is seen by the size of the available parameter space between the green and red curves in Figure 4.4. Each panel in Figure 4.4 has a different integer-value of the strength ξ_c and scans over the full non-sliding parameter space.

4.2.2 Symmetry breaking pattern

For our setup the symmetric extremum does not move throughout the phase transition. To determine whether the parameter point is physically realisable, we must consider the symmetry breaking pattern upon thermal evolution. As well as the critical temperature of the electroweak phase transition T_c, we must also find the critical temperature at which the broken singlet symmetry is restored, $\tilde{T}_c$. Namely we require that $\tilde{T}_c > T_c$. The analysis in ref. [97] reveals that this requirement is often satisfied, but we ought to confirm this.

A more complete treatment would involve including the Higgs and singlet in the one

[2]For example, the size of the cubic term can be increased by tree level or thermal effects.

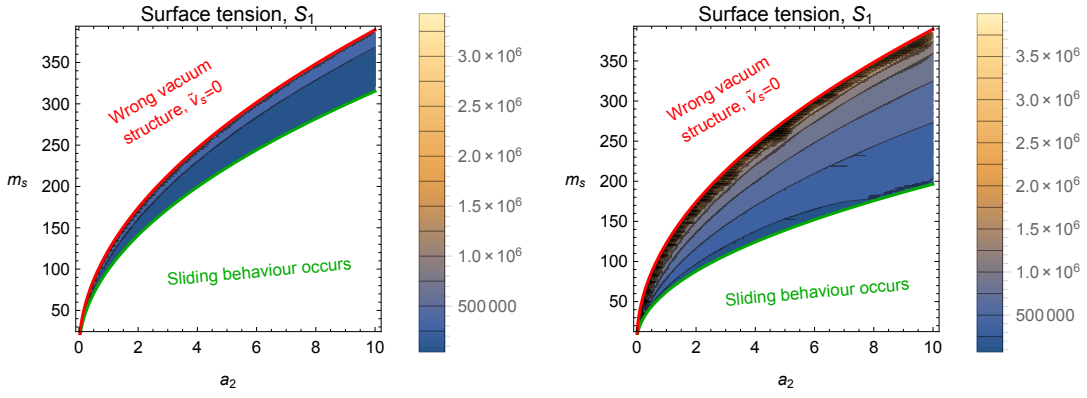

(a) Strength of $\xi_c = 1.0$

(b) Strength of $\xi_c = 2.0$

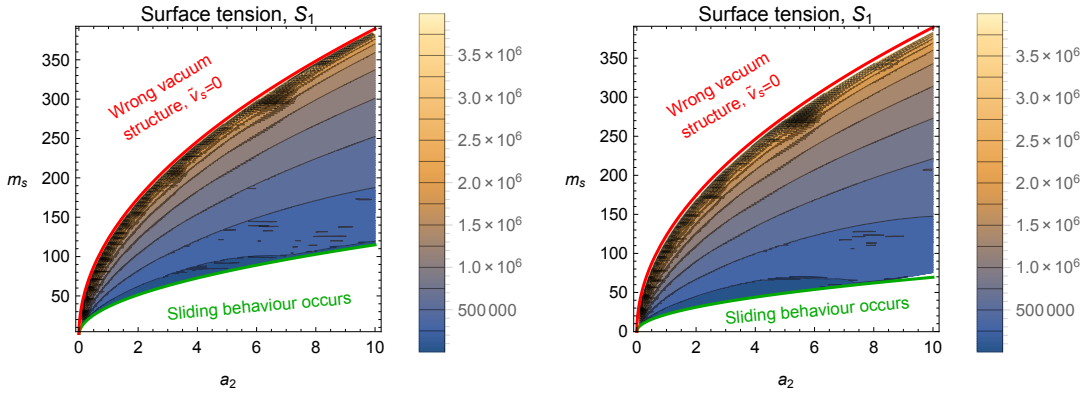

(c) Strength of $\xi_c = 3.0$

(d) Strength of $\xi_c = 4.0$

Figure 4.4: Contours of the surface tension S_1 for fixed values of the strength ξ_c. The surface tension is given in units of GeV^3. Each panel displays the singlet mass at the broken vacuum m_s (in GeV) against the Higgs-singlet mixing coupling a_2. The red and green curves illustrate the upper and lower bound of the singlet mass from eq. (4.43), respectively. Between these bounds is the non-sliding parameter subspace. It should be noted that S_1 varies significantly across each region, but the variation is smoother for stronger phase transitions.

loop (zero temperature and thermal) effective potential. This would give rise to a thermal S-dependence as well as modifying properties of the electroweak phase transition. Crucially, it allows for a restoration of the broken symmetry in the singlet direction.

Here we will determine the value of $\tilde{T}_c$ using a naive approximation. To the effective potential in the singlet direction, we add the leading order high temperature term

$$V(0,S;T) \to V(0,S;T) + \frac{1}{24}\left[\tilde{g}_h m_\phi^2(0,S) + \tilde{g}_s m_S^2(0,S)\right] T^2, \tag{4.44}$$

where $m^2_{\phi/S}(\phi,S)$ is the field-dependent squared mass in eq. (4.3) and $\tilde{g}_{h/s}$ the corresponding number of degrees of freedom of the Higgs/singlet in the symmetric extremum. Assuming the singlet symmetry is approximately a second order phase transition, we de-

termine the restoration temperature as

$$\tilde{T}_c \approx 2\sqrt{6}\left(\tilde{g}_h \frac{a_2}{\tilde{m}_s^2} + \tilde{g}_s \frac{3}{\tilde{v}_s^2}\right)^{-1/2}. \tag{4.45}$$

This will be used later in our numerical results, see Figure 4.12(c). Otherwise, we choose not to include the Higgs and singlet in the loop for the remainder of our investigation.

4.3 Phase transition properties

4.3.1 An approximation to the bounce

To find properties of the phase transition, one must find the trajectory taken in field space from one vacuum to another for a given shape (temperature) of the potential. The true trajectory is given by the bounce solution [30]. For multi-field potentials this can be non-trivial to calculate [92] so we will instead adopt the following procedure.

We will approximate the trajectory taken by the bounce as the *minimised path* between the two vacua [108]. This path is found by minimising the potential in the direction orthogonal to the direct path between the vacua. The path length from $\phi = 0$ can be treated as a new field Φ and the bounce solution found by application of the undershoot-

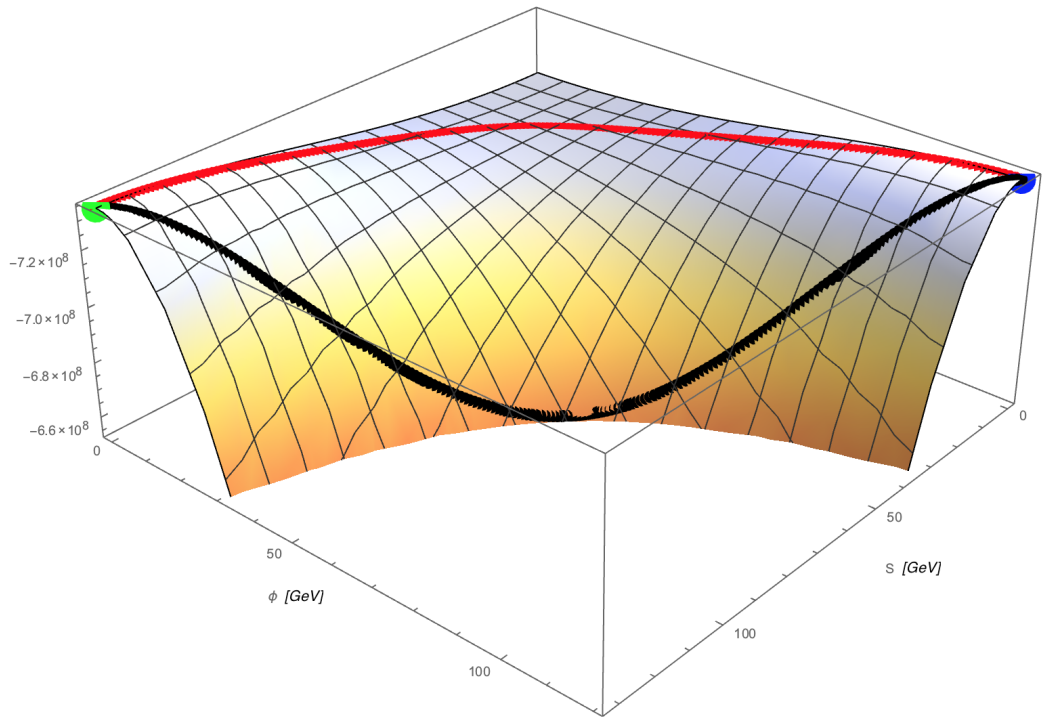

Figure 4.5: An example of an inverted two field scalar potential with both the broken (blue point) and symmetric (green point) vacua nearly degenerate. The illustration shows two paths: the direct path (black curve) and the minimised path (red curve) between the two vacua.

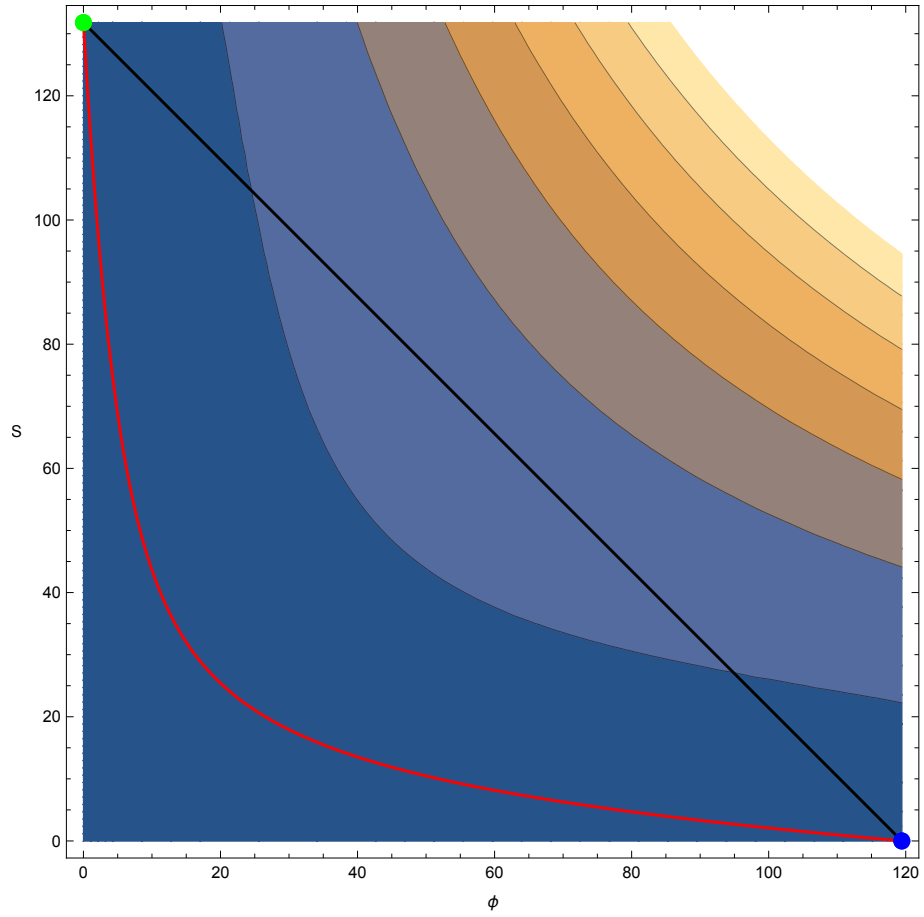

Figure 4.6: Contour plot of the potential displayed in Figure 4.5. In the above, we show the direct path (black) and minimised path (red) between the broken vacuum (blue point) and symmetric vacuum (green point). This potential is close to critical temperature T_c where the two vacua are almost degenerate. Both fields are given in units of GeV.

ing/overshooting procedure on the one field potential $V_{\text{path}}(\Phi)$. This procedure is most easily performed numerically for a given parameter point at a given temperature.

Throughout our calculations we have noticed that the shape of the potential can be highly path dependent. In extreme cases the potential along the direct path can be very different compared with the potential along the minimised path. Therefore, we must carefully define what we mean by the direct path and the minimised path. The direct path is the linear path between the symmetric and broken extrema. We then define a set of orthogonal paths. These are the family of linear paths that are orthogonal to the direct path. The minimised path is the continuous path found by minimising the potential along each of the orthogonal paths *sequentially* from the symmetric extremum to the broken vacuum.

An example parameter point at critical temperature is illustrated in Figures 4.5-4.7. Using Figure 4.5 as a visual aid, the minimised path as an approximation to the bounce path can be justified on mechanics grounds. In the upright potential the minimised path is

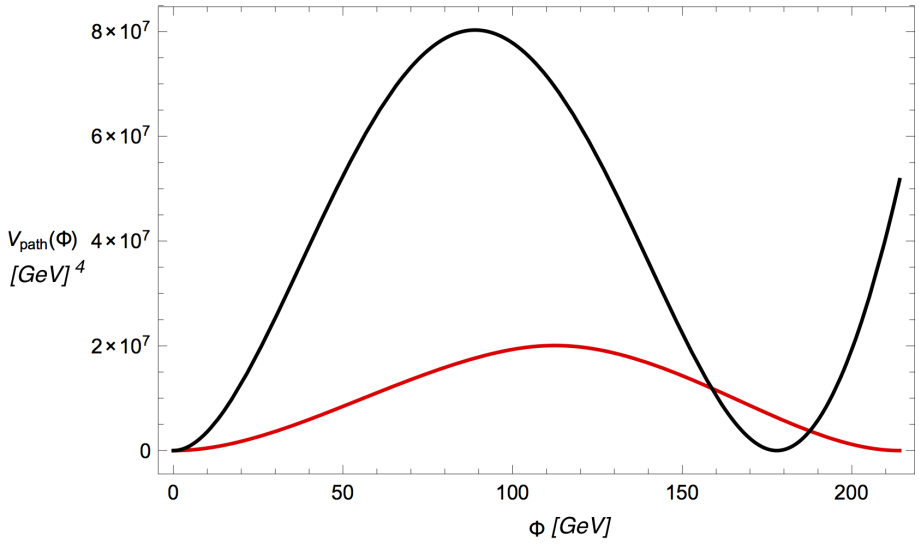

Figure 4.7: The potential along the path length Φ for the direct path (black) and minimised path (red) between the broken and symmetric vacua. This potential is close to critical temperature T_c where the two vacua are almost degenerate. Note that the broken vacuum is further for the minimised path than the direct path, because the path length Φ is longer for a curved trajectory. In this case, the barrier is widened by 23% of the distance between vacua in the direct path case.

the stable valley between two local minima. In the inverted potential the minimised path is the unstable ridge between two local maxima. Of course, the minimised path cannot be the exact trajectory taken by the true bounce. If we imagine releasing a classical particle from rest close to the broken vacuum on the minimised path, it would always fall off the ridge in the direction tangential to the minimised path. It therefore seems intuitive that the true bounce trajectory lies somewhere between the direct and minimised path. From Figure 4.7 it is clear that the size and shape of the potential barrier may change significantly between the direct and minimised path. For the rest of this work, we assume the minimum path provides an adequate approximation to the trajectory taken by the true bounce.

4.3.2 Convergence of the minimum path

Minimising the tree level potential in the S direction, see eq. (4.1), we find

$$\partial_S V_{\text{tree}} = 0 \text{ occurs at } \begin{cases} S = 0 \ \forall \ \phi, \\ S(\phi) = \pm \tilde{v}_S \sqrt{1 - \dfrac{a_2 \phi^2}{\tilde{m}_s^2}}. \end{cases} \tag{4.46}$$

We observe that the minimised path and the non-zero $S(\phi)$ path convergence within a neighbourhood of the symmetric extremum. See Figures 4.8 and 4.9 for an illustration of the $a_2 = 1$ and $a_2 = 10$ zero temperature potentials, respectively. The parameters chosen

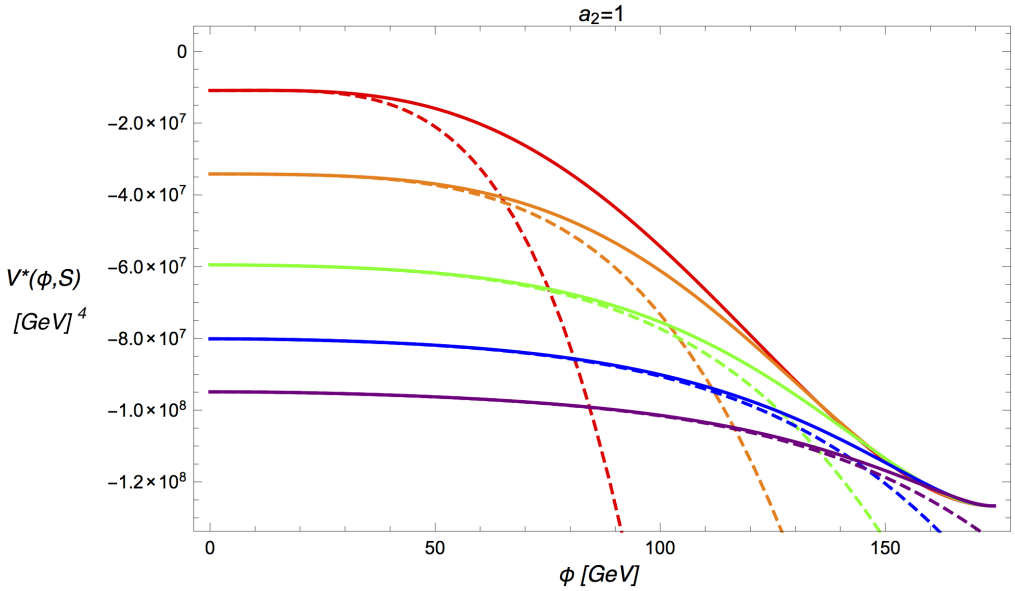

Figure 4.8: A sample of one loop effective potentials at zero temperature with the choice $a_2 = 1$. The displayed potentials $V^*(\phi, S)$ are the projections onto the $V - \phi$ plane of one of two possible trajectories in field space. The solid curves correspond to the potential along the numerically found minimised path. The dashed curves correspond to the same parameter point, but along the $S(\phi)$ path in eq. (4.46). Each colour represents a parameter point on the runaway boundary with a selected phase transition strength ξ_c. The red, orange, green, blue, and purple curves correspond to potentials with $\xi_c = 1.0, 1.5, 2.0, 2.5$, and 3.0, respectively.

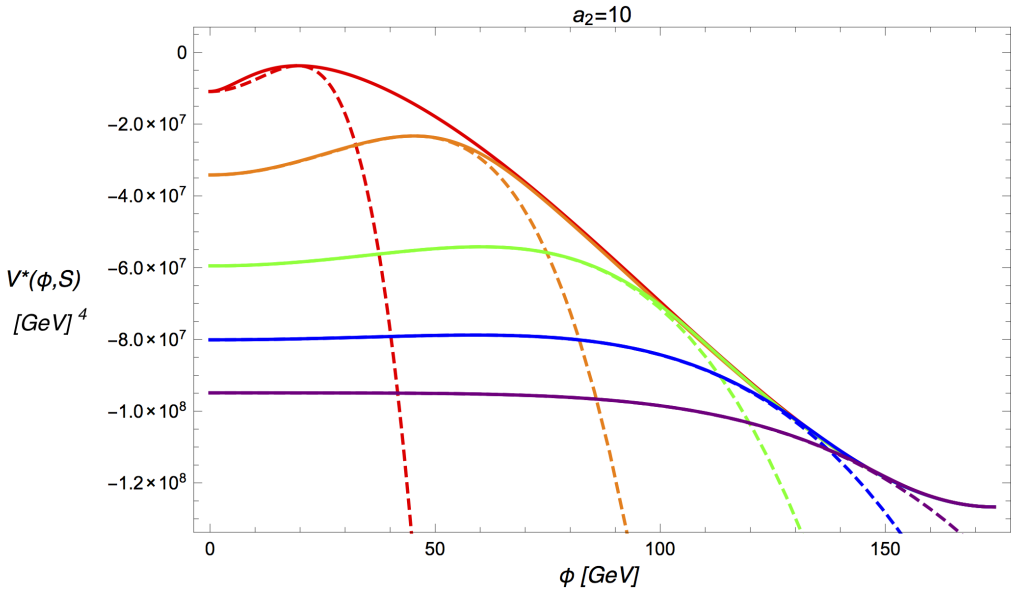

Figure 4.9: Same as Figure 4.8 but with the choice $a_2 = 10$. Note that both paths cross through the symmetric extremum and the peak barrier height. This is irrespective of the strength of the phase transition ξ_c or the size of the neighbour in which the paths converge. This is most obvious for the red coloured potentials, where the strength is $\xi_c = 1.0$.

are those on the runaway boundary, see Section 4.4 for details.

For all zero temperature potentials explored, the $S(\phi)$ path maps out the minimised path between the symmetric extremum and (if it exists) the peak barrier height very well for $\xi_c \gtrsim 1.5$. Although zero temperature barriers are more obvious for the $a_2 = 10$

potentials, there is a very small barrier peaked at $\phi \approx 10$ GeV for $\xi_c = 1.0$ and $a_2 = 1$.

In other words, $S(\phi)$ tends to be a good approximation to the minimised path in a neighbourhood of the symmetric extremum. As the strength of the phase transition ξ_c increases, the minimised path and the non-trivial path found above converge within a greater neighbourhood of the symmetric extremum. Using $S(\phi)$ as an approximation to the true bounce trajectory, this in principle allows for a quick determination of the bounce solution. This approximation is likely to be more valid for stronger phase transitions and for bubble configurations with thick bubble walls, i.e. the initial field value is further away from the broken vacuum.

Further work is required to validate this observation. Similarly, this may be developed into a useful technique for studying very strong phase transitions in a simple way. For example, we found an application for this observation when attempting to understand the potential close to the symmetric extremum in Section 4.4.3.

4.3.3 The surface tension

Let us denote the one field potential traced out by the bounce trajectory by $V_{\text{path}}(\Phi)$, where Φ is the path length of the field from the symmetric vacuum. The surface tension is defined at critical temperature by

$$S_1 = \int_0^{\Phi_c} d\Phi \sqrt{2\left[V_{\text{path}}(\Phi) - V_{\text{path}}(0)\right]}, \tag{4.47}$$

where $\Phi = \Phi_c$ ($\Phi = 0$) at the broken (symmetric) vacuum. Contour plots of the surface tension for various values of the strength ξ_c are shown in Figure 4.4. The surface tension is the one dimensional action, see Section 3.2.

4.3.4 At nucleation temperature

To find the thermal decay rate of the false vacuum, see Section 3.3, one must find a similar quantity to the surface tension S_1. This quantity is the three-dimensional Euclidean action $S_3(T)$. This action assumes a spherically static space-time solution. Assuming the probability rate of bubble production is a rapidly varying function, we estimate the nucleation temperature T_n by the condition that $S_3(T_n)/T_n = 135$. We allow for a ± 1 error to $S_3(T_n)/T_n$ when numerically determining the nucleation temperature. This definition of the nucleation temperature is expected to lead to conservative parameter regions in our numerical work, for the following reason. The decay rate at the time of nucleation can be

approximated by

$$\frac{\Gamma(T_n)}{H^4} \approx \left(\frac{T_n}{H}\right)^4 \exp\left(-\frac{S_3(T_n)}{T_n}\right) \sim 1. \tag{4.48}$$

Rearranging for $S_3(T_n)/T_n$ gives

$$\frac{S_3(T_n)}{T_n} \sim 4\log\left(\frac{2\zeta M_{\rm PL}}{T_n}\right), \tag{4.49}$$

where the Hubble parameter $H = T^2/(2\zeta M_{\rm PL})$, $\zeta \approx 1/34$, and $M_{\rm PL} = 1.22 \times 10^{19}$ GeV is the Planck mass. All parameter points in Section 4.4 have 10 GeV $< T_n <$ 135 GeV. From eq. (4.49), we would expect $155 > S_3(T_n)/T_n > 145$ for this temperature range. Therefore the actual nucleation temperature is always higher than that determined by $S_3(T_n)/T_n = 135 \pm 1$.

Definitions of bubble properties

The latent heat to radiation density ratio is defined by [19, 102, 109]

$$\alpha(T_*) \equiv \frac{1}{\rho_*}\left(-\Delta V(T_*) + \frac{1}{4}T_* \left.\frac{\partial \Delta V(T)}{\partial T}\right|_{T_*}\right), \tag{4.50}$$

where T_* is a temperature of interest and the denominator is the thermal energy density of the plasma in the symmetric phase $\rho_* = (\pi^2 g_{\rm eff} T_*^4)/30$, where $g_{\rm eff} = 108.75$ is the total number of effective degrees of freedom in the plasma. The bubble nucleation rate per Hubble volume at temperature T_* is defined as

$$\left(\frac{\beta}{H}\right)_* \equiv T_* \frac{d}{dT}\left(\frac{S_3(T)}{T}\right)\Bigg|_{T_*}. \tag{4.51}$$

Application of analytics

Here we will plug in the low and high temperature analytics, found in Sections 4.1.3 and 4.1.4, into some useful phase transition properties. For the latent heat ratio in eq. (4.50) we are interested in the free energy density

$$\Delta V_{\rm HT/LT}(T_*) \equiv \Delta V_\phi(T_*) - V_{1\text{ loop}}(0, \tilde{v}_S), \tag{4.52}$$

which in the high (low) temperature approximation is given by eq. (4.32) (eq. (4.41)). Note that the free energy density between the broken vacuum and the origin in field space, $\Delta V_\phi(T_*)$, contains all the temperature dependence. Curves for $\Delta V_\phi(T_*)$ are displayed in Figure 4.10. Using Figure 4.10 one may determine the critical temperature of the

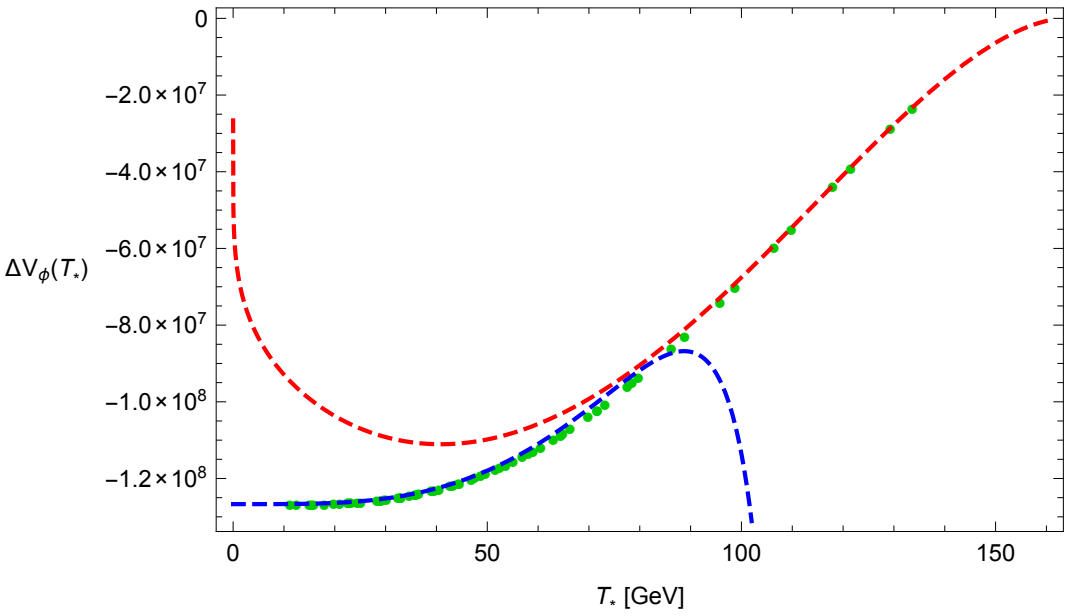

Figure 4.10: Plot showing the thermal evolution of the free energy density difference between the broken vacuum and the origin. The red and blue curves represent the analytic result in the high and low temperature expansion, respectively. The green dots are the parameter points that define the perimeter of the runaway region, displayed in Figures 4.12-4.14, for both values of a_2. The quantities plotted are $\Delta V(T_n) - \frac{1}{4}\tilde{m}_s^2\tilde{v}_S^2$ against T_n which is consistent with the definition in eq. (4.52). That these points exist between the two approximations emphasises the importance of having both a low and high temperature expansion, as well as an interpolation between them, to describe the thermal effective potential.

electroweak phase transition by solving $\Delta V_{\rm HT/LT}(T_c) = 0$, or equivalently

$$\Delta V_\phi(T_c) = -\frac{1}{4}\tilde{m}_s^2\tilde{v}_S^2 = \Delta V_{\rm SM}(0) - \Delta V(0), \tag{4.53}$$

where $\Delta V_{\rm SM}(0) = -\frac{1}{4}m_h^2 v^2 - \frac{1}{8}\zeta_m = -1.267\times10^8$ GeV^4; see condition **(2)** in Section 4.1.2. In other words, after selecting the value of $|\tilde{m}_s\tilde{v}_S|$, the critical temperature can be directly read off the plot.

The key point here is that the thermal evolution of the free energy density is the same for all non-sliding parameter points with the same strength ξ_c. This is because the thermal field evolution of $\phi(T)$ in Figure 4.1 determines the $\Delta V_\phi(T)$ trajectory and the strength $\Delta V(0)$ determines the endpoint of the trajectory T_c. Similarly, we determine the latent heat to energy density ratio at arbitrary temperature T_* to be

$$\begin{aligned}\alpha(T_*) &= \frac{1}{\rho_*}\left[-\Delta V_{\rm HT/LT}(T_*) + \frac{1}{4}T_*\frac{\partial\Delta V_{\rm HT/LT}(T)}{\partial T}\bigg|_{T_*}\right] \\ &= -\frac{1}{4}\frac{\tilde{m}_s^2\tilde{v}_S^2}{\rho_*} + \frac{1}{\rho_*}\left[-\Delta V_\phi(T_*) + \frac{1}{4}T_*\frac{\partial\Delta V_\phi(T)}{\partial T}\bigg|_{T_*}\right].\end{aligned} \tag{4.54}$$

We display the square bracketed term in the above expression using the high/low approx-

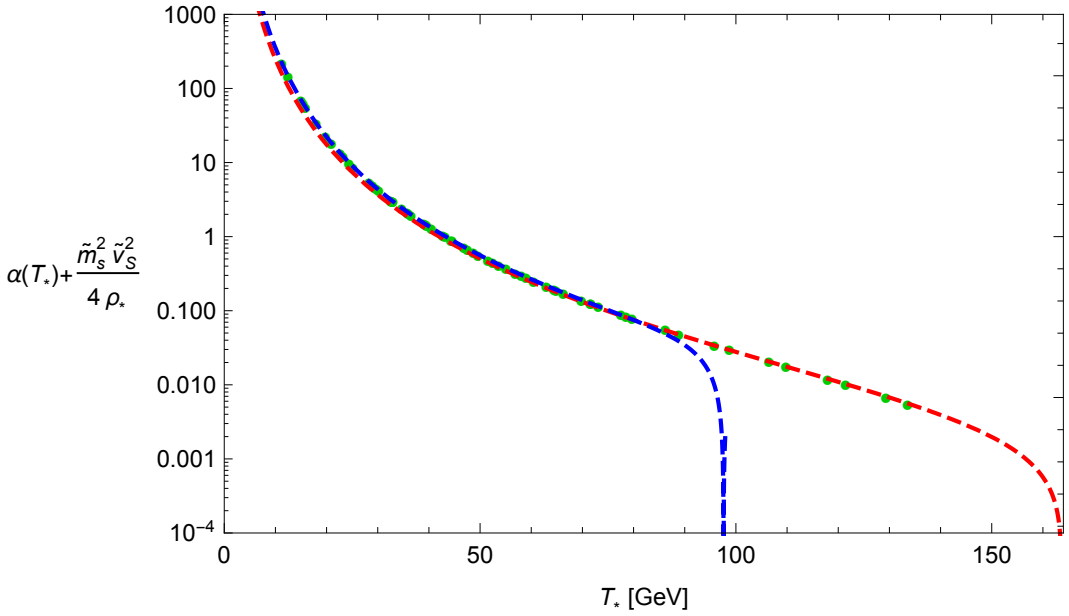

Figure 4.11: Plot showing the thermal evolution of the latent heat density to energy density ratio of the phase transition. The red and blue curves represent the analytic result in the high and low temperature expansion, respectively. The green dots are the numerically determined perimeter of the runaway region, displayed in Figures 4.12-4.14, for both values of a_2. The quantities plotted are $\alpha_n + (\frac{1}{4}\tilde{m}_s^2\tilde{v}_S^2)/\rho_n$ against T_n, where ρ_n is the normalisation factor in eq. (4.50).

imation for $\Delta V_\phi(T_*)$ in Figure 4.11. With the combination of Figures 4.10 and 4.11, one can read off the free energy density and latent heat ratio for a given value of $\frac{1}{4}\tilde{m}_s^2\tilde{v}_S^2$ (zero temperature quantity) and at any temperature T_* (thermal quantity). The difficulty arises in determining the nucleation temperature. For this reason, we must rely on a numerical analysis for the remainder of this work.

4.4 The runaway region

A physical scenario that may favour a significant production of gravitational waves is that of a very strong phase transition with runaway bubble walls [32, 110]. Runaway behaviour describes bubble walls that accelerate to ultra-relativistic speeds. In other words the bubble wall velocity $v_w \to 1$ and the corresponding Lorentz factor blows up. This is because the pressure inside the bubble exceeds that of the friction exerted on the wall by the plasma in the symmetric phase.

4.4.1 Runaway bubble walls

We use the Bödeker-Moore prescription in [31] to distinguish between runaway and non-runaway behaviour at nucleation temperature. We will use this prescription to trace out a boundary that captures the parameter space of runaway bubble scenarios. We find an

analytic form for the runaway prescription as follows. Including only the quadratic in ϕ piece of the thermal effective potential

$$V_{T\ (\text{quad})}(\phi, S) = V(\phi, S) + \frac{1}{2}\left[DT^2\right]\frac{\phi^2}{v^2}, \tag{4.55}$$

where D is the quadratic coefficient in the high temperature expansion, see eq. (4.24). The runaway criterion states that $V_{T\ (\text{quad})}(v_n, 0) \leq V_{T\ (\text{quad})}(0, \tilde{v}_S)$, whereby $v_n = \langle\phi(T_n)\rangle$ in the broken vacuum and the nucleation temperature T_n are both determined using the full thermal effective potential. Therefore, runaway bubble solutions occur if the supercooling exceeds

$$\frac{T_n}{T_c} \leq \frac{\sqrt{2}v}{v_n T_c}\sqrt{\frac{-\Delta V(0) + V(v,0) - V(v_n,0)}{D}}. \tag{4.56}$$

If the inequality in the above expression is equal, then T_n coincides with the temperature at which nucleated bubbles are expected to runaway T_{run}. It is interesting to note that bubbles could have runaway walls during a fraction of the duration between the start and end of the phase transition, whereby $T_{\text{run}} < T_n$. We assume that relatively few parameter points have such a phase transition, but they would exist close to runaway boundary. This assumption is good if the phase transition proceeds sufficiently fast. Note that as T_n decreases, v_n approaches v monotonically. So for very strong phase transitions $|V(v,0) - V(v_n,0)| \ll |\Delta V(0)|$ and eq. (4.56) simplifies to

$$\frac{T_n}{T_c} \lesssim \frac{\sqrt{2}}{T_c}\sqrt{\frac{-\Delta V(0)}{D}}. \tag{4.57}$$

The approximation in eq. (4.57) is equivalent to a runaway prescription that says "runaway occurs if the broken vacuum is lower than the symmetric vacuum in the potential $V_{T\ (\text{quad})}(\phi, S)$". Nonetheless, the prescription for distinguishing between runaway and not runaway at nucleation temperature is determined by the amount of supercooling for a given value of $\Delta V(0)$, hence corresponding strength ξ_c and critical temperature T_c.

In summary, an increasing amount of supercooling is necessary to have a runaway bubble scenario for increasingly stronger phase transitions. It then follows that phase transitions that proceed with runaway bubbles (or at least, very fast detonations) exist in the most supercooled regions of the parameter space. Parameter points with $T_n = T_{\text{run}}$ are numerically determined and displayed by the dashed curves in Figures 4.12-4.14. We refer to this as the **runaway boundary**.

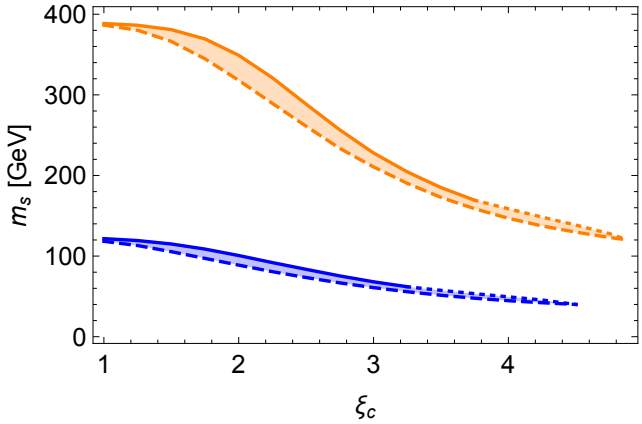

(a) Singlet mass against the strength.

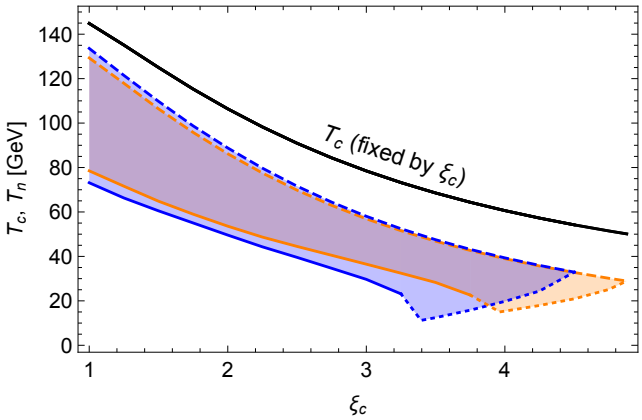

(b) Critical temperatures and nucleation temperatures against the strength.

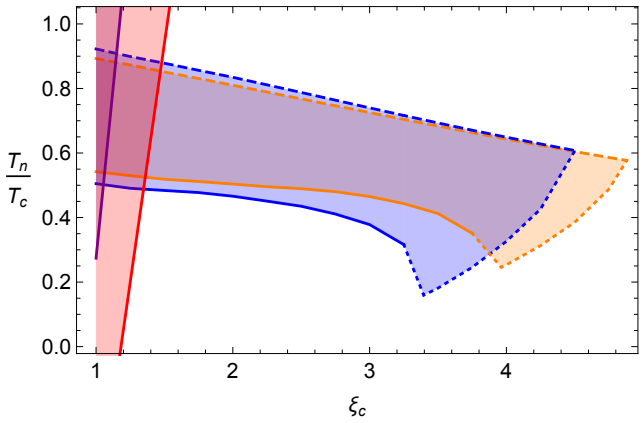

(c) Supercooling against the strength.

Figure 4.12: Plots showing the runaway region for $a_2 = 1$ (blue) and $a_2 = 10$ (orange). The runaway, stuck-in-false, and destabilisation boundaries are represented by dashed, solid, and dotted curves, respectively. All quantities are evaluated at the nucleation temperature, except the singlet mass m_s ($T = 0$) and the strength ξ_c & surface tension S_1 ($T = T_c$). The black curve in panel (b) corresponds to the critical temperature for a given strength ξ_c. The purple (red) shaded region in panel (c) corresponds to parameter points with $a_2 = 1$ ($a_2 = 10$) which are expected to have the wrong symmetry breaking pattern, according to eq. (4.45). Here we use $\tilde{g}_h = 4$ and $\tilde{g}_s = 1$.

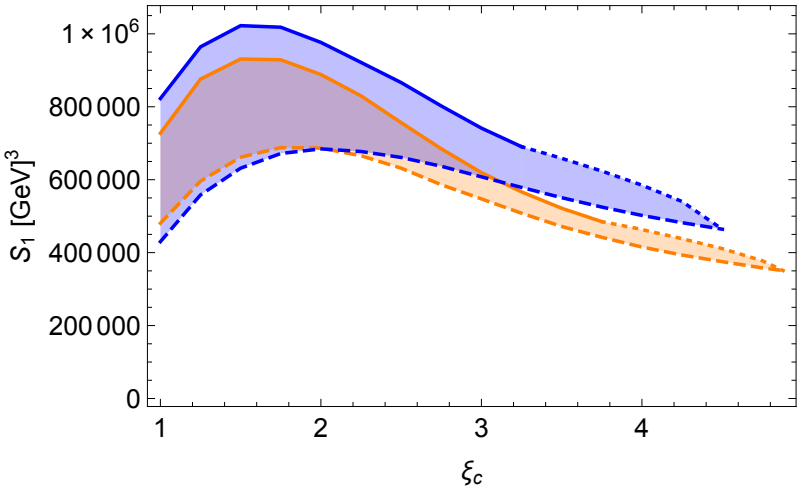

(a) Surface tension against the strength.

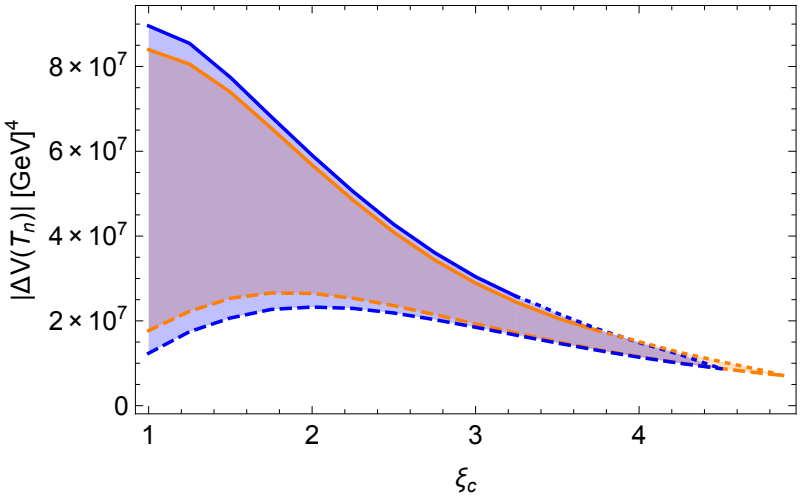

(b) Free energy density (pressure difference) against the strength.

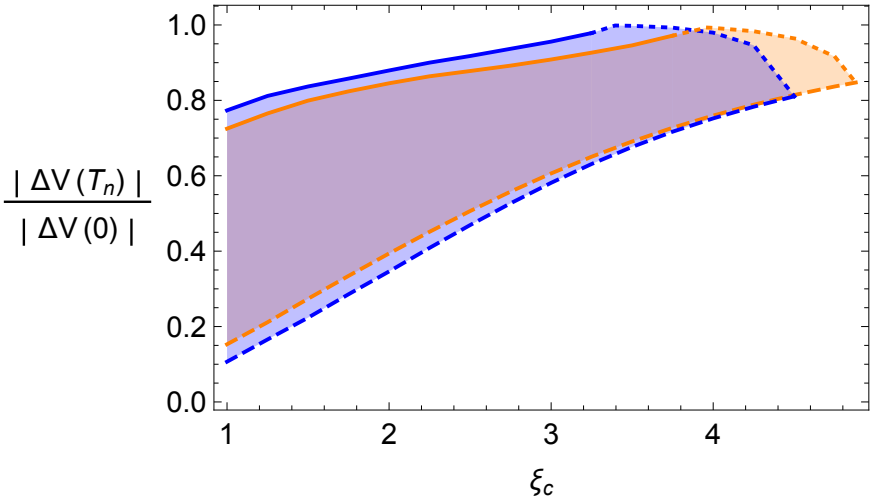

(c) Free energy density to vacuum energy ratio against the strength.

Figure 4.13: Plots displaying the runaway region, continued from previous figure. See caption in Figure 4.12 for curve colour and shading details.

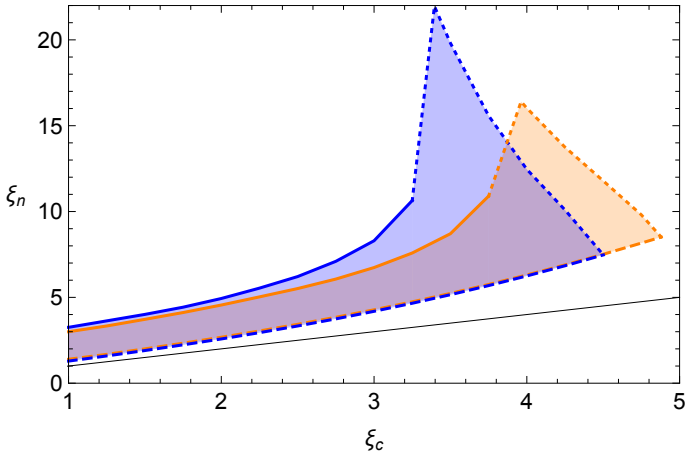

(a) Comparison of strengths at T_n and T_c.

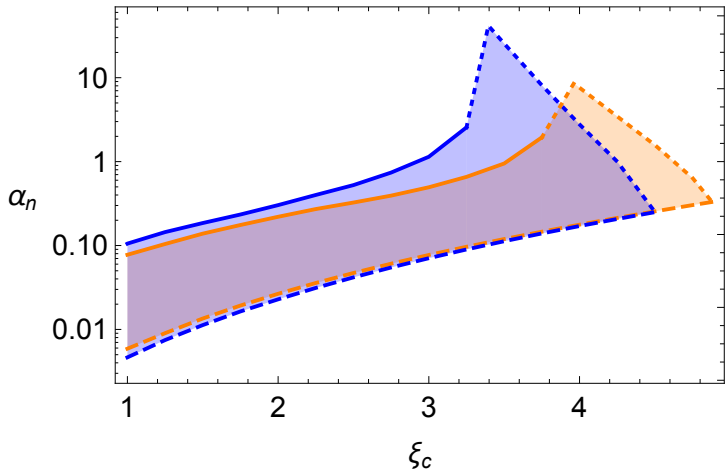

(b) Latent heat to energy density ratio against the strength.

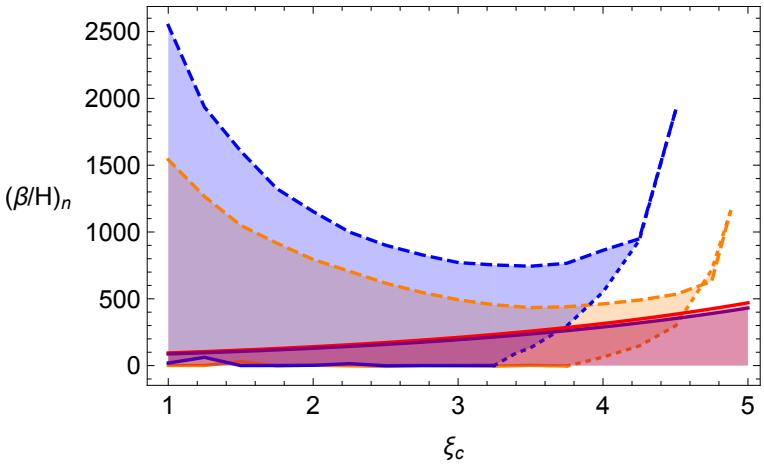

(c) Bubble nucleation rate against the strength.

Figure 4.14: Plots displaying the runaway region, continued from previous figure. See caption in Figure 4.12 for curve colour and shading details. In panel (a) we display $\xi_n = \xi_c$ by the thin black curve. The red (purple) shaded region in panel (d) corresponds to the $a_2 = 10$ ($a_2 = 1$) parameter space in which the phase transition may not complete. This is according to the criteria derived in Section 4.4.4.

4.4.2 Stuck in the false vacuum

Here we will consider the case of $T_n < T_{\rm run}$. This would result in faster bubble wall speeds at nucleation temperature, since bubble walls would have already started to runaway. To have bubbles with faster and faster wall velocities nucleating at T_n, the pressure difference $-\Delta V(T_n)$ across the wall must be increased compared with that in the $T_n = T_{\rm run}$ case. Similarly, more supercooling requires a larger surface tension. However, if too large, any nucleated bubbles will collapse under the surface tension and the phase transition will not proceed by bubble nucleation. All of these features are evident in panels (a) and (b) in Figure 4.13.

Therefore there exists a maximum surface tension which coincides with a temperature $T_{\rm stuck}$ at which we can only nucleate a few bubbles per Hubble volume. We define $T_{\rm stuck}$ by $(\beta/H)_n \approx 0$, corresponding to a minimum in $S_3(T)/T$. This is consistent with the solid curve in Figure 4.14(c). We refer to this as the **stuck-in-false boundary**.

4.4.3 Destabilisation of the symmetric vacuum

There is an important feature that occurs as we take the strength to arbitrarily large values along both the runaway and stuck-in-false boundaries. As we increase the strength ξ_c, the potential gets generically flatter as both the vacuum energy difference $|\Delta V(0)|$ and the surface tension S_1 decrease, see Figure 4.13. If the potential is too flat, thermal corrections can spontaneously break the symmetric vacuum at $T \leq T_n$. This destabilisation of the symmetric vacuum results in either the potential barrier disappearing or a second false electroweak broken vacuum emerging at $\phi \neq 0$. These are described below.

- **Case (i): Destabilisation at a temperature just below T_n, no barrier:**
  This behaviour is observed for the $a_2 = 1$ runaway boundary at $4.25 < \xi_c < 4.50$, the $a_2 = 1$ stuck-in-false boundary at $3.25 < \xi_c < 3.50$, and the $a_2 = 10$ stuck-in-false boundary at $3.75 < \xi_c < 4.00$.

  The disappearance of the barrier means that the phase transition does not proceed by bubble nucleation, despite appearing very strongly first order at critical temperature. In such a scenario, both criteria to find the runaway and stuck-in-false parameter points are ruined. The former because there is no longer a potential barrier in $V_{T\ (\rm quad)}(\phi, S)$ at $T_{\rm run}$. The latter because no minimum in $S_3(T)/T$ exists.

- **Case (ii): Destabilisation at a temperature just below T_n, barrier remains:**
  This behaviour is observed for the $a_2 = 10$ runaway boundary at $4.75 < \xi_c < 5.00$.

The phase transition can still proceed by bubble nucleation at nucleation temperature. With a $\phi \neq 0$ false vacuum, we must be careful to calculate the phase transition properties as going to the false vacuum and not to the saddle point along $\phi = 0$. This is important when calculating the strength $\xi_n \equiv \sqrt{2}\, v_n/T_n$ at nucleation temperature, the latent heat to radiation density ratio α_n, and the bubble nucleation rate $(\beta/H)_n$. We will leave the investigation of this region for further study, but note that a similar observation was made in ref. [111] for a toy two field model.

Below we calculate the temperature at which the symmetric vacuum destabilises using the thermal effective potential in the high temperature expansion, given by eq. (4.26). The temperature at which the symmetric vacuum along $\phi = 0$ becomes a maximum is determined to be

$$T_{\rm des} \leq \sqrt{\frac{-2\tilde{m}_h^2 v^2}{D}}, \tag{4.58}$$

where D is given by eq. (4.24). The above expression is sensible because we can only have the symmetric vacuum destabilise at non-zero temperature if the symmetric extremum is a saddle point at zero temperature, i.e. if $\tilde{m}_h^2 < 0$. Note that for all but the $a_2 = 10$ runaway boundary, the temperature $T_{\rm des}$ is the temperature at which the phase transition character changes from first order to second order. However, at this temperature the phase transition bubble properties cannot be calculated since no barrier exists. Therefore we must rethink our strategy.

Recall our observation in Section 4.3.2 that the stronger the phase transition, the larger the neighbourhood in which the minimised path and the $S(\phi)$ path in eq. (4.46) converge. Let us substitute the expression for $S(\phi)$ into the high temperature potential in eq. (4.26). This serves as a good approximation to the minimised path in a neighbourhood of the symmetric extremum, because we are only concerned by the potential very close to the symmetric vacuum. We will calculate phase transition properties when the nucleation temperature coincides with the temperature at which the $\phi \neq 0$ extremum is expected to be an inflex point. This temperature is determined to be

$$T_{\rm destab} \approx \sqrt{\frac{-2\tilde{m}_h^2 v^2}{D - E^2/(4\lambda_Q)}}, \tag{4.59}$$

where $\lambda_Q \approx (-\frac{1}{2}C^2 m_h^2 v^2 + \frac{3}{2}\xi_m)$ comes from Section 4.1.3. Here we ignore the temperature dependent term in the quartic coefficient, $\lambda_T(T) \approx \lambda_Q$. The quantity C^2 is defined in eq. (4.10). Compared to the temperature in eq. (4.59), the numerically determined value of $T_{\rm destab}$ is always $10^{-3} - 10^{-2}$ GeV higher. The extremum at $\phi = 0$ is always a minimum

(i.e. symmetric vacuum) at this temperature since $T_{\rm destab} > T_{\rm des}$.

The boundary in which $T_n = T_{\rm destab}$ can be traced along as the final edge of the runaway parameter region for the unbroken $\mathbb{Z}_2$xSM. We refer to this as the **destabilisation boundary**. The destabilisation boundary coincides with the runaway boundary when $T_n = T_{\rm run} = T_{\rm destab}$ and with the stuck-in-false boundary when $T_n = T_{\rm stuck} = T_{\rm destab}$. These are displayed by the dotted curves in Figures 4.12-4.14.

4.4.4 Does the phase transition complete?

A final question we must ask is whether bubbles of broken electroweak phase can saturate the surrounding universe. This is important if the phase transition is close to being stuck in the false vacuum, because the Hubble volume of symmetric vacuum could expand at a greater rate than the expansion of bubbles of broken vacuum, since the bubble nucleation rate $(\beta/H)_n$ is small. Assuming that the phase transition is very fast, we determine that any phase transition with a nucleation rate satisfying

$$\left(\frac{\beta}{H}\right)_n \gtrsim \frac{(7000\text{ GeV})}{T_n} \tag{4.60}$$

will fully saturate the Hubble volume with the broken vacuum, i.e. the phase transition completes. See Appendix D for details and a derivation. This can be regarded as the most pessimistic bound for $(\beta/H)_n$; any phase transition with a nucleation rate satisfying eq. (4.60) *will* saturate the universe with broken electroweak phase. Phase transitions with a nucleation rate that does not satisfy this bound may have a completed phase transition, but must be confirmed through a more detailed analysis.

4.4.5 Comments on the runaway region

The runaway region for $a_2 = 1$ and $a_2 = 10$ are shown in Figures 4.12-4.14 by the blue and orange shaded areas. Each of the boundaries is described above. There are a number of observations that we make.

The most obvious observation is that the value of a_2 sets the scale of the singlet mass in the runaway region, see Figures 4.12(a). A larger value of a_2 also tends to reduce $(\beta/H)_n$ along the runway boundary. Otherwise, the runaway regions map out an expanse of parameter space that does not care so much about the value of a_2.

The strength ξ_c gets rapidly stronger as the singlet mass m_s is lowered in Figure 4.12(a). We can see that the maximum strength ξ_c we can reach slightly depends on the value of a_2. With the exception of large ξ_c, the $a_2 = 1$ runaway region covers slightly more of the

parameter space of finite temperature quantities than the $a_2 = 10$ runaway region. In Figure 4.12(c), the grey region is determined by calculating $\tilde{T}_c < T_n$ along each boundary and interpolating between them. The temperature $\tilde{T}_c$ is estimated in eq. (4.45). Therefore, realising the symmetry breaking pattern is only of concern if we have a stronger a_2 coupling but just satisfy the criteria for a strong phase transition $\xi_c \sim 1$.

Generally, there is not a strong trend between the strength ξ_c and the amount of supercooling T_n/T_c. This can be seen by the fact that a point with $\xi_c = 1$ on the stuck-in-false boundary is more supercooled than a point with $\xi_c \sim 4.5$ on the runaway boundary. However, there is more supercooling for stronger phase transitions on either the runaway or stuck-in-false boundary. The nucleation temperature along the runaway boundary can be inferred from eq. (4.56). Along the stuck-in-false boundaries T_n is roughly given by

$$(T_n)_{\text{stuck}} \approx \begin{cases} (110\text{ GeV})\exp\left[-\frac{2}{5}\xi_c\right] & \text{for } a_2 = 1, \quad (\text{accurate for } T_n \gtrsim 40\text{ GeV}) \\ (120\text{ GeV})\exp\left[-\frac{2}{5}\xi_c\right] & \text{for } a_2 = 10. \quad (\text{accurate for } T_n \gtrsim 30\text{ GeV}) \end{cases} \tag{4.61}$$

There is a clear connection between the strength ξ_c and all other measures of the strength of the phase transition. This includes the strength ξ_n and the latent heat to energy density ratio of the phase transition α_n at nucleation temperature, as can be seen in panels (a) and (b) in Figure 4.14, respectively. The latter is consistent with the relation in [109] (corrected in [110]) for weaker phase transitions. Performing a numerical fit along the runaway boundary in Figure 4.14(b) we find

$$(\alpha_n)_{\text{run}} \approx (4.9 \times 10^{-3})\xi_c^2 + (3.8 \times 10^{-4})\xi_c^4. \tag{4.62}$$

For a given strength ξ_c, being on the stuck-in-false boundary can increase α_n by an order of magnitude compared to the being on runaway boundary, $(\alpha_n)_{\text{stuck}} \approx 10(\alpha_n)_{\text{run}}$.

As the strength ξ_c increases, the ratio $\Delta V(T_n)/\Delta V(0)$ increases along each boundary, see Figure 4.13(c). This does not mean that $|\Delta V(T_n)|$ increases since the increase in ξ_c is obtained by a decrease in $|\Delta V(0)|$. In fact, the functional form of $|\Delta V(T_n)|$ against ξ_c in Figure 4.13(b) is closer to the functional form of the surface tension S_1 against ξ_c in Figure 4.13(a).

We cannot go to arbitrarily strong phase transitions since the barrier vanishes, as described in Section 4.4.3. The largest strength ξ_c for a given a_2 occurs when the runaway and destabilisation boundaries coincide. This is where the dashed and dotted curves meet in Figures 4.12-4.14. Notice that the value of $(\beta/H)_n$ sharply increases at this point in

Figure 4.14(c). This is means that the value of $S_3(T)/T$ changes significantly over a small change in temperature T. This is a signature of the barrier disappearing as we approach the destabilisation boundary. To the left of this boundary we have a (strongly) first order transition, but to the right we have a second order transition. Therefore, it is sensible to suspect that the phase transition is more likely to thermally tunnel as we approach the boundary, reflected by an increase in $(\beta/H)_n$.

Assuming one finds a mechanism to prevent (or delay) the appearance of the destabilisation boundary, the further parameter space may not be physically realisable as the phase transition may not complete. This is because the required value of $(\beta/H)_n$ increases as the nucleation temperature decreases according to eq. (4.60). As the nucleation temperature decreases, the phase transition strength increases. Therefore the bound in eq. (4.60) becomes more relevant for stronger phase transitions in Figure 4.14(c).

4.5 The effective friction parameter

We will calculate an effective friction parameter η using the approach in [112]. In the rest frame of the bubble wall, the Higgs equation of motion is given by

$$\frac{d^2\Phi(\rho)}{d\rho^2} = \frac{\partial V_{\text{path}}(\Phi, T_n)}{\partial \Phi} + \eta v \frac{\Phi^2}{T_n} \frac{d\Phi(\rho)}{d\rho}, \tag{4.63}$$

where v is the bulk velocity of the fluid and Φ is our effective field. In the rest frame of the unperturbed fluid outside the bubble, the bulk velocity of the fluid is zero because the plasma is unperturbed. We will be addressing the runaway parameter region where the bubble wall is ultra-relativistic, $v_w \to 1$. In the rest frame of the bubble wall the fluid velocity would appear to *approach* the bubble wall with equal speed $v \approx v_w$. This type of bubble falls into the category of a very fast detonation. The friction parameter defined in [112] is assumed to be constant in the regime where the velocity is ultra-relativistic, i.e. $\eta(v) \to$ constant for $v \to 1$.

4.5.1 Without hydrodynamics

To avoid complications that arise from hydrodynamics, we assume that the temperature and fluid velocity are constant across the phase boundary. In which case eq. (4.63) is sufficient to describe the system. The friction parameter is determined by numerically fitting η to the solution $\Phi(\rho)$ that starts at the symmetric vacuum and ends at the broken vacuum $\Phi = \Phi_n$. Note that this solution is not the same as the bounce solution determining

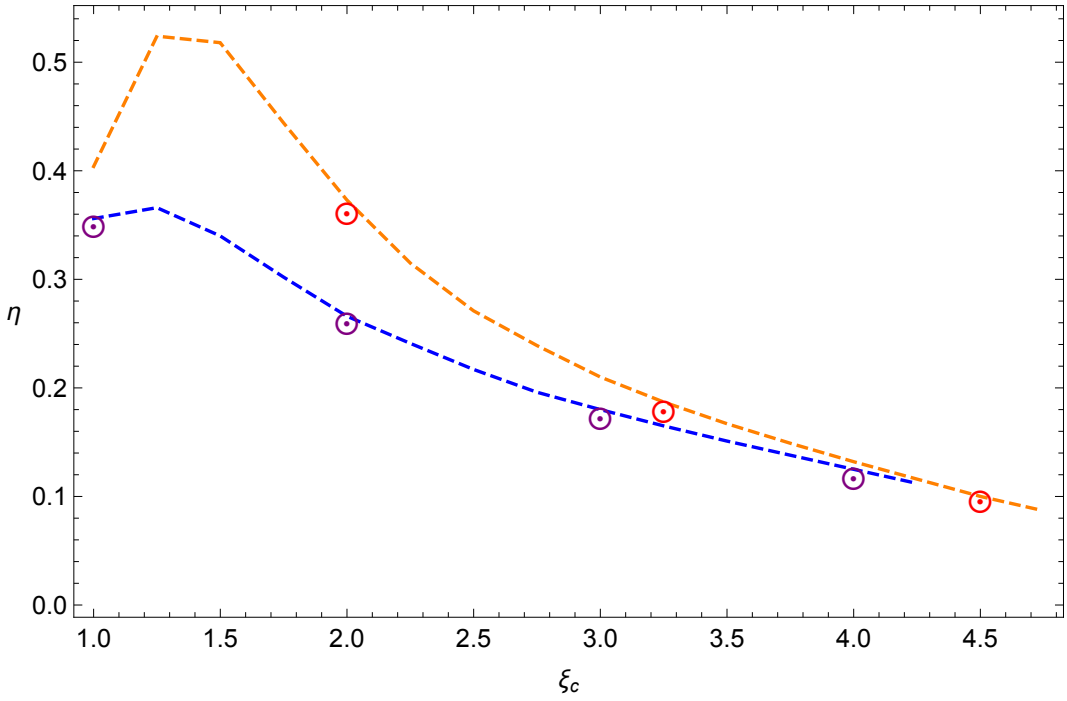

Figure 4.15: The friction parameter η calculated along runaway boundary for $a_2 = 1$ (blue) and $a_2 = 10$ (orange). The dashed curves are calculated for the case where hydrodynamic effects are ignored. Including hydrodynamics, we check a few points on the runaway boundary. These are displayed by the purple and red crosshairs for $a_2 = 1$ and $a_2 = 10$, respectively. The numerically fitted friction parameter is in relatively good agreement with and without hydrodynamics considered.

the decay of the false vacuum. Instead the field profile $\Phi(\rho)$ starts and ends at the false and true vacua, respectively.

The friction parameter is calculated for the runaway boundary and is displayed in Figure 4.15. One can see that as the strength of the phase transition ξ_c increases, we generally see a decrease in the effective friction parameter η as the strength increases. The values we find are roughly consistent with the results of Table 2 in ref. [112], though we note that their results are for subsonic bubble walls. This is supportive of the friction η being independent of the wall velocity and strictly dependent on the strength ξ_c. We also observe that the effective friction parameter is slightly higher for larger a_2, in agreement with ref. [98].

4.5.2 Including hydrodynamics

A more accurate calculation of η involves the inclusion of hydrodynamic effects. Put simply, we must solve for the field $\Phi(\rho)$, temperature $T(\rho)$, and fluid velocity $v(\rho)$ variation across the bubble wall. This requires solving eq. (4.63) along with the following set of

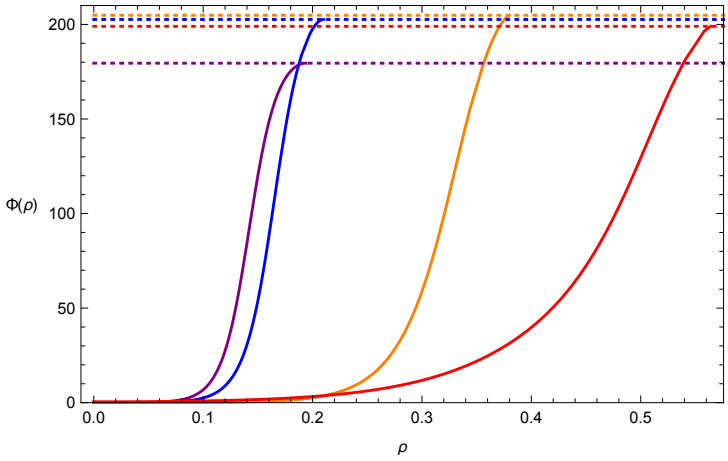

(a) The field profile $\Phi(\rho)$.

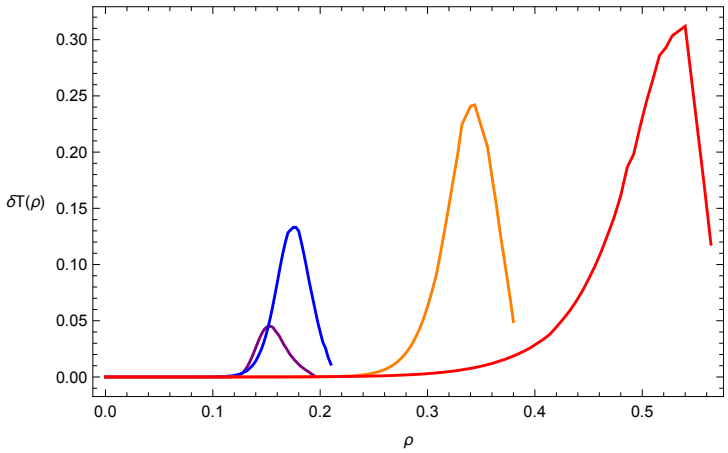

(b) The change in surrounding fluid temperature profile, $\delta T(\rho) = T(\rho) - T(0)$.

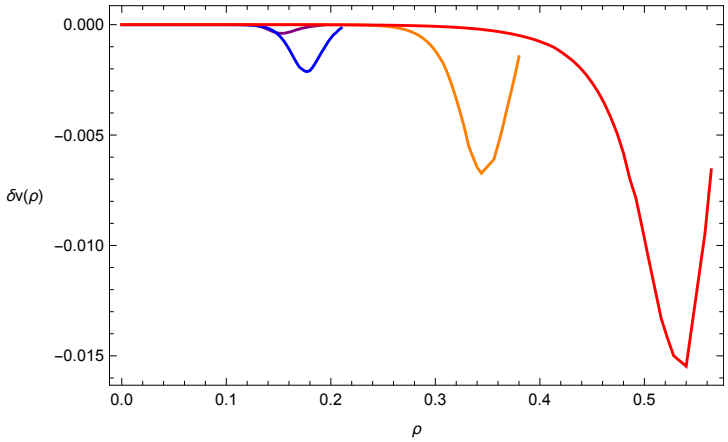

(c) The change in the unboosted fluid velocity profile $\delta v(\rho) = v(\rho) - v(0)$.

Figure 4.16: A sample of solutions with hydrodynamics included, for parameter points on the $a_2 = 1$ runaway boundary. The profiles for $\xi = 1$, 2, 3, and 4 are represented by the purple, blue, orange, and red curves, respectively. Each solution has been cut off at the point closest to the broken phase.

coupled differential equations [113]

$$\left(4aT^4 - T\frac{\partial V_{\text{path}}(\Phi,T)}{\partial T}\right)\gamma^2 v = C_1, \tag{4.64}$$

$$\left(4aT^4 - T\frac{\partial V_{\text{path}}(\Phi,T)}{\partial T}\right)\gamma^2 v^2 + aT^4 - V_{\text{path}}(\Phi,T) + \frac{1}{2}\left[\frac{d\Phi(\rho)}{d\rho}\right]^2 = C_2, \tag{4.65}$$

where C_1 and C_2 are integration constants that are determined by the initial value, the Lorentz factor is given by $\gamma = (1-v^2)^{-1/2}$, and the quantity $a = \pi^2 g_{\text{eff}}/90$. These additional differential equations derive from energy and momentum conservation across the phase boundary.

We want the bulk fluid velocity in the rest frame of the universe, i.e. in front of or far behind the bubble wall. As we have very fast detonations, the wall velocity is highly relativistic. Therefore the fluid velocity v is in a boosted frame of reference, as it appears in the above differential equations. This is reflected by our finding dramatically different solutions for $v(\rho)$ as we take the initial value of v closer to one. We can undo the boosting effect by the following relativistic transformation [112]

$$v_{\text{boosted}} \to v_{\text{unboosted}} = \frac{v_{\text{boosted}}}{1 - v^2_{\text{boosted}}}. \tag{4.66}$$

In the unboosted frame of reference, solutions for $v(\rho)$ converge as $v(0) \to 1$.

Since we are dealing with detonations, all initial values are known. In the symmetric phase, the initial values are in theory $\phi(0) = 0$, $T(0) \approx T_n$, and $v(0) = 1$. But this would lead to the field profile remaining at the symmetric vacuum for an infinite amount of time and the Lorentz factor blowing up. So we instead choose $0.002 \lesssim \phi(0) \lesssim 0.5$, $T(0) = T_n$, and $v(0) = 0.999$. By evolving the equations of motion we qualitatively expect a decrease in the bulk velocity of the fluid as it passes through the bubble wall, $v(\rho) < v(0)$, and a corresponding temperature increase of the plasma, $T(\rho) > T(0)$ [109, 114].

We find solutions to eq. (4.63)-(4.65) using a few parameter points along the runaway boundaries and, again, numerically determine the friction parameter η. For a given parameter point, we find all three profiles by numerical means using the method in Appendix E. A sample of profiles are displayed in Figure 4.16. Each coloured curve corresponds to a parameter point on the $a_2 = 1$ runaway boundary with different strength. Each solution is cut off at the value of ρ in which the field is closest to the broken VEV. The solutions for $\delta T(\rho)$ and $\delta v(\rho)$ appear to have quite a sudden cut off, because of the fine-tuning of the initial parameters required to obtain the correct solution. This is more obvious for

solutions in Figure 4.16 with higher strengths ξ_c. As the strength increases, the change in temperature and velocity across the wall also increases. Both the temperature and fluid velocity reach a peak value then drop to the original temperature.

4.6 Acoustic gravitational wave relic density

We will calculate the expected relic density of gravitational waves produced during the electroweak phase transition. Gravitational wave production is a byproduct of bubble collisions. The fine details of this process are beyond the scope of this thesis. Instead we will focus on the gravitational wave relic density predicted from α_n and $(\beta/H)_n$ in panels (b) and (c) of Figure 4.14, respectively. In the envelope approximation [17, 18], the relic density is predicted to be

$$\Omega_{\rm GW}^{\rm ea} \approx \frac{0.11 v_w^3}{0.42 + v_w^2} \left(\frac{\beta}{H}\right)_n^{-2} \frac{\kappa^2 \alpha_n^2}{(1+\alpha_n)^2}, \tag{4.67}$$

where κ is an efficiency factor that determines the fraction of latent heat density that goes into the bulk motion of the fluid. In the limit of fast bubble walls, this is given by [109]

$$\kappa \approx \frac{\alpha_n}{0.73 + 0.083\sqrt{\alpha_n} + \alpha_n}. \tag{4.68}$$

Gravitational waves produced by the standard "colliding thin shell" mechanism decay shortly after the time of production. A more durable source of gravitational waves may dominate observations in the present day [33]. These are acoustically-generated gravitational waves and have a corresponding relic density of

$$\frac{\Omega_{\rm GW}^{\rm aco}}{\Omega_{\rm GW}^{\rm ea}} \approx \frac{3(8\pi)^{1/3} \tilde{\Omega}_{\rm GW}}{0.11 v_w (0.42 + v_w^2)} \left(\frac{\beta}{H}\right)_n, \tag{4.69}$$

where $\tilde{\Omega}_{\rm GW} \approx 0.04$ is determined numerically in [102]. The relic density $\Omega_{\rm GW}^{\rm aco}$ is calculated for the runaway regions, see Figure 4.17. For our explored parameter space there is an important feature of the relic density. Namely that the relic density blows up along the stuck-in-false boundary. This results from our definition that this boundary is determined through tuning $(\beta/H)_n \approx 0$.

The relic density does, however, have an upper bound. This bound is determined by the value of $(\beta/H)_n$ such that the phase transition completes, see Section 4.4.4. A phase transition with a relic density above this upper bound may not necessarily saturate the universe with the true vacuum. Regions in which the phase transition may not complete

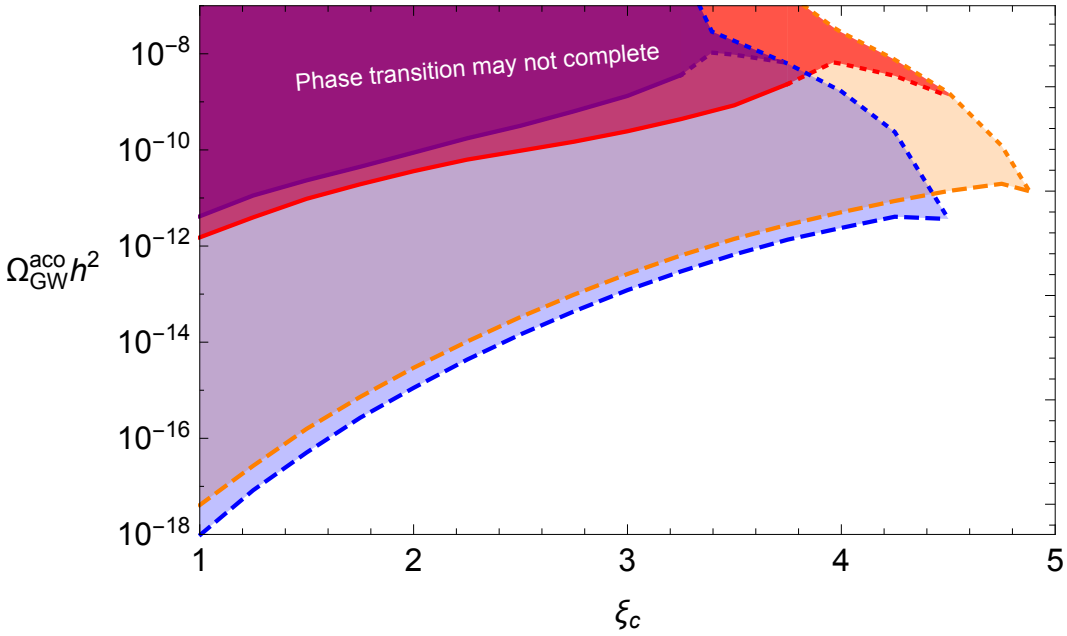

Figure 4.17: Plot of the relic density of acoustically-produced gravitation waves against the latent heat density of the phase transition. The blue (orange) area is the runaway region for $a_2 = 1$ ($a_2 = 10$). The runaway and destabilisation boundaries are represented by dashed and dotted curves, respectively. The stuck-in-false boundaries blow up $\Omega_{\rm GW}^{\rm aco}$ as a result of our definition that $(\beta/H)_n \approx 0$.

are highlighted in Figure 4.17. The boundary is calculated assuming the values of α_n and T_n of the closest boundary in Figure 4.14(c). This boundary is the stuck-in-false boundary, unless the phase transition is very strong in which it is the destabilisation boundary. This assumption overestimates the value of α_n and T_n, and so $(\beta/H)_n$ would decrease. Both an increase in α_n and a decrease in $(\beta/H)_n$ have opposite effects on $\Omega_{\rm GW}^{\rm aco}$. Therefore, we cannot say with certainty whether the calculated bound in Figure 4.17 underestimates or overestimates the size of the red/purple region compared to the accurately calculated boundary.

In summary, we have explored a region of the unbroken $\mathbb{Z}_2$xSM parameter space that corresponds to the greatest possible gravitational wave relic densities for a given strength ξ_c of the electroweak phase transition. This is the region of phase transitions with the most supercooling and the highest risk of the phase transition not completing.

4.7 Concluding remarks

We we have investigated the non-sliding parameter region of the unbroken $\mathbb{Z}_2$xSM. For smaller values of ξ_c, the mass scale of the singlet is effectively set by a_2 through $m_s \sim \sqrt{a_2/2}v$. A larger value of ξ_c allows for a broader range of singlet masses m_s, as can be seen in Figure 4.4.

We do not include the Higgs and singlet in the one loop (including thermal) corrections. Therefore the results of this study must be digested with this setup in mind. One important consideration is the symmetry breaking pattern of the phase transition. By the calculation in Section 4.2.2, we can see that most of the parameter space realises the required symmetry breaking pattern.

Our calculation of the phase transition properties rely on two assumptions. The first is that the minimised path is an adequate approximation to the trajectory taken by the true bounce solution. The second is that we define the nucleation temperature by the condition that $S_3(T)/T = 135 \pm 1$. The second assumption means that our outlined runaway region in Figures 4.12 is rather conservative, i.e. the phase transition *definitely starts* for any parameter point enclosed within the runaway region.

The runaway region is the non-sliding parameter subspace with the most supercooled phase transitions. This derives from the Bödeker-Moore prescription of runaway [31]. Both low and high temperature approximations [69] are necessary to explore the runaway region. The runaway region is bounded by the stuck-in-false-vacuum scenario, whereby no nucleated bubbles are expected to expand to fill the universe with broken electroweak phase.

In attempting to take the strength ξ_c to arbitrarily high values, we encounter an issue with the symmetric vacuum destabilising as the temperature is lowered from the critical temperature. If destabilisation occurs at a higher temperature than nucleation temperature, one of two scenarios occur. Either the phase transition does not proceed by bubble nucleation, as the barrier vanishes, or the symmetric vacuum slides to $\phi \neq 0$, breaking the electroweak symmetry. The latter scenario would proceed by bubble nucleation as usual but in a sea of "slightly" massive particles in the plasma. We only observe this scenario in Section 4.4.3 for a strong coupling, $a_2 = 10$. We note that this was previously observed in the context of a two field model [111]. This scenario was also realised for very strong phase transitions as $\Delta V(0) \to 0$ in a two Higgs doublet model, see Figure 5.8 in ref. [84]. This could make for an interesting cosmological scenario as the Higgs and singlet have a small window of mixing with a strong coupling in this false vacuum. Nonetheless, the destabilisation boundary marks out the final edge of the runaway region.

The destabilisation of the symmetric vacuum prevents one from getting arbitrarily strong phase transitions. It is worth searching for a method to remove, or delay, the appearance of the destabilisation boundary. However, the region of even stronger phase transitions comes at the risk of the phase transition not completing. This can be seen in

Figure 4.14(c).

It is our hope that the runaway regions we provide capture most of the parameter space for models driven to a very strong phase transition by $T_c \to 0$ and with a lot of supercooling. More studies into the runaway region for other models can validate this. For example, these parameter regions could be matched to the projected eLISA sensitivity curves in Figure 5 of ref. [110]. If more gravitational wave signals are discovered in the future, new physics can be extracted.

Chapter 5

Conclusion

Throughout this work we have studied aspects of the electroweak phase transition whilst only including the thermally-induced cubic terms from the electroweak gauge bosons. This was intended to explore how a strong electroweak phase transition can arise from tree level barriers and, in general, zero temperature aspects of the scalar potential.

In Chapter 2, we established a strong correlation between a zero temperature quantity and the strength of the electroweak phase transition at critical temperature. This zero temperature quantity is the vacuum energy difference between the broken and symmetric extrema. This mechanism works by monotonically lowering the critical temperature of the phase transition, whilst keeping the broken vacuum close to its zero temperature location, as the broken and symmetric extrema tend toward degeneracy at zero temperature. We found that for some models, or specific parameter regions, this allows one to tune the vacuum energy difference to get an arbitrarily strong phase transition. Parameter points that do not follow this correlation exhibit a feature that we refer to as sliding behaviour. Sliding behaviour is the scenario in which the broken vacuum destabilises, then the broken vacuum moves rapidly in field space toward the symmetric extremum. This has the effect to (sometimes significantly) weaken the strength of the phase transition.

Chapter 3 was a short technical chapter, where we discussed the formalism behind phase transitions. Most of the analytic expressions explored in Chapter 3 are not valid in Chapter 4. Nonetheless the basic concepts do still hold, so the phase transition properties in Chapter 4 are calculated numerically.

We conducted a thorough study into the non-sliding parameter region of the $\mathbb{Z}_2$xSM in Chapter 4. We further constrained ourselves to parameter regions in which the phase transition is expected to proceed by bubbles with runaway walls. Referred to as runaway regions, these have the most supercooled phase transitions for a given strength. In

attempting to take the strength to arbitrarily large values, we found that the symmetric vacuum may destabilise at a temperature just below nucleation temperature. The phase transition would initially proceed by bubble nucleation but then quickly crosses over to a second order phase transition as the barrier vanishes. Finally, we determined the range of acoustically-produced gravitational wave relic densities from runaway region phase transition properties. The highest relic densities are found to have the strongest phase transitions, the most supercooling, and the highest risk of the phase transition not completing.

There are many unanswered questions throughout this thesis, which may develop into exciting studies of the electroweak phase transition. For example, how does the non-sliding, non-runaway region compare with the non-sliding, runaway region explored in Chapter 4? We expect the non-runaway region to be bound by the same runaway boundary and a continuation of the destabilisation boundary extended up to $\xi_c = 1$. This region would appear on the opposite side of the dashed line to the runaway (shaded) region displayed in Figures 4.12 and 4.17. Similarly, we may ask what phase transition properties are attainable in the sliding parameter region? Like the spread of parameter points in Figures 2.2 and 2.4 compared to the spread in more complicated SM extensions, see Figures 2.5-2.6, perhaps the $\mathbb{Z}_2$xSM also maps out a substantial expanse of the more advanced phase transition properties, e.g. surface tension, supercooling, latent heat of the phase transition, bubble nucleation rate.

Our results emphasise the importance of the geometry of the zero temperature potential on the properties of the electroweak phase transition. Namely, the depth of the potential, discrete symmetries, and the location of the broken vacuum play a role in obtaining a very strong phase transition for any model. This enables one to understand phase transition properties through the geometrical features of a generic potential, rather than model-dependent features of a specific potential.

Bibliography

[1] Christopher P. D. Harman and Stephan J. Huber. Does zero temperature decide on the nature of the electroweak phase transition? *JHEP*, 06:005, 2016. ii, 64, 75

[2] Z. Fodor, J. Hein, K. Jansen, A. Jaster, I. Montvay, and F. Csikor. Numerical simulations and the strength of the electroweak phase transition. *Phys. Lett.*, B334:405–411, 1994. xi, 49, 50, 51

[3] Georges Aad et al. Observation of a new particle in the search for the Standard Model Higgs boson with the ATLAS detector at the LHC. *Phys.Lett.*, B716:1–29, 2012. 1, 6

[4] Serguei Chatrchyan et al. Observation of a new boson at a mass of 125 GeV with the CMS experiment at the LHC. *Phys.Lett.*, B716:30–61, 2012. 1, 6

[5] B. P. Abbott et al. Observation of Gravitational Waves from a Binary Black Hole Merger. *Phys. Rev. Lett.*, 116(6):061102, 2016. 1

[6] F. Englert and R. Brout. Broken symmetry and the mass of gauge vector mesons. *Phys. Rev. Lett.*, 13:321–323, Aug 1964. 1

[7] G. S. Guralnik, C. R. Hagen, and T. W. B. Kibble. Global conservation laws and massless particles. *Phys. Rev. Lett.*, 13:585–587, Nov 1964.

[8] Peter W. Higgs. Broken symmetries and the masses of gauge bosons. *Phys. Rev. Lett.*, 13:508–509, Oct 1964. 1

[9] Albert Einstein. Approximative Integration of the Field Equations of Gravitation. *Sitzungsber. Preuss. Akad. Wiss. Berlin (Math. Phys.)*, 1916:688–696, 1916. 1

[10] Albert Einstein. Über Gravitationswellen. *Sitzungsber. Preuss. Akad. Wiss. Berlin (Math. Phys.)*, 1918:154–167, 1918. 1

[11] The ATLAS collaboration. Search for resonances decaying to photon pairs in 3.2 fb^{-1} of pp collisions at $\sqrt{s}$ = 13 TeV with the ATLAS detector. 2015. 2

[12] CMS Collaboration. Search for new physics in high mass diphoton events in proton-proton collisions at 13TeV. 2015. 2

[13] Morad Aaboud et al. Search for resonances in diphoton events at $\sqrt{s}$=13 TeV with the ATLAS detector. *JHEP*, 09:001, 2016. 2

[14] Vardan Khachatryan et al. Search for Resonant Production of High-Mass Photon Pairs in Proton-Proton Collisions at $\sqrt{s}$ =8 and 13 TeV. *Phys. Rev. Lett.*, 117(5):051802, 2016. 2

[15] D. S. Akerib et al. Improved Limits on Scattering of Weakly Interacting Massive Particles from Reanalysis of 2013 LUX Data. *Phys. Rev. Lett.*, 116(16):161301, 2016. 2

[16] J. Billard, L. Strigari, and E. Figueroa-Feliciano. Implication of neutrino backgrounds on the reach of next generation dark matter direct detection experiments. *Phys. Rev.*, D89(2):023524, 2014. 2

[17] Arthur Kosowsky, Michael S. Turner, and Richard Watkins. Gravitational radiation from colliding vacuum bubbles. *Phys. Rev.*, D45:4514–4535, 1992. 2, 98

[18] Arthur Kosowsky and Michael S. Turner. Gravitational radiation from colliding vacuum bubbles: envelope approximation to many bubble collisions. *Phys. Rev.*, D47:4372–4391, 1993. 98

[19] Marc Kamionkowski, Arthur Kosowsky, and Michael S. Turner. Gravitational radiation from first order phase transitions. *Phys. Rev.*, D49:2837–2851, 1994. 2, 83

[20] Edward Witten. Cosmic Separation of Phases. *Phys. Rev.*, D30:272–285, 1984. 3

[21] V. A. Kuzmin, V. A. Rubakov, and M. E. Shaposhnikov. On the Anomalous Electroweak Baryon Number Nonconservation in the Early Universe. *Phys. Lett.*, B155:36, 1985. 3, 14

[22] Guy D. Moore. Measuring the broken phase sphaleron rate nonperturbatively. *Phys. Rev.*, D59:014503, 1999. 3, 14

[23] Stephan J. Huber and Thomas Konstandin. Gravitational Wave Production by Collisions: More Bubbles. *JCAP*, 0809:022, 2008. 3

[24] A. Ashoorioon and T. Konstandin. Strong electroweak phase transitions without collider traces. *JHEP*, 07:086, 2009. 6, 62

[25] Stephan J. Huber, Thomas Konstandin, Germano Nardini, and Ingo Rues. Detectable Gravitational Waves from Very Strong Phase Transitions in the General NMSSM. *JCAP*, 1603(03):036, 2016. 13

[26] Leonardo Leitao and Ariel Megevand. Gravitational waves from a very strong electroweak phase transition. *JCAP*, 1605(05):037, 2016.

[27] Ville Vaskonen. Electroweak baryogenesis and gravitational waves from a real scalar singlet. 2016. 62, 64

[28] G. C. Dorsch, S. J. Huber, T. Konstandin, and J. M. No. A Second Higgs Doublet in the Early Universe: Baryogenesis and Gravitational Waves. 2016.

[29] Mateo Garcia-Pepin and Mariano Quiros. Strong electroweak phase transition from Supersymmetric Custodial Triplets. *JHEP*, 05:177, 2016. 3

[30] Sidney Coleman. Erratum: Fate of the false vacuum: semiclassical theory. *Phys. Rev. D*, 16:1248–1248, Aug 1977. 4, 56, 57, 58, 59, 60, 78

[31] Dietrich Bodeker and Guy D. Moore. Can electroweak bubble walls run away? *JCAP*, 0905:009, 2009. 5, 63, 85, 100

[32] Andrey Katz and Antonio Riotto. Baryogenesis and Gravitational Waves from Runaway Bubble Collisions. 2016. 5, 85

[33] Mark Hindmarsh, Stephan J. Huber, Kari Rummukainen, and David J. Weir. Gravitational waves from the sound of a first order phase transition. *Phys. Rev. Lett.*, 112:041301, 2014. 5, 63, 98

[34] Stephen P. Martin. A Supersymmetry primer. 1997. [Adv. Ser. Direct. High Energy Phys.18,1(1998)]. 6, 9, 11

[35] Massimo Pietroni. The Electroweak phase transition in a nonminimal supersymmetric model. *Nucl. Phys.*, B402:27–45, 1993. 6, 10

[36] A. T. Davies, C. D. Froggatt, and R. G. Moorhouse. Electroweak baryogenesis in the next-to-minimal supersymmetric model. *Phys. Lett.*, B372:88–94, 1996.

[37] S. J. Huber and M. G. Schmidt. Electroweak baryogenesis: Concrete in a SUSY model with a gauge singlet. *Nucl. Phys.*, B606:183–230, 2001.

[38] A. Menon, D. E. Morrissey, and C. E. M. Wagner. Electroweak baryogenesis and dark matter in the nMSSM. *Phys. Rev.*, D70:035005, 2004. 10

[39] Stephan J. Huber, Thomas Konstandin, Tomislav Prokopec, and Michael G. Schmidt. Electroweak Phase Transition and Baryogenesis in the nMSSM. *Nucl.Phys.*, B757:172–196, 2006.

[40] Stephan J. Huber and Miguel Sopena. The bubble wall velocity in the minimal supersymmetric light stop scenario. *Phys. Rev.*, D85:103507, 2012.

[41] Marcela Carena, Germano Nardini, Mariano Quiros, and Carlos E. M. Wagner. The Effective Theory of the Light Stop Scenario. *JHEP*, 10:062, 2008.

[42] Weicong Huang, Zhaofeng Kang, Jing Shu, Peiwen Wu, and Jin Min Yang. New insights in the electroweak phase transition in the NMSSM. *Phys. Rev.*, D91(2):025006, 2015. 7, 10, 37

[43] Jonathan Kozaczuk, Stefano Profumo, Laurel Stephenson Haskins, and Carroll L. Wainwright. Cosmological Phase Transitions and their Properties in the NMSSM. *JHEP*, 01:144, 2015. 6, 10

[44] David E. Morrissey and Michael J. Ramsey-Musolf. Electroweak baryogenesis. *New J. Phys.*, 14:125003, 2012. 6

[45] Thomas Konstandin. Quantum Transport and Electroweak Baryogenesis. *Phys. Usp.*, 56:747–771, 2013. [Usp. Fiz. Nauk183,785(2013)]. 6

[46] Christophe Grojean, Geraldine Servant, and James D. Wells. First-order electroweak phase transition in the standard model with a low cutoff. *Phys.Rev.*, D71:036001, 2005. 6, 28

[47] Dietrich Bodeker, Lars Fromme, Stephan J. Huber, and Michael Seniuch. The Baryon asymmetry in the standard model with a low cut-off. *JHEP*, 0502:026, 2005. 28

[48] Stefano Profumo, Michael J. Ramsey-Musolf, and Gabe Shaughnessy. Singlet Higgs phenomenology and the electroweak phase transition. *JHEP*, 0708:010, 2007. 9, 18, 33

[49] Jose Ramon Espinosa and Mariano Quiros. Novel Effects in Electroweak Breaking from a Hidden Sector. *Phys.Rev.*, D76:076004, 2007.

[50] Jose R. Espinosa, Thomas Konstandin, and Francesco Riva. Strong Electroweak Phase Transitions in the Standard Model with a Singlet. *Nucl.Phys.*, B854:592–630, 2012. 33

[51] Vernon Barger, Daniel J. H. Chung, Andrew J. Long, and Lian-Tao Wang. Strongly First Order Phase Transitions Near an Enhanced Discrete Symmetry Point. *Phys. Lett.*, B710:1–7, 2012. 33

[52] G. C. Dorsch, S. J. Huber, and J. M. No. A strong electroweak phase transition in the 2HDM after LHC8. *JHEP*, 10:029, 2013. 49

[53] G. C. Dorsch, S. J. Huber, K. Mimasu, and J. M. No. Echoes of the Electroweak Phase Transition: Discovering a second Higgs doublet through $A_0 \to ZH_0$. *Phys. Rev. Lett.*, 113(21):211802, 2014.

[54] Francesco Sannino and Jussi Virkajärvi. First Order Electroweak Phase Transition from (Non)Conformal Extensions of the Standard Model. *Phys. Rev.*, D92(4):045015, 2015. 15

[55] P. H. Damgaard, A. Haarr, D. O'Connell, and A. Tranberg. Effective Field Theory and Electroweak Baryogenesis in the Singlet-Extended Standard Model. 2015. 6

[56] Daniel J. H. Chung, Andrew J. Long, and Lian-Tao Wang. 125 GeV Higgs boson and electroweak phase transition model classes. *Phys. Rev.*, D87(2):023509, 2013. 7

[57] Xin-min Zhang. Operators analysis for Higgs potential and cosmological bound on Higgs mass. *Phys. Rev.*, D47:3065–3067, 1993. 8

[58] Steven Abel and Alberto Mariotti. Novel Higgs Potentials from Gauge Mediation of Exact Scale Breaking. *Phys.Rev.*, D89(12):125018, 2014. 8

[59] Glauber C. Dorsch, Stephan J. Huber, and Jose Miguel No. Cosmological Signatures of a UV-Conformal Standard Model. *Phys.Rev.Lett.*, 113:121801, 2014. 8

[60] Marcela Carena, Germano Nardini, Mariano Quiros, and Carlos E. M. Wagner. MSSM Electroweak Baryogenesis and LHC Data. *JHEP*, 02:001, 2013. 10

[61] Ulrich Ellwanger, Cyril Hugonie, and Ana M. Teixeira. The Next-to-Minimal Supersymmetric Standard Model. *Phys.Rept.*, 496:1–77, 2010. 10, 11

[62] Graham G. Ross, Kai Schmidt-Hoberg, and Florian Staub. The Generalised NMSSM at One Loop: Fine Tuning and Phenomenology. *JHEP*, 1208:074, 2012. 10

[63] Stephan J. Huber, Thomas Konstandin, Tomislav Prokopec, and Michael G. Schmidt. Baryogenesis in the MSSM, nMSSM and NMSSM. *Nucl. Phys.*, A785:206–209, 2007. 10

[64] Hyun Min Lee, Stuart Raby, Michael Ratz, Graham G. Ross, Roland Schieren, et al. Discrete R symmetries for the MSSM and its singlet extensions. *Nucl.Phys.*, B850:1–30, 2011. 10

[65] S. A. Abel, Subir Sarkar, and P. L. White. On the cosmological domain wall problem for the minimally extended supersymmetric standard model. *Nucl. Phys.*, B454:663–684, 1995. 10

[66] Ian Jack, D.R. Timothy Jones, Stephen P. Martin, Michael T. Vaughn, and Youichi Yamada. Decoupling of the epsilon scalar mass in softly broken supersymmetry. *Phys.Rev.*, D50:5481–5483, 1994. 12

[67] L. Dolan and R. Jackiw. Symmetry Behavior at Finite Temperature. *Phys. Rev.*, D9:3320–3341, 1974. 13, 14, 27

[68] Peter Brockway Arnold and Olivier Espinosa. The Effective potential and first order phase transitions: Beyond leading-order. *Phys.Rev.*, D47:3546, 1993. 13, 50

[69] Greg W. Anderson and Lawrence J. Hall. The Electroweak phase transition and baryogenesis. *Phys.Rev.*, D45:2685–2698, 1992. 14, 47, 48, 100

[70] Stephan J. Huber. *Electroweak baryogenesis in the supersymmetric standard model with a gauge singlet.* 1999. Parallelt.: Baryogenese beim elektroschwachen Phasenübergang im supersymmetrischen Standardmodell mit Eichsingulett. - Text dt., Zsfassung in dt. u. engl. 14, 69

[71] Hiren H. Patel and Michael J. Ramsey-Musolf. Baryon Washout, Electroweak Phase Transition, and Perturbation Theory. *JHEP*, 07:029, 2011. 16

[72] Carroll Wainwright, Stefano Profumo, and Michael J. Ramsey-Musolf. Gravity Waves from a Cosmological Phase Transition: Gauge Artifacts and Daisy Resummations. *Phys. Rev.*, D84:023521, 2011.

[73] Carroll L. Wainwright, Stefano Profumo, and Michael J. Ramsey-Musolf. Phase Transitions and Gauge Artifacts in an Abelian Higgs Plus Singlet Model. *Phys. Rev.*, D86:083537, 2012. 16, 62

[74] Anders Andreassen, William Frost, and Matthew D. Schwartz. Consistent Use of Effective Potentials. *Phys. Rev.*, D91(1):016009, 2015. 16

[75] J. R. Espinosa, M. Garny, and T. Konstandin. Interplay of Infrared Divergences and Gauge-Dependence of the Effective Potential. *Phys. Rev.*, D94(5):055026, 2016. 16

[76] G. Cynolter, E. Lendvai, and G. Pocsik. Note on unitarity constraints in a model for a singlet scalar dark matter candidate. *Acta Phys. Polon.*, B36:827–832, 2005. 22, 66

[77] U. Ellwanger, Michel Rausch de Traubenberg, and Carlos A. Savoy. Phenomenology of supersymmetric models with a singlet. *Nucl.Phys.*, B492:21–50, 1997. 23, 36, 39

[78] Tania Robens and Tim Stefaniak. Status of the Higgs Singlet Extension of the Standard Model after LHC Run 1. *Eur.Phys.J.*, C75(3):104, 2015. 24

[79] D. López-Val and T. Robens. r and the W-boson mass in the singlet extension of the standard model. *Phys.Rev.*, D90(11):114018, 2014. 24

[80] Kwang Sik Jeong, Yutaro Shoji, and Masahiro Yamaguchi. Singlet-Doublet Higgs Mixing and Its Implications on the Higgs mass in the PQ-NMSSM. *JHEP*, 09:007, 2012. 24

[81] K.A. Olive et al. Review of Particle Physics. *Chin.Phys.*, C38:090001, 2014. 24

[82] Vernon Barger, Paul Langacker, Mathew McCaskey, Michael J. Ramsey-Musolf, and Gabe Shaughnessy. LHC Phenomenology of an Extended Standard Model with a Real Scalar Singlet. *Phys.Rev.*, D77:035005, 2008. 33

[83] Lars Fromme, Stephan J. Huber, and Michael Seniuch. Baryogenesis in the two-Higgs doublet model. *JHEP*, 11:038, 2006. 49

[84] Michael Seniuch. *Analysis of the phase structure in extended Higgs models.* PhD thesis, 2006. 49, 100

[85] Grzegorz Gil, Piotr Chankowski, and Maria Krawczyk. Inert Dark Matter and Strong Electroweak Phase Transition. *Phys. Lett.*, B717:396–402, 2012.

[86] Nikita Blinov, Stefano Profumo, and Tim Stefaniak. The Electroweak Phase Transition in the Inert Doublet Model. *JCAP*, 1507(07):028, 2015. 49

[87] Iason Baldes, Thomas Konstandin, and Geraldine Servant. A First-Order Electroweak Phase Transition in the Standard Model from Varying Yukawas. 2016. 50

[88] Curtis G. Callan and Sidney Coleman. Fate of the false vacuum. ii. first quantum corrections. *Phys. Rev. D*, 16:1762–1768, Sep 1977. 56, 57, 60

[89] Ian Affleck. Quantum Statistical Metastability. *Phys. Rev. Lett.*, 46:388, 1981. 60, 61

[90] Andrei D. Linde. On the Vacuum Instability and the Higgs Meson Mass. *Phys. Lett.*, B70:306–308, 1977.

[91] Andrei D. Linde. Decay of the False Vacuum at Finite Temperature. *Nucl. Phys.*, B216:421, 1983. [Erratum: Nucl. Phys.B223,544(1983)]. 57, 60, 61

[92] Thomas Konstandin and Stephan J. Huber. Numerical approach to multi dimensional phase transitions. *JCAP*, 0606:021, 2006. 56, 57, 78

[93] Hiren H. Patel and Michael J. Ramsey-Musolf. Stepping Into Electroweak Symmetry Breaking: Phase Transitions and Higgs Phenomenology. *Phys. Rev.*, D88:035013, 2013. 62

[94] Hooman Davoudiasl, Ryuichiro Kitano, Tianjun Li, and Hitoshi Murayama. The New minimal standard model. *Phys. Lett.*, B609:117–123, 2005.

[95] Jose Ramon Espinosa and Mariano Quiros. Novel Effects in Electroweak Breaking from a Hidden Sector. *Phys. Rev.*, D76:076004, 2007. 64

[96] Vernon Barger, Daniel J. H. Chung, Andrew J. Long, and Lian-Tao Wang. Strongly First Order Phase Transitions Near an Enhanced Discrete Symmetry Point. *Phys. Lett.*, B710:1–7, 2012. 64

[97] James M. Cline and Kimmo Kainulainen. Electroweak baryogenesis and dark matter from a singlet Higgs. *JCAP*, 1301:012, 2013. 76

[98] Jonathan Kozaczuk. Bubble Expansion and the Viability of Singlet-Driven Electroweak Baryogenesis. *JHEP*, 10:135, 2015. 66, 95

[99] Jose R. Espinosa, Thomas Konstandin, and Francesco Riva. Strong Electroweak Phase Transitions in the Standard Model with a Singlet. *Nucl. Phys.*, B854:592–630, 2012. 63, 64

[100] David Curtin, Patrick Meade, and Chiu-Tien Yu. Testing Electroweak Baryogenesis with Future Colliders. *JHEP*, 11:127, 2014. 66

[101] Michael J. Baker and Joachim Kopp. The Vev Flip-Flop: Dark Matter Decay between Weak Scale Phase Transitions. 2016. 62

[102] Mark Hindmarsh, Stephan J. Huber, Kari Rummukainen, and David J. Weir. Numerical simulations of acoustically generated gravitational waves at a first order phase transition. *Phys. Rev.*, D92(12):123009, 2015. 63, 83, 98

[103] Stefano Profumo, Michael J. Ramsey-Musolf, and Gabe Shaughnessy. Singlet Higgs phenomenology and the electroweak phase transition. *JHEP*, 08:010, 2007. 64

[104] Weicong Huang, Zhaofeng Kang, Jing Shu, Peiwen Wu, and Jin Min Yang. New insights in the electroweak phase transition in the NMSSM. *Phys. Rev.*, D91(2):025006, 2015. 64, 75

[105] Sidney R. Coleman and Erick J. Weinberg. Radiative Corrections as the Origin of Spontaneous Symmetry Breaking. *Phys. Rev.*, D7:1888–1910, 1973. 67

[106] L. Dolan and R. Jackiw. Symmetry Behavior at Finite Temperature. *Phys. Rev.*, D9:3320–3341, 1974. 69

[107] Greg W. Anderson and Lawrence J. Hall. Electroweak phase transition and baryogenesis. *Phys. Rev. D*, 45:2685–2698, Apr 1992. 69

[108] Daniel J. H. Chung and Andrew J. Long. Cosmological Constant, Dark Matter, and Electroweak Phase Transition. *Phys. Rev.*, D84:103513, 2011. 78

[109] Jose R. Espinosa, Thomas Konstandin, Jose M. No, and Geraldine Servant. Energy Budget of Cosmological First-order Phase Transitions. *JCAP*, 1006:028, 2010. 83, 93, 97, 98

[110] Chiara Caprini et al. Science with the space-based interferometer eLISA. II: Gravitational waves from cosmological phase transitions. *JCAP*, 1604(04):001, 2016. 85, 93, 101

[111] David Land and Eric D. Carlson. Two stage phase transition in two Higgs models. *Phys. Lett.*, B292:107–112, 1992. 91, 100

[112] Stephan J. Huber and Miguel Sopena. An efficient approach to electroweak bubble velocities. 2013. 94, 95, 97

[113] J. Ignatius, K. Kajantie, H. Kurki-Suonio, and M. Laine. The growth of bubbles in cosmological phase transitions. *Phys. Rev.*, D49:3854–3868, 1994. 97

[114] M. Gyulassy, K. Kajantie, H. Kurki-Suonio, and Larry D. McLerran. Deflagrations and Detonations as a Mechanism of Hadron Bubble Growth in Supercooled Quark Gluon Plasma. *Nucl. Phys.*, B237:477–501, 1984. 97

[115] José M. No Redondo. Aspects of phenomenology and cosmology in hidden sector extensions of the standard model. 2009. 118

Appendix A

Parameter space scan (xSM)

Throughout the numerical scan, the ($\mathbb{Z}_2$)xSM parameters are assigned random values following the below table. These parameters are chosen through linear distributions. For our numerical scan, the mass scale is chosen to be $M = 1$ TeV.

Parameter:	Mass dimension, n:	Minimum:	Maximum:	Determined:
λ_0	0	$m_{\phi_1}^2/(4v^2)$	$m_{\phi_2}^2/(4v^2)$	Random assignment
v_S	0	$-M$	0	Random assignment
$\lvert a_1\rvert$	1	0	M	Random assignment
$\lvert b_3\rvert$	1	0	M	Random assignment
m_s	1	0	M	Random assignment
$\lvert a_2\rvert$	0	0	10	Reparameterisation
b_4	0	0	10	Reparameterisation
μ	1	–	–	Minimum condition
b_2	2	–	–	Minimum condition
m_h	1	125	125	Fixed

Table A.1: Table of real values randomly assigned to each ($\mathbb{Z}_2$)xSM parameter throughout the numerical scan. The dimension column is given in units of mass dimension, i.e. $[M]^n$. The final column labels how the numerical value is determined.

Appendix B

Parameter space scan (GNMSSM)

Throughout the numerical scan, the parameters are assigned with a natural description for the GNMSSM at low energy scales. This implies that the GNMSSM may easily be described via a top-down approach with a low enough supersymmetry breaking scale, so as to not demand a huge fine-tuning of the parameters. Therefore, we choose $m_{\text{SUSY}} = 1$ TeV for our numerical scan. All parameters are randomly chosen through linear distributions, except for $|\lambda|$ and $|k_3|$ which are determined through $\log_{10}$ distributions.

Parameter:	Mass dimension, n:	Minimum:	Maximum:	Determined:
$\tan\beta$	0	1	10	Random assignment
$\lvert\lambda\rvert$	0	1.0×10^{-3}	0.7	Random assignment
v_S	1	-250	0	Random assignment
$\lvert\mu\rvert$	1	0	m_{SUSY}	Random assignment
$\lvert k_1\rvert$	2	0	m^2_{SUSY}	Random assignment
$\lvert k_2\rvert$	1	0	m_{SUSY}	Random assignment
$\lvert k_3\rvert$	0	1.0×10^{-3}	0.7	Random assignment
$\lvert b\mu\rvert$	1	0	m^2_{SUSY}	Random assignment
$\lvert k_2 A_{k_2}\rvert$	1	0	m^2_{SUSY}	Random assignment
$\lvert k_3 A_{k_3}\rvert$	1	0	m_{SUSY}	Random assignment
$\lvert\lambda A_\lambda\rvert$	1	0	m_{SUSY}	Random assignment *
m_{Q_3}	1	Δm_3	m_{SUSY}	Fixed for m_h
$m_{\bar{u}_3}$	1	–	–	Fixed
Δm_3	1	100	100	Fixed
A_t	1	–	–	Fixed
m_{h^0}	1	125	125	Fixed
m_{H_u}	1	–	–	Minimum condition
m_{H_d}	1	–	–	Minimum condition
m_S	1	–	–	Minimum condition
$\lvert A_{k_1}\rvert$	1	0	m_{SUSY}	No linear term in S

Table B.1: Table of real values randomly assigned to each GNMSSM parameter throughout the numerical scan. The dimension column is given in units of mass dimension, i.e. $[M]^n$. The final column labels how the numerical value is determined.
*Note that the A_λ parameter is randomly assigned subject to the broken vacuum being the absolute minimum of the one loop effective potential.

Appendix C

GNMSSM benchmarks: parameter points

The assigned parameter values for each of the benchmark scenarios is provided in the table below.

Parameter:	Benchmark I:	Benchmark II:	Benchmark III:
$\tan\beta$	1.350	2.355	5.133
λ	0.5770	0.5690	0.6266
v_S [GeV]	-110.1	-161.5	-146.7
μ [GeV]	463.7	275.5	278.6
k_1 [GeV]^2	-6.820×10^5	-7.547×10^5	8.624×10^5
k_2 [GeV]	-303.7	367.8	529.2
k_3	-0.1513	0.2804	-0.2508
$b\mu$ [GeV]^2	7.843×10^5	7.621×10^5	8.057×10^5
$k_2 A_{k_2}$ [GeV]^2	-6.072×10^5	3.440×10^4	-2.065×10^5
$k_3 A_{k_3}$ [GeV]	-124.5	-233.8	456.6
λA_λ [GeV]	641.1	130.4	265.2
m_{Q_3} [GeV]	688.8	926.7	991.7

Table C.1: Table of values assigned to each of the considered GNMSSM benchmark scenarios.

Appendix D

Bubble nucleation rate approximation for a completed phase transition

Let us define $S(T) \equiv S_3(T)/T$ and $B(T) \equiv \beta(T)/H(T)$, such that

$$\frac{\beta(T)}{H(T)} = T\frac{\partial S_3(T)}{\partial T} \rightarrow S'(T) = \frac{B(T)}{T}. \tag{D.1}$$

Taylor expanding $B(T)$ about $T = T_*$, we have

$$S'(T) = \frac{B(T_*)}{T} + \left(1 - \frac{T_*}{T}\right)\left.\frac{\partial B(T)}{\partial T}\right|_{T_*} + ... + \frac{1}{n!}\left(1 - \frac{T_*}{T}\right)^n T^{(n-1)}\left.\frac{\partial^n B(T)}{\partial T^n}\right|_{T_*}. \tag{D.2}$$

Integrating this expression from T_* to T

$$\begin{aligned} S(T) = \int_{T_*}^{T} d\tilde{T}\left[S'(\tilde{T})\right] = \; & S(T_*) + \left(B(T_*) - T_*B'(T_*) + \frac{1}{2}T_*^2B''(T_*) + ...\right)\log\left(\frac{T}{T_*}\right) \\ & + \left(-T_*B'(T_*) + \frac{1}{2}T_*^2B''(T_*) + ...\right)\left(1 - \frac{T}{T_*}\right) \\ & + \left(\frac{1}{2}T_*^2B''(T_*) + ...\right)\frac{1}{2}\left(1 - \frac{T}{T_*}\right)^2 + \mathcal{O}\left(1 - \frac{T}{T_*}\right)^3. \end{aligned} \tag{D.3}$$

Henceforth, we will use the shorthand notation that any quantity $F(T)$ evaluated at $T = T_*$ is denoted by $F(T_*) = F_*$. We can rewrite the above expression as

$$\begin{aligned} S(T) = \; & S_* + \left(B_* + B_*^{(1)} + B_*^{(2)} + ... + B_*^{(k)}\right) \log\left(\frac{T}{T_*}\right) \\ & + \left(B_*^{(1)} + B_*^{(2)} + B_*^{(3)} + ... + B_*^{(k)}\right)\left(1 - \frac{T}{T_*}\right) \\ & + \frac{1}{2}\left(B_*^{(2)} + B_*^{(3)} + ... + B_*^{(k)}\right)\left(1 - \frac{T}{T_*}\right)^2 + \mathcal{O}\left(1 - \frac{T}{T_*}\right)^3, \end{aligned} \tag{D.4}$$

where

$$B_*^{(k)} \equiv \frac{(-1)^k}{k!} T_*^k \left.\frac{\partial^k B(T)}{\partial T^k}\right|_{T_*}. \tag{D.5}$$

Thus we have

$$e^{-S(T)} \approx e^{-S_*}\left(\frac{T_*}{T}\right)^{(B_*+B_1)}\left[1 - B_1\left(1 - \frac{T}{T_*}\right) + \frac{1}{2}\left(B_1^2 - B_2\right)\left(1 - \frac{T}{T_*}\right)^2\right], \tag{D.6}$$

$$\text{where } B_1 = \sum_{i=1}^{k} B_*^{(i)} \text{ and } B_2 = \sum_{i=2}^{k} B_*^{(i)}.$$

The value of k is the power of $(1 - T_*/T)$ at which the original Taylor expansion in eq. (D.2) is truncated. For the simplest approximation, we assume that $B(T)$ is constant with respect to temperature. More specifically that $B(T) \approx B_n$ is constant between the nucleation and finalisation temperature of the phase transition. This should be valid for very fast phase transitions where both the nucleation and finalisation temperatures are far away from temperatures where $B(T)$ blows up[1], i.e. $B_n^{(0)} \gg B_n^{(k)}$ for all $k > 0$.

This expression can be plugged into the expected volume of bubbles normalised to the Hubble volume, $f(T)$. The finalisation temperature of the phase transition T_f is defined at when the Hubble volume is saturated with broken electroweak phase $f(T_f) = 1$ [115].

$$f(T_f) = \frac{4\pi v_w^3}{3}(2\zeta M_{\rm PL})^4 \int_{T_f}^{T_n} dT \left[\frac{1}{T^5} e^{-S(T)}\left(1 - \frac{T^2}{T_n^2}\right)^3\right]. \tag{D.7}$$

This expression assumes all bubbles nucleate at nucleation temperature and we ignore the excess volume from overlapping bubbles. The resulting finalisation temperature is therefore an overestimate. Noting that

$$\left(1 - \frac{T^2}{T_n^2}\right)^3 = 1 - 3\frac{T^2}{T_n^2} + 3\frac{T^4}{T_n^4} - \frac{T^6}{T_n^6}, \tag{D.8}$$

[1]For example, $B(T) \to \infty$ as $T \to T_c$ and, if a barrier exists at zero temperature, $B(T) \to \infty$ as $T \to 0$.

we can solve the integral in eq. (D.7) to find

$$f(T_f) = \frac{4\pi v_w^3}{3}(2\zeta M_{\rm PL})^4 e^{-S_n}(T_n)^{B_n}\left[-\frac{T^{-B_n-4}}{B_n+4}+\frac{3}{T_n^2}\frac{T^{-B_n-2}}{B_n+2}-\frac{3}{T_n^4}\frac{T^{-B_n}}{B_n}+\frac{1}{T_n^6}\frac{T^{-B_n+2}}{B_n-2}\right]_{T_f}^{T_n}$$

$$f(T_f) = \frac{4\pi v_w^3}{3}\left(\frac{2\zeta M_{\rm PL}}{T_n}\right)^4 e^{-S_n}\left\{\frac{48}{(B_n+4)(B_n+2)B_n(B_n-2)}\right.$$
$$\left.-\left(\frac{T_f}{T_n}\right)^{-(B_n+4)}\left[-\frac{1}{B_n+4}+\frac{3}{B_n+2}\left(\frac{T_f}{T_n}\right)^2-\frac{3}{B_n}\left(\frac{T_f}{T_n}\right)^4+\frac{1}{B_n-2}\left(\frac{T_f}{T_n}\right)^6\right]\right\} \tag{D.9}$$

Recall that $B_n \equiv (\beta/H)_n$ is the bubble nucleation rate at nucleation temperature. Applying the condition that $f(T_f) = 1$ to eq. (D.9), we determine a lower bound for $(\beta/H)_n$. We also assume $v_w \approx 1$, $\zeta \approx 1/34$, $S_n \approx 135$, and $M_{\rm PL} = 1.22\times10^{19}$ GeV. This lower bound is necessary to have a phase transition that completes, i.e. saturates the universe with broken phase. This is achieved by finding numerical solutions for $(\beta/H)_n$ against T_n with fixed T_f/T_n, and $(\beta/H)_n$ against T_f/T_n with fixed T_n. Both are plotted in Figures D.1-D.2.

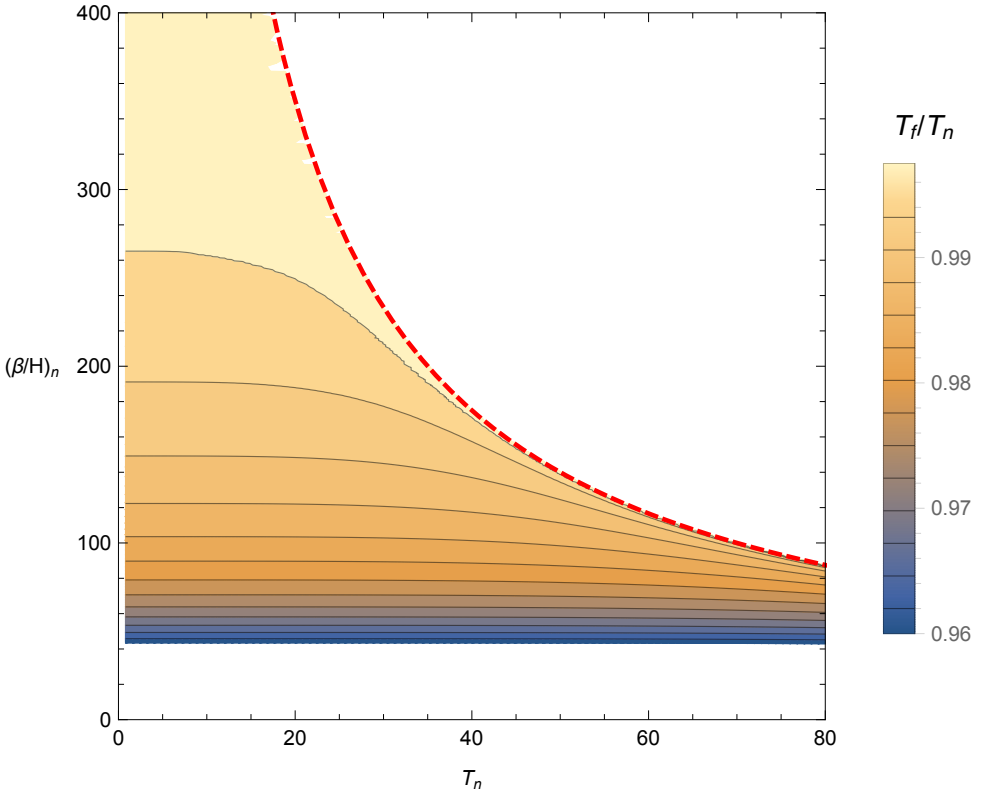

Figure D.1: Contour plot of the lower bound of the bubble nucleation rate $(\beta/H)_n$ against the nucleation temperature T_n. The contours represent a fixed value of T_f/T_n in accordance with the legend. For not-so-fast phase transitions, $T_f/T_n \lesssim 0.98$, the value of $(\beta/H)_n$ is approximately constant in T_n. However, our assumption that $B(T)$ is constant around T_n is mostly likely valid if $T_f/T_n \to 1$. This solution is given by eq. (D.10) and is displayed by the red, dashed curve.

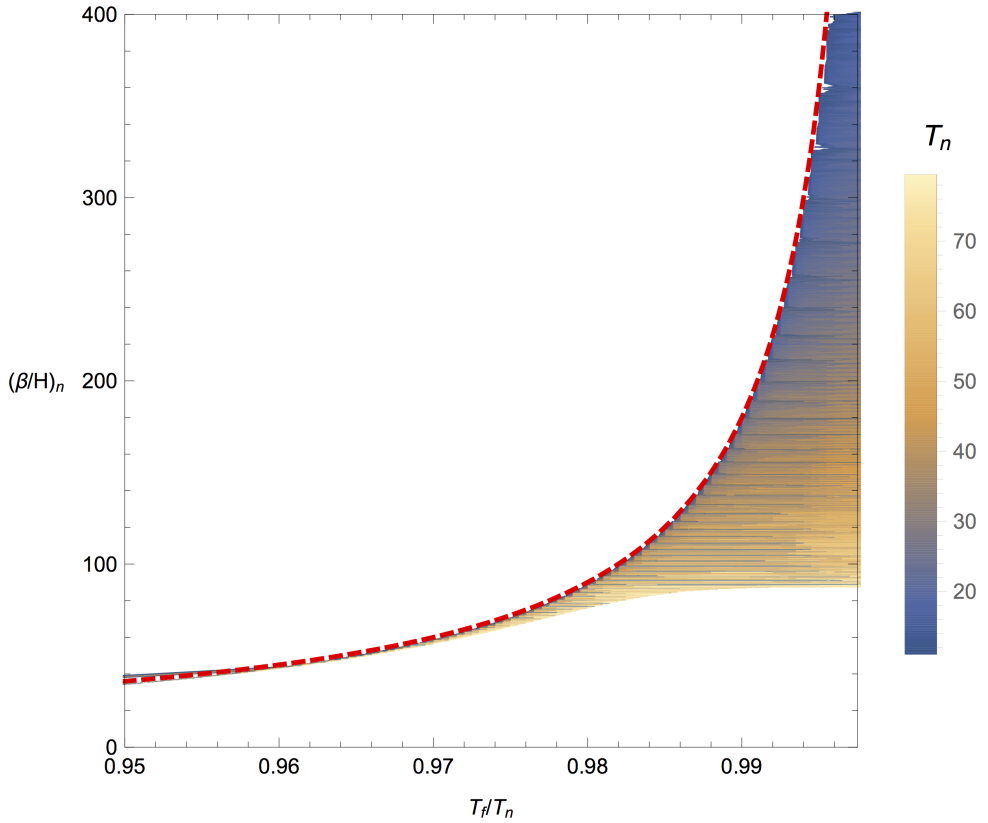

Figure D.2: Density plot of the lower bound of the bubble nucleation rate $(\beta/H)_n$ against the ratio T_f/T_n. The density represents the nucleation temperature T_n. For not-so-fast phase transitions, $T_f/T_n \lesssim 0.98$, the value of $(\beta/H)_n$ is approximately constant in T_n. The red, dashed curve approximates the $T_n \to 0$ solution and is given by eq. (D.11).

Our assumption that $B(T)$ is constant is most likely valid for very fast phase transitions, $T_f/T_n \to 1$. In this limit, we determine that the nucleation rate must be

$$\left(\frac{\beta}{H}\right)_n \gtrsim \frac{(7000\text{ GeV})}{T_n} \tag{D.10}$$

for the phase transition to complete. This can be regarded as the most pessimistic bound for $(\beta/H)_n$; any phase transition with a nucleation rate satisfying eq. (D.10) *will* complete.

It is interesting to note the behaviour of the solutions of $(\beta/H)_n$ against T_n as the value of T_f/T_n moves away from unity. At high temperatures, solutions are well approximated by eq. (D.10). But as the nucleation temperature lowers, the solution plateaus to a constant value of $(\beta/H)_n$. This constant is roughly given by

$$\left(\frac{\beta}{H}\right)_n \approx 1.8\left(1-\frac{T_f}{T_n}\right)^{-1}. \tag{D.11}$$

This observation is illustrated in Figure D.2.

Appendix E

Numerical approach in accurately determining friction

We discretise the differential equations and then evolve the resulting difference equations from their initial condition. However, in order to solve eq. (4.64) and eq. (4.65), one would need to know the temperature variation of $V_{\rm path}$. In this work we resort to Taylor expanding the potential about its value at the previous temperature; for the i^{th} iteration this is T_i. Up to quartic order

$$\begin{aligned} V_{\rm path}(\Phi, T_{i+1}) = \quad & V_{\rm path}(\Phi, T_i) + (\delta T)\left.\frac{\partial V_{\rm path}(\Phi,T)}{\partial T}\right|_{T=T_i} + \frac{(\delta T)^2}{2}\left.\frac{\partial^2 V_{\rm path}(\Phi,T)}{\partial T^2}\right|_{T=T_i} \\ & + \frac{(\delta T)^3}{3!}\left.\frac{\partial^3 V_{\rm path}(\Phi,T)}{\partial T^3}\right|_{T=T_i} + \frac{(\delta T)^4}{4!}\left.\frac{\partial^4 V_{\rm path}(\Phi,T)}{\partial T^4}\right|_{T=T_i} + \mathcal{O}(\delta T)^5. \end{aligned} \tag{E.1}$$

Manipulating this expression, we can see that

$$\frac{\partial V_{\rm path}(\Phi, T_{i+1})}{\partial T_{i+1}} = \left.\frac{\partial V_{\rm path}(\Phi,T)}{\partial T}\right|_{T=T_i} + (\delta T)\left.\frac{\partial^2 V_{\rm path}(\Phi,T)}{\partial T^2}\right|_{T=T_i} + \mathcal{O}(\delta T)^2. \tag{E.2}$$

Adopting the notation $V_{\pm a} = V_{\rm path}(\Phi, T_i \pm a(\delta T_0))$, we determine the derivatives at $T = T_i$ in the following way. We linearise the equations for Taylor expanded potentials V_{-2}, V_{-1}, V_0, V_{+1} and V_{+2}. This recovers expressions for the finite-sized derivatives up to fourth order:

$$\left.\frac{\partial V_{\rm path}(\Phi,T)}{\partial T}\right|_{T=T_i} = \frac{V_{+1} - V_{-1}}{2(\delta T_0)}, \tag{E.3}$$

$$\left.\frac{\partial^2 V_{\rm path}(\Phi,T)}{\partial T^2}\right|_{T=T_i} = \frac{V_{+1} - 2V_0 + V_{-1}}{(\delta T_0)^2}, \tag{E.4}$$

$$\left.\frac{\partial^3 V_{\text{path}}(\Phi, T)}{\partial T^3}\right|_{T=T_i} = \frac{V_{+2} - 2V_{+1} + 2V_{-1} - V_{-2}}{2(\delta T_0)^3}, \tag{E.5}$$

$$\left.\frac{\partial^4 V_{\text{path}}(\Phi, T)}{\partial T^4}\right|_{T=T_i} = \frac{V_{+2} - 4V_{+1} + 6V_0 - 4V_{-1} + V_{-2}}{(\delta T_0)^4}. \tag{E.6}$$

Using a feasible step size δT_0 is essential for reliable estimates of these derivatives. Although this step size is ideally small, we must be mindful of any errors residing from numerical precision. For our investigation in Section 4.5.2, we take $\delta T_0 = 0.1$ GeV.